Numerical simulation of metal materials quenching by applying Eulerian two-fluid model

Cukrov, Alen

Doctoral thesis / Disertacija

2023

Degree Grantor / Ustanova koja je dodijelila akademski / stručni stupanj: **University of Zagreb, Faculty of Mechanical Engineering and Naval Architecture / Sveučilište u Zagrebu, Fakultet strojarstva i brodogradnje**

Permanent link / Trajna poveznica: https://urn.nsk.hr/urn:nbn:hr:235:117642

Rights / Prava: In copyright / Zaštićeno autorskim pravom.

Download date / Datum preuzimanja: **2024-03-29**

Repository / Repozitorij:

Repository of Faculty of Mechanical Engineering and Naval Architecture University of Zagreb







University of Zagreb

Faculty of Mechanical Engineering and Naval Architecture

Alen Cukrov

NUMERICAL SIMULATION OF METAL MATERIALS QUENCHING BY APPLYING EULERIAN TWO-FLUID MODEL

DOCTORAL DISSERTATION

Zagreb, 2023



University of Zagreb

Faculty of Mechanical Engineering and Naval Architecture

Alen Cukrov

NUMERICAL SIMULATION OF METAL MATERIALS QUENCHING BY APPLYING EULERIAN TWO-FLUID MODEL

DOCTORAL DISSERTATION

Supervisor:
Ivanka Boras, PhD, Full Professor Tenure

Zagreb, 2023



Sveučilište u Zagrebu

Fakultet strojarstva i brodogradnje

Alen Cukrov

NUMERIČKA SIMULACIJA GAŠENJA METALNIH MATERIJALA PRIMJENOM EULEROVA DVOFLUIDNOGA MODELA

DOKTORSKI RAD

Mentor:
prof. dr. sc. Ivanka Boras

Zagreb, 2023.

Bibliography data

UDC: 536.2:532.5:519.8

Keywords: immersion quenching; Stefan problem; two-fluid VOF model; locally imposed closures; boiling flow; mesh versatility; frozen turbulence

Scientific area: TECHNICAL SCIENCES.

Scientific field: Mechanical engineering.

Institution: Faculty of Mechanical Engineering and Naval Architecture, University of Zagreb.

Thesis supervisor: Ivanka Boras, PhD, Full Professor Tenure.

Number of pages: 135

Number of figures: 46

Number of tables: 14

Number of references: 103

Date of oral examination: February 10th, 2023

Thesis defense committee:

- Željko Tuković, PhD, Full Professor Tenure – President.
- Dr. Yohei Sato, Paul Scherrer Institut, Switzerland – Member;
- Dr. Bojan Ničeno, Paul Scherrer Institut, Switzerland – Member;
- Darko Landek, PhD, Full Professor – Member;
- Severino Krizmanić, PhD, Assistant Professor – Member.

Archive: Faculty of Mechanical Engineering and Naval Architecture, University of Zagreb.

I dedicate this thesis to my mom and dad.

ACKNOWLEDGEMENTS

First of all, I would like to express my sincere gratitude to my thesis supervisor, **Professor Ivanka Boras**. Since our first conversation, which was, to the best of my knowledge, on Monday, June 8th, 2009, she has been a reference to me in many important aspects of my life. She has always had free time for consulting and provided me with wise and supportive advice. Furthermore, I would like to thank **Professor Emeritus Antun Galović**, a true intellectual who has introduced me to the area of science and research. Furthermore, I would like to acknowledge his input during the writing of this thesis. Back in 2012, Professor Galović, as Head of the Chair of Engineering Thermodynamics, emphasized the necessity for this topic to be solved by using numerical methods. Back in 2009, the first consulting in the area of thermodynamics that I did at the Chair of Engineering Thermodynamics, in one of the offices, was with **Asst. Professor Saša Mudrinić**, to whom I express my sincere appreciation. I had his support and trust, especially in 2012, when he wanted me to join industrial CFD, but also during my appointment and, in particular, at the very beginning of my official work as a Ph.D. student. Back in 2010, **Professor Zdravko Virag**, a doyen in the field of classical fluid mechanics, revealed to me the secret of how to deal with any physical text to establish a full understanding, i. e., the importance of derivations in studying the natural sciences. He has been a reference to me in continuum mechanics matters ever since, to whom I am ineptly grateful. Furthermore, Professor Virag has given me the contact information for starting my international endeavors. **Assistant Professor Severino Krizmanić** suggested dealing with CFD to me in the autumn of 2010 after I visited him for consulting in his course Fluid Mechanics II. Professor Krizmanić, furthermore, played an important role in my employment here at FAMENA. His efforts during this research are also gratefully acknowledged. The vast engineering knowledge I received from **Professor Miroslav Ruševljan** to whom I am extremely grateful. He shared with me so many important engineering ideas, thus paving the path for doing serious work as a research and development engineer. An upgrade to work at a world-class level in the area of computational continuum mechanics has been achieved via The collaboration with remarkable **Associate Professor Željko Tuković**, with whom I met eariler in 2011 via the lectures in his course, has resulted in an upgrade to work at a world-class level in the area of computational continuum mechanics. The collaboration began on Thursday, November 17 th, 2011. Through many years, Professor Tuković was my most serious teacher of numerical modeling, and I may regard him as my official CFD tutor. I would also like to thank **Professor Damir Dović** who

has strongly emphasized to me the importance of consulting the official software documentation and the importance of fundamental test cases to obtain successful numerical simulation in complex geometries. My friend, **Dr. Tomislav Marić**, to whom I was recommended by Professor Virag in 2011, had played an important role during my master's studies and ever since. He told me what to do, that is, which were the important topics that should be covered in order to pursue world-class research in the field of computational modeling, and he helped me to come on a five month Erasmus mobility at the institution where he was working at the time. Since 2016, I have had a close collaboration with **Dr. Bojan Ničeno**, to whom I am extremely grateful. He has opened me to the world of top-level science and put me into it; I acknowledge his trust and confidence in me to take me to the Paul Scherrer Institute and provide me with challenging multiphase flow with phase-change topics. Since the very beginning of October 2017, I have had the opportunity to work with **Dr. Yohei Sato**, who has played a crucial role in the development of the present computational model. It was a joy and a pleasure to work twice, in October 2017 and during the academic year 2019/2020, with such an exceptional professional. **Professor Darko Landek**, whom I remembered very well from my first year of undergraduate study in 2009, has shown patience and professionalism during this work, and I am grateful for all his input during this research.

The astonishing work in the area of organizing the offices of the Department of Engineering Thermodynamics here at FAMENA is done by the remarkable **Ms. Silva Čep**. Since 2009, when we met, she has shown a full capability to help us work smoothly without being disturbed by administration matters, and I am also grateful for her input during this research.

A special thank goes to my office mate , **Mr. Danijel Zadravec**, who has significantly contributed to my work with his suggestions and advises. He has always been ready for collaboration and discussion, especially in the most difficult circumstances, when it seemed that the breakthrough would be difficult.

Of course, I would like to thank all my other colleagues, friends, and students who have been supporting me through these years. The inputs from other professors from the University of Zagreb's Faculty of Mechanical Engineering and Naval Architecture have been also gratefully acknowledged. Finally, I have to acknowledge the help of my family in helping me to obtain intellectual wideness, but also leaving me the freedom of choice that comes with responsibility.

ABSTRACT

A novel approach for the solution of mass transfer within the framework of the multi-fluid model supplemented with the Volume of Fluid (VOF) method, i.e. two-fluid VOF, is presented in this thesis with a goal to conduct the computation of the temperature field inside a specimen and on its surface during the immersion quenching process of a metal material in a liquid medium. Thereby, the initial temperatures of the specimen and the bath were identified as the main input data that should be supplemented to the model. The governing equation set is comprised of mass, momentum, and energy conservation equations, written on a per-phase basis and supplemented with closure models via the source terms, the so-called locally imposed closures approach. In our method, the heat and mass transfer is calculated from the heat transfer coefficient, which has a fictitious function and depends on the local cell size and the thermal conductivity, and the implementation is straightforward because of the usage of the local value instead of a global parameter. The interface sharpness is ensured by the application of the geometrical reconstruction scheme implemented in VOF. The model is verified against the analytical solution to Stefan problem, for three types of computational meshes including triangular cells, and good agreement was obtained for the interface position and the temperature field. The straightforward application to the engineering problem of film boiling around a cylinder specimen has been carried out by supplementing the model with the prescribed turbulent kinetic energy value, the so-called frozen turbulence, and, later on, in the application section, mesh motion. Thereby, the temperature field has been successfully reconstructed inside the solid, the conjugate heat transfer (CHT) approach. The analysis of integral quantities has shown the satisfactory agreement between the computation results and the experiment, and the ones obtained using the correlations from the literature.

Keywords:
immersion quenching process; Stefan problem; two-fluid VOF model; locally imposed closures; boiling flow; mesh versatility; frozen turbulence.

SAŽETAK

Novi pristup za rješavanje prijenosa mase unutar okvira višefluidnoga modela potpomognutog metodom volumnog udjela fluida (*engl*. Volume-of-fluid, VOF), tj., dvofluidnoga VOF modela, je predstavljen u ovom radu s ciljem provedbe proračuna temperaturnog polja unutar i na površini uzorka tijekom procesa gašenja metalnih materijala postupkom uranjanja u kapljeviti medij. Pritom su kao glavni ulazni podaci identificirani inicijalna temperatura uzorka i inicijalna temperatura medija za gašenje. Skup jednadžbi održanja je sastavljen od zakona očuvanja mase, količine gibanja i energije, zapisan za svaku od faza i nadopunjen dopunskim relacijama putem izvorskih članova, tzv. pristup lokalno narinutih dopunskih relacija. U predloženoj metodi, prijenos topline i mase je računat na temelju koeficijenta prijelaza topline, koji ima fiktivnu ulogu te ovisi o lokalnoj veličini ćelije i toplinskoj provodnosti, te čija je implementacija jednostrana uslijed korištenja lokalnih vrijednosti umjesto globalnog parametra. Glatkoća, tj. oštrina granice faza je osigurana primjenom sheme geometrijske rekonstrukcije (*engl*. geometrical reconstruction scheme) ugrađene u VOF metodu. Model jer verificiran korištenjem analitičkog rješenja Štefanovog problema, za tri tipa računalne (numeričke) mreže uključujući pritom i trokutne kontrolne volumene, te je postignuto zadovoljavajuće slaganje položaja granice faza i temperaturnog polja. Jednostrana primjena na inženjerski problem filmskog isparivanja oko cilindričnog uzorka jer provedena nadopunjujući model s unaprijed zadanom vrijednošću kinetičke energije turbulencije, tzv. zamrznuta turbulencija, te, kasnije, u odjeljku s primjenom metode, gibajućom mrežom. Pritom je uspješno rekonstruirano temperaturno polje unutar krutine, spregnuti prijenos topline. Analizom integralnih veličina uočeno je zadovoljavajuće slaganje s rezultatima eksperimenta i rezultatima dobivenim korelacijama iz literature.

Ključne riječi:
gašenje uranjanjem; Štefanov problem; dvofluidni VOF model; lokalno narinute dopunske relacije; strujanje s isparivanjem; versatilnost numeričke mreže; zamrznuta turbulencija.

EXTENDED ABSTRACT IN CROATIAN LANGUAGE

0.1 Uvod

Održivi razvoj pretpostavlja razvoj, proizvodnju i primjenu kvalitetnih, energetski efikasnih i po okoliš manje utjecajanih novih proizvoda. Energetska efikasnost i potreba za smanjenjem utjecaja na okoliš posebno se ističu u izradi i uporabi proizvoda koji zahtjevaju prijenos i pretvorbu velikih količina energije (i toplinskih tokova). Takvi proizvodi su primarno vezani uz energetiku, termotehniku i procesnu tehniku, ali i druga područja poput metalurgije, zavarivanja, obrade deformacijom u toplom stanju, toplinske obrade metala i dr., u kojima je prisutan čitav skup procesa kod kojih su od iznimnog značaja termodinamički procesi unutar materijala te prijenos topline i mase u materijalu obratka, kao i u radnim medijima primjenjenim u procesu obrade (primjerice za hlađenje, podmazivanje). U industrijskim procesima hlađenja od iznimnog je značaja za efikasnost prijenosa topline mjehurasto isparivanje kojim se ostvaruje značajno odvođenje gustoće toplinskog toka uz relativno niske razlike temperatura, rezultirajući time vrlo velikim iznosima koeficijenta prijelaza topline. S druge strane, u procesima toplinske obrade metala se, uslijed iznimno velikih gustoća toplinskog toka, oko površine predmeta formira parni omotač, kojim se signifikantno reducira prijenos topline s površine predmeta u medij za gašenje. Numeričko modeliranje prijenosa topline i mase, u kontekstu industrijske primjene ovakvih procesa, podrazumijeva primjenu načelno dva tipa metoda za rješavanje višefaznog strujanja (*engl.* multiphase flow). Prva su skupina tzv. volumne metode, poput primjerice metode volumnog udjela fluida (*engl*. Volume-of-Fluid, VOF) te metoda razina (*engl*. level-set method, LSM), kod kojih se dobiva detaljan opis granice faza (*engl*. interface), ali se iziskuje primjena fine rezolucije mreže uz samu granicu faza, kako bi se granica faza mogla adekvatno obuhvatiti u proračunu. Drugu skupinu čine osrednjene metode, kod kojih se u postupku izvođenja matematičkog modela gubi informacija o položaju granice faza, pa se međufazni prijenos modelira putem izvorskih članova u jednadžbama očuvanja. Ovoj skupini metoda pripadaju model mješavine (*engl*. mixture model, MM) i Eulerov dvofluidni model (*engl.* two-fluid model, TFM). S obzirom da je model mješavine zapravo pojednostavljeni dvofluidni model (eliminira se detaljan opis međufaznog prijenosa na granicama faza), u nastavku, za proračune u radu primjenit će se samo Eulerov dvofluidni model, u kojem je potrebno uvesti dodatne korelacije između dviju faza, parne i kapljevite, kojima se opisuje međufazni prijenos količine gibanja i energije. U ovom modelu

gubi se informacija o položaju granice faza, što predstavlja poteškoću pri modeliranju procesa s isparivanjem u kapljeviti medij u toplinskoj obradi metala, odnosno procesa gašenja uranjanjem austenitiziranog čelika u bazen ili kupku za ohlađivanje. Zato se u okviru ovog rada koristi dvofluidna formulacija kombinirana s VOF metodom, tj. Eulerov dvofluidni model, koji kombinira prednosti VOF metode u smislu da je granica faza točno (egzaktno!) opisana, a zadržava svojstvo dvofluidnoga modela na način da se proračun može provesti korištenjem grublje rezolucije mreže i većih vremenskih inkremenata tijekom simulacije.

0.2 Dosadašnja istraživanja

Pregledom dosadašnjih istraživanja utvrđeno je kako su oba tipa numeričkog modeliranja višefaznog strujanja primjenjivani u kontekstu modeliranja procesa gašenja uranjanjem, ali i postupka gašenja prskanjem (*engl*. spray quenching). Ključna uloga svih proračuna višefaznog strujanja pripada načinu modeliranja prijenosa mase na granicama faza. Za modeliranje prijenosa mase ističu se tri glavna pristupa: model energijske bilance (*engl*. energy jump model); Schrageov model; i Leejev model. Model energijske bilance, proizlazi iz jednostavnog rezoniranja na temelju mehanike kontinuuma, a taj je da je gustoća toplinskog toka koja se prenese u procesu promjene faze jednaka razlici gustoća toplinskog toka provođenjem (Fourierov stavak!) s obje strane granice faza. Takav pristup iziskuje doduše definiranje inicijalnog sloja pare (kod isparivanja!) neposredno uz sâm uzorak jer se u jednadžbi prijenosa mase nalazi gradijent volumnog udjela parne faze. Međutim, nije nužno uvoditi empirijske koeficijente ili faktore. S druge strane, Schrageov model dolazi iz kinetičke teorije plinova, te je za njegovo korištenje potrebno definirati tzv. akomodacijski faktor kako bi se dobili ispravni rezultati proračuna. Međutim, i ovaj model iziskuje definiranje inicijalnog sloja disperzne faze. Posljednji navedeni model je Leejev model koji po definiciji ne zahtijeva definiranje inicijalnog sloja disperzne faze, što ga čini prikladanim za proračun s promjenom faze u stopostotnom monofaznom mediju (*engl*. bulk fluid). Međutim, i ovaj model zahtijeva kalibriranje empirijskog koeficijenta kako bi se postigla zadovoljavajuća točnost. U ovom je radu stoga primijenjen pristup najsličniji metodi energijske bilance jer fenomenološki najbolje opisuje procese isparivanja tekućih medija kod gašenja uranjanjem. Prisutnost inicijalnog sloja pare je opravdana činjenicom da je cilj rada modelirati filmsko isparivanje pri procesu gašenja uranjanjem, što za posljedicu ima da će rezultati numeričke simulacije trebati biti odgođeni za određeno vrijeme potrebno za stvaranje parnog omotača. Pregledom dosada provedenih

istraživanja utvrđeno je samo nekoliko slučajeva u kojima se dvofluidnom formulacijom uspješno riješilo napredovanje granice faza na fundamentalnoj razini. U radu je razvijena nova metoda numeričkog proračuna prijelaza topline prikladna za matematičko modeliranje gašenja ugrijanog čelika uranjanjem u tekuća sredstva za gašenje, vodu ili ulje za kaljenje.

0.3 Cilj i hipoteza istraživanja

Cilj provedenog istraživanja je razvoj numeričke metode za proračun gašenja uranjanjem u kapljeviti medij podložan Leidenfrostovu fenomenu, pri čemu su poznati: inicijalna temperatura medija za gašenje te inicijalna temperatura uzorka. Metoda treba dati zadovoljavajuću temperaturnu distribuciju unutar uzorka i na njegovoj površini u režimu filmskog isparivanja, koje je prisutno na početku procesa gašenja uranjanjem u isparivi medij za gašenje (npr. kapljevita voda, ulje). Otud se izvodi i hipoteza istraživanja koja glasi: „*Korištenjem Eulerova dvofluidnoga modela može se izračunati temperaturna raspodjela unutar uzorka u režimu filmskog isparivanja*". Naglasak je stavljen na primjenu dvofluidnog modela (*engl*. two-fluid model, TFM) zbog njegove efikasnosti na proračunima s niskom rezolucijom računalne mreže, čime je podesan za primjenu na geometrijskim domenama većih razmjera, koje se susreću u industrijskim primjenama toplinske obrade.

0.4 Numerička metoda

Uspješno numeričko modeliranje procesa mjehurastog isparivanja, jednako kao i procesa filmskog isparivanja nužno zahtijeva efikasno modeliranje prijenosa mase na graničnim površinama faza (u nastavku granica faza). U radu se predlaže novi model prijenosa mase, izveden iz modela energijskog skoka (*engl*. energy jump model) raspisanog za slučaj čistog provođenja topline unutar sloja pare i prisutnosti jedne zasićene i jedne nezasićene (pregrijane ili pothlađene) faze (npr. vrela kapljevina i pregrijana para) i toplinskog modela promjene faze (*engl*. thermal phase change model, TPCM), uz istu pretpostavku. Dobiveni model je zapravo aproksimacija temperaturnog gradijenta u okolišu granice faza, pri čemu se udaljenost od granice faza tretira kao polovica duljine stranice kuboidnog kontrolnog volumena numeričke mreže. Ta se aproksimacija provodi primjenom koeficijenta prijelaza topline, $h_{pq'}$, dostupnog u TPC modelu kao fiktivne varijable, kojom se u TCP model unosi lokalna duljina ćelije kao

$V_c^{1/3}$, kako je ranije navedeno. Međufazna se površina računa kao gradijent volumnog udjela faze, čime se osigurava primjena konstitutivnih relacija isključivo na granicama faza. Nadalje, ovim se pristupom osigurava i ponašanje metode nalik onome kod jednofluidne VOF formulacije, tj. jasno razgraničenje između dviju faza, odnosno modeliranje podvojenog strujanja (*engl*. separated flows). Isto je uočeno i u drugim metodama, metodi algebarske gustoće međufazne površine (*engl*. algebraic interfacial area density, AIAD) i metode velikog mjehura (*engl*. large bubble method, LBM). Metoda je implementirana u računalni program ANSYS Fluent korištenjem korisnički definiranih funkcija (*engl.* user-defined functions, UDFs).

0.4.1 Verifikacija metode

Model za predviđanje temperaturne raspodjele unutar uzorka na čijoj površini dolazi do pojave Leidenfrostovog fenomena verificiran je rješavanjem Štefanovog problema, nestacionarnog napredovanja fazne granice; pri čemu je rezultat numeričke simulacije uspoređen s analitičkim rješenjem položaja granice faza, $X(t)$, te distribucije temperature uzduž prostorne koordinate x. Proračun je proveden na tri različite mreže: jednolikoj pravokutnoj, nejednolikoj (gradiranoj) pravokutnoj i hibridnoj mreži. Pritom je hibridna mreža komponirana od nejednolikih pravokutnih kontrolnih volumena i trokutnih kontrolnih volumena. Za svaki od navedenih tipova mreže je provedena studija utjecaja rezolucije mreže na dobivena rješenja, te je potvrđena ranije poznata pretpostavka kako prilikom korištenja Eulerova dvofluidnoga modela rezolucija mreže nema bitan utjecaj na konačni rezultat simulacije.

0.4.2 Validacija metode

Eulerov dvofluidni model nestacionarnog napredovanja fazne granice kapljevina/para validiran je korištenjem eksperimentalnih rezultata dostupnih u Momoki *et al*. [1], koji su dobiveni za cjelokupan proces hlađenja srebra u kapljevitoj vodi pri temperaturi zasićenja. Pri modeliranju filmskog isparivanja, uočena je važnost modeliranja turbulentnog strujanja kapljevine oko filma vodene pare. Utvrđeno je kako disperzirani model turbulencije, tj. model turbulencije u kojem se jednadžbe očuvanja veličina strujanja rješavaju jedino u kontinuiranoj fazi, dok se unutar disperzirane faze turbulencija modelira korelacijom, adekvatno opisuje fiziku procesa filmskog isparivanja sa spregnutim prijenosom topline (*engl.* conjugate heat transfer, CHT). S obzirom na kompleksnost modeliranja turbulentnog strujanja za ovakav slučaj,

pretpostavljena je vrijednost kinetičke energije turbulencije unutar domene, te je ta vrijednost zadana konstantnom tijekom proračuna, tzv. „zamrznuta turbulencija". Određena se vrijednost kinetičke energije turbulencije tako zadaje unutar glavnine domene, izuzev sloja ćelija neposredno uz sâm uzorak; čime se modelira laminarno strujanje u filmu pare uz sâm objekt. Na temelju provedenih proračuna, utvrđeno je kako vrijednost kinetičke energije turbulencije 0,25 m^2/s^2 adekvatno modelira spregnuti prijenos topline jer se njom postiže zadovoljavajuće slaganje temperaturnog polja unutar krutine dobivenog numeričkom simulacijom s rezultatima eksperimenta, za prvih 15 s trajanja procesa. Potvrđeno je kako primjenom Kelvin-Helmholtzove teorije nestabilnosti se može dobiti adekvatna vrijednost kinetičke energije turbulencije, ako se za relativnu brzinu, prisutnu u brojniku tog izraza, uzme vrijednost brzine strujanja unutar filma pare. Brzina strujanja izračunava se iz teorije graničnog sloja, uz pretpostavku glatke granice kapljevina-para, te da je brzina na rubu parnog omotača jednaka nuli (*engl*. no-slip condition). Primijećeno je kako koeficijent turbulentne viskoznosti, koji je svojstvo strujanja, idealno prati tijek formiranja pare. Navedeno se može objasniti primjenom tenzora brzine deformacije, koji se nalazi unutar definicije turbulentne viskoznosti odabranog modela turbulencije.

0.5 Primjena metode

U nastavku rada je dan opis koraka proračuna gašenja valjka od superlegure Inconela 600 uranjanjem, pri čemu su poznati: temperatura medija za gašenje i inicijalna temperatura valjka (uzorka). Pritom se u ovom slučaju radi o pothlađenoj kapljeviti temperature 60 °C, te je radi jednostavnosti proračuna, pretpostavljena ista temperatura i za okolni medij unutar kojeg se uzorak nalazi neposredno prije uranjanja. Bitno je napomenuti da se za taj, okolni medij, u proračunu pretpostavilo da se radi o vodenoj pari temperature 60 °C. Na taj se način se simplificira matematički model jer nije potrebno uzimati dodatni skup jednadžbi za modeliranje prijenosa topline na okolni zrak (potrebna bi bila još jedna skupina jednadžbi očuvanja za zrak, čime bi se proračun bitno usporio), na koji se ionako ne posvećuje pozornost uslijed izrazito niskih vrijednosti koeficijenta prijelaza topline s užarene krutine (crveni dio spektra, temperature preko 800 °C) na okolni medij. Nadalje, na taj je način izuzeta mogućnost dolaska do prijenosa mase i okolnog medija (jer su oba pri istoj inicijalnoj temperaturi), do koje bi moglo doći uslijed temperaturnog gradijenta na slobodnoj površini medija za gašenje. Uzorak se inicijalno nalazi na temperaturi 855 °C, što je u suglasju s normom ISO 9950, koja propisuje

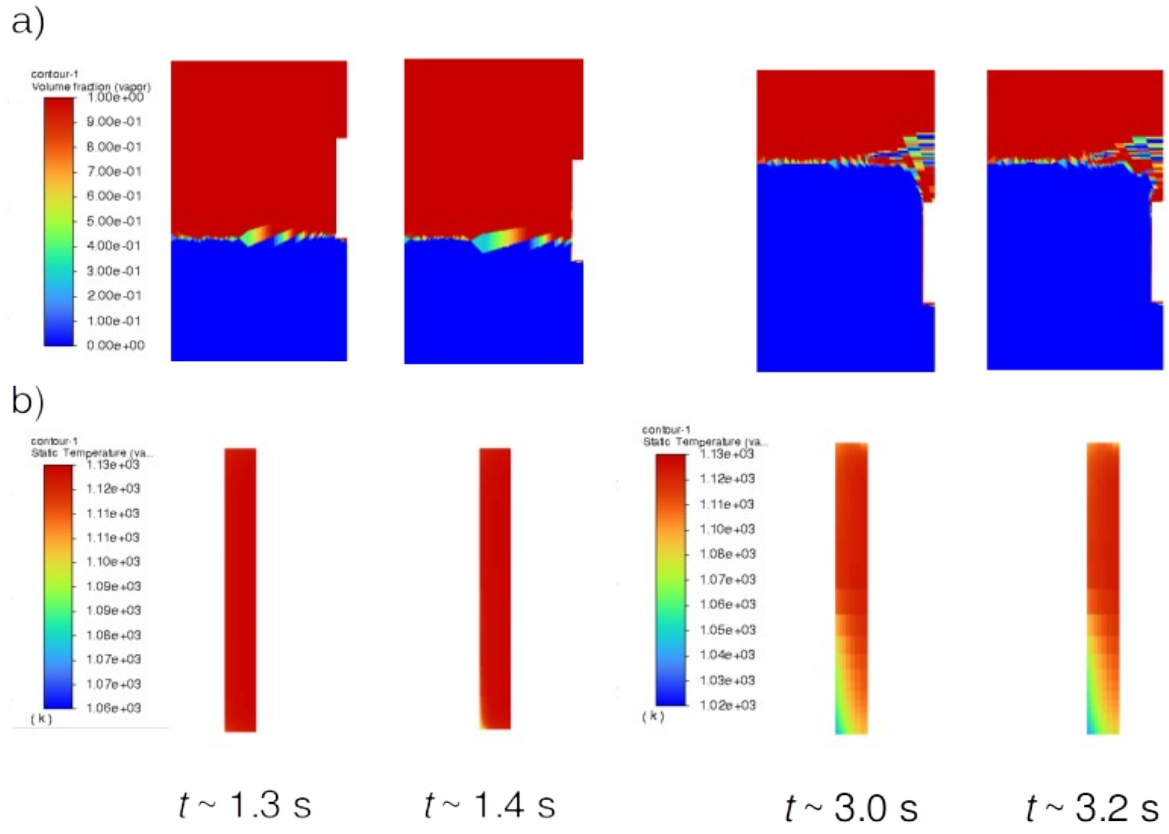
uvjete pod kojima bi se trebao provoditi ovakav eksperiment. Uz navedene vrijednosti, inicijalne temperature medija i uzorka, zadana je i vrijednost kinetičke energije turbulencije u iznosu od 0,1 m^2/s^2, na temelju prijašnjih istraživanja. Definirane su dvije zone s obzirom na režim strujanja (turbulentni ili laminarni) unutar domene. Prva je međufazna zona 1, koja oplakuje površinu uzorka i proteže se samo jedan sloj ćelija u domenu. Unutar te se zone pretpostavlja laminarno strujanje, tj. kinetička energija turbulencije teži k nuli. Druga zona obuhvaća period neposredno uz sâm objekt, ali ne i samu zonu 1, te se unutar nje definira ranije navedena vrijednost kinetičke energije turbulencije. U ostatku domene se pretpostavlja laminarno strujanje, na način naveden za međufaznu zonu 1. Također, primijenjena je metoda pomične mreže s topološkom promjenom, tj. tijekom gibanja mreže (objekta) dolazi do generiranja novih ćelija i brisanja nekih postojećih, pri čemu se provodi interpolacija rezultata sa stare mreže na novu. Uzorak se uranja konstantnom brzinom uranjanja, 0,13 m/s, pri čemu je za gibanje uzorka u numeričkoj simulaciji korišten tzv. ALE (*engl.* arbitrary Lagrangian-Eulerian) pristup, kod kojeg se unutar svake od domena rješava Eulerov skup jednadžbi (praćenje promjena unutar kontrolnog volumena), dok se sama granica između dviju domena opisuje Lagrangeovom formulacijom (praćenjem gibanja materijalnog volumena). Posebnost niklove superlegure Inconela 600 je dobro predvidljiva promjena fizikalnih svojstava, toplinske provodnosti, λ_s, i specifičnog toplinskog kapaciteta, c_s, s promjenom temperature uzorka; što je potrebno uzeti u obzir pri proračunu. Materijal je izrazito visoke toplinske prodornosti, što znači da su prilikom gašenja uranjanjem prisutni svi režimi Leidenfrostovog isparivanja (npr. filmsko i mjehurasto isparivanje, i prijenos topline konvekcijom).

0.6 Rezultati proračuna

Provedenim proračunom dobivena je vrijednost temperaturne raspodjele u središtu valjka, u glavnini faze parnog omotača, što je razvidno iz položaja točke infleksije na tranzijentnu temperaturnu raspodjelu dobivenu eksperimentom predstavljenim u Landek *et al.* [2], u rasponu vrijednosti temperatura od ± 10 %, što se smatra vrlo prihvatljivim. Vremenska promjena temperature na površini valjka uspoređena je s rezultatima analitičkog modela, tj. proračuna metodom analize inverznog prijenosa topline (*engl.* inverse heat transfer method analysis, IHTA), te je također postignuto zadovoljavajuće slaganje u pojasu pogreške proračuna (10 %). Numeričkim proračunom temperaturnog polja unutar same krutine je potvrđena hipoteza istraživanja, a ta je da se korištenjem Eulerova dvofluidnoga modela može efikasno

riješiti temperaturna distribucija unutar krutine u režimu filmskog isparivanja pri procesu gašenja uranjanjem. Navedeno potvrđuje grafički prikaz na Sl. 1.

Nadalje, analizom integralnih veličina, osrednjenih po površini uzorka (cjelokupnoj) i po pojedinim površinama (donja baza, površina A; plašt, površina B i gornja baza, površina C): koeficijenta prijelaza topline (i cjelokupna i pojedine površine) i gustoće toplinskog toka (samo po pojedinim površinama uzorka) utvrđeno je njihovo dobro slaganje s rezultatima eksperimenta (koeficijent prijelaza topline) i proračunom istih korištenjem korelacija dostupnih u Momoki *et al*. [1]. Proračunom su obuhvaćeni i mnogi detalji vezani uz sâm proces uranjanja. Tako je razvidno naglo povećanje koeficijenta prijelaza topline i gustoće toplinskog toka na donjoj bazi uzorka kada se uzorak nalazi neposredno ponad slobodne površine medija za gašenje. Također je uočljivo i formiranje kratera na gornjoj površini uzorka kada je uzorak potpuno uronjen u kapljeviti medij za gašenje.



Sl. 1. Prikaz numeričkih rezultata simulacije gašenja uranjanjem: a) polje volumnog udjela parne (kapljevite) faze; b) temperaturno polje unutar krutine.

0.7 Zaključci provedenog istraživanja

U provedenom istraživanju razvijen je novi model prijenosa mase na granicama faza, temeljen na toplinskoj bilanci na granici faza, u kojem se kao fiktivna varijabla koristi koeficijent prijelaza topline time što se putem te veličine aproksimira udaljenost središta kontrolnog volumena koji sadrži granicu faza i same granice faza, te uvodi toplinska provodnost u aproksimativni izraz za izračun gustoće toplinskog toka na granici faza. Rezultati provedenih proračuna potvrđuju slijedeće:

1. Štefanov problem uspješno je riješen na mrežama različitih gustoća raspodjele ćelija, te mrežama različitih oblika. Potvrđeno je kako pri korištenju Eulerova dvofluidnoga modela, nije nužno imati finu rezoluciju numeričke mreže, jer se međufazni prijenos modelira korelacijama;
2. postignuto je ponašanje dvofluidnog modela nalik onome jednofluidnog na granici faza sa stajališta jednadžbe očuvanja količine gibanja; nagli skok brzine je zabilježen u ćelijama koje obuhvaćaju granicu faza;
3. odabirom sheme geometrijske rekonstrukcije održana je jasna granica između dva fluida, čime se postiglo ponašanje VOF metode u kontekstu modeliranja dvofluidnim Eulerovim modelom, sa svim njegovim prednostima (niska rezolucija mreže i relativno veliki vremenski koraci);
4. nestrukturirana mreža je uspješno primijenjena u rješavanju Štefanovog problema, te je zabilježen, kao i u ostalim slučajevima, ispravan rezultat u smislu da se dominantan prijenos mase odvija na granici faza (izostaje u kontinuiranim fazama), te da se temperaturna raspodjela unutar proračunske domene i položaj granice faza slažu s analitičkim rješenjem;
5. primjena modela za izračun temperaturnog polja unutar krutine, zajedno s rješavanjem polja strujanja, je uspješno provedena uključujući disperzni model turbulencije s dvije jednadžbe. Pritom je samo za kontinuiranu fazu (kapljevita voda u ovom slučaju) definiran skup očuvanja turbulentnih veličina, dok se unutar disperzne faze, pare, turbulencija modelira korištenjem Tchenove korelacije. Primijećeno je kako se unutar filma pare zapravo radi o laminarnom strujanju (nizak *Re* broj), pa se može naslutiti da se radi o turbulenciji uzrokovanoj mjehurima;
6. primjenom Kelvin-Helmholtzove teorije nestabilnosti može se doći do iznosa kinetičke energije turbulencije, koji se, u okviru ovog rada, zadaje, te ostaje konstantan tijekom

odvijanja proračuna (tzv. „zamrznuta turbulencija”). Pritom se brzina strujanja računa korištenjem teorije graničnog sloja za slučaj filmskog isparivanja unutar kapljevine pri temperaturi zasićenja;

7. provedeni proračun faze gašenja u kaljenju čelika daje temperaturnu distribuciju u blizini središta uzorka zadovoljavajuće točnosti. Također, prihvatljiva su i rješenja temperaturne distribucije na površini samog uzorka. Kvalitativna procjena razvoja temperaturnog polja unutar krutine pokazuje fizikalno očekivani tijek temperaturne promjene u procesu gašenja uranjanjem, ali i nakon što je objekt uronjen u kapljeviti medij;
8. analizom integralnih veličina, koeficijenta prijelaza topline i gustoće toplinskog toka, potvrđeno je kako metoda vrlo uspješno predviđa prijenos topline u slučaju gašenja metalnog materijala uranjanjem, što je potvrđeno usporedbom s rezultatima inverznog prijenosa topline (koeficijent prijelaza topline za cilindričnu površinu uzorka) i rezultatima dobivenim korištenjem korelacija dostupnih u literaturi, Momoki *et al*. [1].

Navedeno implicira kako se razvijeni numerički postupak može sa sigurnošću primijeniti u industrijskim proračunima filmskog isparivanja tijekom procesa gašenja uranjanjem, uz napomenu da je potrebno inicijalno zadati, uz inicijalne temperature medija za gašenje i samog uzorka, i vrijednost kinetičke energije turbulencije, koja ovisi o zadanim uvjetima strujanja. Pri tome treba voditi računa da li se matematički modelira isparivanje u mirujućoj kapljevini (*engl.* pool boiling) ili isparivanju uz prisutnost prisilne konvekcije (*engl.* forced convection boiling).

CONTENTS

ACKNOWLEDGEMENTS....VI
ABSTRACT....VIII
SAŽETAK....IX
EXTENDED ABSTRACT IN CROATIAN LANGUAGE....X
0.1 Uvod....X
0.2 Dosadašnja istraživanja....XI
0.3 Cilj i hipoteza istraživanja....XII
0.4 Numerička metoda....XII
0.4.1 Verifikacija metode....XIII
0.4.2 Validacija metode....XIII
0.5 Primjena metode....XIV
0.6 Rezultati proračuna....XV
0.7 Zaključci provedenog istraživanja....XVII
LIST OF FIGURES....XXII
NOMENCLATURE....XXV
1 INTRODUCTION....1
1.1 Motivation....1
1.2 Quenching process....3
1.3 Boiling....7
1.3.1 Single-phase convection....9
1.3.2 Two-phase convection....9
1.3.3 Immersion quenching....10
1.3.4 A summary of boiling processes....13
1.4 Literature review....13
1.4.1 Fundamental studies....13
1.4.2 Closure on fundamental studies....24
1.4.3 Applied studies....25
1.4.4 Applied studies closure....29
1.4.5 Conclusion on literature review....30
1.4.6 A brief disclaimer for Croatian readers....32
1.5 Objectives and hypothesis of the thesis....32
1.6 Expected scientific contribution....33
1.7 Thesis outline....33
2 NUMERICAL METHOD....35
2.1 Mathematical model....36
2.1.1 Conservation equations....36
2.1.2 Closure models....37
2.1.2.1 Interfacial area....37
2.1.2.2 Interphase momentum transfer....37
2.1.2.3 Interphase heat transfer....38
2.1.2.4 Interphase mass transfer....39
2.1.3 Discretization of equations....40
2.2 Model verification....40
2.2.1 Additional relevant studies....40
2.2.1.1 Two-fluid solution to Stefan problem....41
2.2.1.2 Local mass transfer and/or non-uniform/triangular meshes....41
2.2.2 Theoretical solution of Stefan problem....41
2.2.2.1 Conditions at the interface....42
2.2.2.2 Interface position....42
2.2.2.3 Temperature field....43

2.2.3 Conditions of simulations....44
2.2.3.1 Material properties....44
2.2.3.2 Computational domain and boundary conditions....44
2.2.3.3 Initial conditions....45
2.2.3.4 Computational mesh....46
2.2.3.5 Implementation in Fluent....48
2.2.4 Results and discussions of the verification case....48
2.2.4.1 Definition of the interface position....48
2.2.4.2 Definition of computational errors....49
2.2.4.3 Uniform mesh....50
2.2.4.4 Non-uniform meshes....54
2.2.4.4.1 Stretched quadrilateral mesh....54
2.2.4.4.2 Hybrid mesh....56
2.3 Model validation....59
2.3.1 Description of the validation experiment....59
2.3.2 Additional considerations regarding turbulent flow modeling....59
2.3.3 Description of the case and geometry....61
2.3.4 Turbulent kinetic energy....65
2.3.5 Additional remarks regarding the heat transfer during cooling of heated metal object....69
2.3.6 Computational results....70
2.3.6.1 Temperature field....70
2.3.6.2 Comparison of calculated heat transfer coefficients....71
2.3.6.3 The justification of the applied turbulent kinetic energy value....76
2.3.6.4 The C_μ coefficient – a short discussion....79
2.4 Conclusion of Chapter 2....81
3 NUMERICAL SIMULATION OF METAL MATERIAL QUENCHING....82
3.1 Introduction....82
3.2 Related studies....83
3.2.1 Water entry....83
3.2.2 Drag reduction....84
3.2.3 Quenching....84
3.2.4 A brief summary on the related studies....85
3.3 Description of the experiment....86
3.4 Numerical method....87
3.4.1 Description of the case and geometry....87
3.4.1.1 An overview....87
3.4.1.2 Material properties....89
3.4.2 Initial and boundary conditions....91
3.4.3 Moving boundary problem....91
3.4.4 Dynamic mesh handling....92
3.4.4.1 Mesh motion....92
3.4.4.2 Remeshing....92
3.4.5 Computational mesh....93
3.4.6 Turbulence modeling....94
3.4.7 Solution procedure....95
3.5 The heat transfer coefficient....95
3.6 Conclusion of Chapter 3....96
4 RESULTS....98
4.1 Temperature distribution....98
4.2 Heat transfer characteristics....101
4.2.1 Surface A (horizontal bottom surface)....103
4.2.2 Surface B (vertical lateral surface)....105
4.2.3 Surface C (top horizontal surface)....107

4.3 Conclusion of Chapter 4....110
5 CONCLUSIONS AND FUTURE WORK PERSPECTIVES....112
5.1 Introduction....112
5.2 Conclusions....112
5.2.1 Verification part....112
5.2.2 Validation part....113
5.2.3 Application case....114
5.3 Future work....116
5.4 Conclusion of Chapter 5....117
REFERENCES....118
APPENDIX A: THE DERIVATION OF CORRELATION FOR CALCULATION OF LOCAL NUSSELT NUMBER....125
APPENDIX B. THE ESTIMATION OF VAPOR LAYER THICKNESS IN A STABLE FILM BOILING WITH A SMOOTH VAPOR-LIQUID INTERFACE....129
BIOGRAPHY AND A LIST OF SELECTED PUBLICATIONS....131
Biography....131
Selected publications....131
ŽIVOTOPIS I POPIS ODABRANIH PUBLIKACIJA....132
Životopis....132
Odabrane publikacije....132

LIST OF FIGURES

Sl. 1. Prikaz numeričkih rezultata simulacije gašenja uranjanjem: a) polje volumnog udjela parne (kapljevite) faze; b) temperaturno polje unutar krutine.....XVI
Fig. 2. A schematic representation of a *CCT* diagram for a continuous cooling of an undereutectoid steel; the achievement of a fully martensitic structure at the specific location for which the cooling characteristic is plotted.....5
Fig. 3. A conceptual sketch of immersion quenching process: (a) film boiling mode; (b) rewetting of the specimen surface; (c) single-phase convection heat transfer.....11
Fig. 4. Graphical representation of the OCASIMAT model.....22
Fig. 5. A schematic representation of the domain accompanied with the applied boundary conditions and initial phase distribution.....45
Fig. 6. The initial condition of the vapor volume fraction (a) and the vapor temperature (b).....46
Fig. 7. Types of meshes used in computations: (a) uniform quadrilateral, (b) stretched quadrilateral and (c) hybrid of stretched quadrilateral and triangular cells.....46
Fig. 8. Evolution of the interface position using the uniform quadrilateral mesh: (a) for the whole simulation time, (b) the detailed view at the beginning, and (c) near the end of the simulation.....51
Fig. 9. The comparison of temperature at $t = 0.1$ s between the analytical solution and the simulation: whole domain (left) and the closer view near the interface (right).....52
Fig. 10. The vapor and liquid phase's temperature distributions in the domain composed of 100 quadrilateral, uniformly distributed, cells compared with analytical solution and accompanied with distribution of vapor volume fraction: whole domain (left) and the closer view near the interface (right); the markers denote cell center values. The plot represent the result at $t = 0.1$ s.....53
Fig. 11. The distribution of vapor and liquid phase's velocity magnitude field in the domain composed of 100 quadrilateral, uniformly distributed, cells together with the profile of vapor volume fraction: whole domain (left) and the closer view near the interface (right); the markers denote cell center values. At $t = 0.1$ s.....54
Fig. 12. Evolution of the interface position using the stretched quadrilateral mesh: (a) for the whole simulation time, (b) the detailed view at the beginning, and (c) near the end of the simulation.....55
Fig. 13. The comparison of temperature at $t = 0.1$ s between the analytical solution and the simulation: whole domain (left) and the closer view near the interface (right).....56
Fig. 14. Evolution of the interface position using the hybrid mesh: (a) for the whole simulation time, (b) the detailed view at the beginning, and (c) near the end of the simulation.....57
Fig. 15. The comparison of temperature at $t = 0.1$ s between the analytical solution and the simulation: whole domain (left) and the closer view near the interface (right).....58
Fig. 16. Distribution of (a) volume fraction of vapor and (b) vapor temperature for the hybrid mesh.59
Fig. 17. A schematic representation of the validation model with the applied boundary conditions. The dimensions are in mm.....62
Fig. 18. The computational mesh (a), a detailed view on cell distribution in the vicinity of the fluid-solid boundary (b).....63
Fig. 19. A schematic representation of initial temperature field distribution: in radial direction, in vicinity of the vertical surface (left); in the immediate neighborhood of top and bottom horizontal surface (right).....64
Fig. 20. A conceptual sketch on determination of initial temperature in the edge control volume.....65
Fig. 21. The temperature evolution in a solid specimen during approximately first 15 s of the simulation; the data is compared to the experimental results from Momoki et al. [1], extracted using [65]. The dashed line denotes ± 2 % error band.....70
Fig. 22. The calculated heat transfer coefficients using numerical simulation in comparison to ones obtained using Eq. (72).....72
Fig. 23. Transient behavior of: (a) vapor film; (b) temperature evolution in the vapor phase; (c) temperature evolution in the liquid phase.....74

Fig. 24. The comparison of the applied, constant, TKE value obtained using a parametric study and calculated ones using Eq. (64).....77
Fig. 25. The turbulent viscosity (a) and volume fraction (b) field for two different time instances in the conducted simulation of film boiling around a vertical cylinder in a saturated liquid medium.....78
Fig. 26. A view on vapor phase's velocity magnitude (a) and strain rate (b) distrubutions; the strain rate follows closely the interface shape, thus featuring the presence of friction at the interface between the phases.....80
Fig. 27. The experimental investigation of Inconel 600 quenching in quescient liquid-water pool at initial temperature of ca. 52 ºC: (a) immediately before the immersion; (b) after the top of the body has been immersed; (c) at later stage of the immersion quenching process.....87
Fig. 28. An overview of the computational domain with selected boundary conditions; a "Coupled" prescribed boundary condition is ommited from the sketch for the sake of clarity. The dimensions are expressed in mm.....88
Fig. 29. Thermal effusivity of Inconel 600 with respect to temperature.....90
Fig. 30. Thermal diffusivity of the studied material.....90
Fig. 31. A view on computational mesh: (a) the area in the vicinity of the specimen; (b) a broader view.....93
Fig. 32. The initial TKE distribution in the analysed case.....94
Fig. 33. Comparison of the computational result in the vicinity of the specimen center with the data available from the experiment in Landek et al. ; extracted using .The *dashed* lines represent 10 % discrepancy from the experimental data.....98
Fig. 34. Comparison of the surface temperature obtained using the data from experiment in Landek et al. and the simulation data. The dashed lines denote 10 % discrepancy from the published data.....99
Fig. 35. The volume fraction field evolution in time (a) together with the spatial temperature distribution in solid (b), both being addressed during the immersion process.....100
Fig. 36. The vapor volume fraction evolution (a) and temperature field distribution in a solid object (b) during quenching process, whilst the body remains stationary in a liquid medium.....101
Fig. 37. Comparison of calculated heat transfer coefficients by taking into consideration all heat transfer surfaces with the correlation given in Momoki et al. . The dashed lines denote ± 15 % discrepancy from the correlation result.....102
Fig. 38. The overall heat flow rate transferred from the solid specimen during the immersion process, after impact on a free surface level of a liquid quenchant; a comparison with the data obtained using correlations.....103
Fig. 39. Comparison of calculated heat transfer coefficientes on the bottom horizontal surface by use of numerical simulation with the ones obtained with correlation available in Momoki et al. and the investigation of 30 x 3*0* mm cylinder made of silver in 104
Fig. 40. The distribution of the heat flux values at surface A against time.....105
Fig. 41. Comparison of the calculated heat transfer coefficients on the vertical lateral surface with the results obtained using experimental data, presented in Landek et al. , and the ones obtained via the empirical correlation given in Momoki et al. 106
Fig. 42. The heat flux distribution versus time for vertical lateral surface; a comparison between the numerical simulation (instantaneous and the data averaged with respect to time) and the result obtaiend by use of correlation available in Momoki et al. [1].....107
Fig. 43. The heat transfer coefficient distribution on the top horizontal surface, surface C, with respect to time together with the correlation data obtained using the model presented in Momoki et al. [1] and the data availabale in Yamada et al. [102].....109
Fig. 44. The instantaneous, averaged (both simulation) and correlation obtained heat flux values at the top horizontal surface.....110
Fig. 45. The mass transfer process in a three-cell stencil.....126
Fig. 46 A conceptual sketch of the boundary conditions applied in the theoretical according to Yamada et al. [62], and used in obtaining the average velocity for determination of *TKE* here.....130

LIST OF TABLES

Table 1. A brief overview of popular mass transfer models according to Kharangate and Mudawar [18].....20
Table 2. The properties of vapor and liquid at 1.013 bar [46].....44
Table 3. A general, mesh size dependent, time stepping procedures applied for the uniform and stretched meshes.....47
Table 4. Time stepping procedures for the cases of certain hybrid meshes.....48
Table 5. The relative computational error in estimation of interface position at selected two time instances for different resolutions of uniform quadrilateral mesh.....51
Table 6. The maximum relative computational error in estimation of vapor phase's temperature field inside the domain at $t = 0.1$ s for uniform quadrilateral mesh.....52
Table 7. The relative computational error in estimation of interface position at selected two time instances for different resolutions of stretched quadrilateral mesh.....55
Table 8. The maximum relative computational error in estimation of vapor phase's temperature field inside the domain at $t = 0.1$ s for different resolutions of stretched quadrilateral mesh.....56
Table 9. The maximum relative computational error in estimation of vapor phase's temperature field inside the domain at $t = 0.1$ s for different resolutions of hybrid mesh.....57
Table 10. The maximum relative computational error in estimation of vapor phase's temperature field inside the domain at $t = 0.1$ s for different resolutions of hybrid mesh.....58
Table 11. The thermal properties of superheated vapor used in estimation of film boiling heat transfer coefficient at the temperature 350 °C.....72
Table 12. Joint comparison of experimental and the flow fields (volume fraction) obtained with usage of numerical simulation.....75
Table 13. Thermal properties of water and vapor at atmospheric pressure.....96
Table 14. A comparison between the flow field obtained using numerical simulation and experimental finding after the solid is immersed into liquid medium.....108

NOMENCLATURE

Latin symbols

Quantity	Description	Unit
A	cross-sectional area	m^2
A_i	interfacial area density/concentration	m^{-1}
a_v	the thermal diffusivity of the vapor phase	m^2/s
b	thermal effusivity	$Ws^{0.5}/(m\ K)$
C	model constant in rough estimation of two-phase heat transfer coefficient	
c_l	specific heat capacity of the liquid phase	J/(kg K)
$c_{p,s}$	specific heat capacity (at the constant pressure) of a saturated phase in model by Sun *et al.* (2012)	J/(kg K)
c_s	the specific heat capacity of a solid	J/(kg K)
C_{slope}	empirical constant in LES model	
c_v	specific heat capacity of the vapor phase	J/(kg K)
C_v, C_l	vapor and liquid phase's scaling factors, respectively	1
D	the diameter	m
d_1	the shortest length from the mixture cell's center to the interface	m
d_2	the nearest liquid cell control distance	m
d_3	the distance from the closest cell completely filled with liquid to the interface	m
d_{eqv}	the equivalent diameter	m
d_p	characteristic length of the dispersed phase	m
d_v	the diameter of a vapor bubble	m
E_T	the relative error in estimation of temperature field	1
E_{xi}	the relative error in estimation of interface position	1
f_4	function in a lumped heat conduction model	
F_v, F_l	density ratio of vapor and liquid phase, respectively	1
g	gravitational acceleration	m/s^2
$\nabla\alpha$	gradient of the volume fraction field	m^{-1}
h	the heat transfer coefficient	$W/(m^2\ K)$
h'	the specific enthalpy of a saturated liquid	kJ/kg
h''	the specific enthalpy of a saturated vapor	kJ/kg
H	height of a specimen	m
$\bar{h}$	the average heat transfer coefficient for the overall heat transfer surface	$W/(m^2\ K)$
$\bar{h}_A$	the average heat transfer coefficient for the top horizontal surface of a cylinder during film boiling	$W/(m^2\ K)$
$\bar{h}_{B1}$, $\bar{h}_{B2}$	the average heat transfer coefficients at the vertical surface of a cylinder, in the region of the smooth and a wavy vapor-liquid	$W/(m^2\ K)$

	interfaces, respectively	
$\bar{h}_C$	the average heat transfer coefficient at the bottom horizontal surface of a cylinder	W/(m^2 K)
h_c	the heat transfer coefficient in the vicinity of the specimen center	W/(m^2 K)
h_i	the heat transfer coefficient at specific time instance	W/(m^2 K)
h_{pq}	interphase heat transfer coefficient	W/(m^2 K)
$h_{simul.}$	the average heat transfer coefficient obtained by use of numerical simulation	W/(m^2 K)
L	length; total length of a cylinder specimen	m
l_0	characteristic length	m
L_{B1}	the length of the zone of a smooth interface	m
$\dot{m}$	mass transfer rate per unit volume	kg/(s m^3)
M_f	martensite finish temperature	^{o}C
$\dot{m}_{lv}$	mass transfer rate per unit volume in a vapor-liquid phase-change process	kg/(s m^3)
$\dot{m}_{pq}$	mass transfer rate per unit volume for a phase pair	kg/(s m^3)
M_s	martensite start temperature	^{o}C
$\vec{n}$	normal vector	m
n	gradient of level-set function in model proposed by Koseiffi *et al.*	1
n	empirical exponent	
O	the perimeter	m
p	system pressure	Pa
p_{amb}	ambient pressure	Pa
q	wall heat flux	W/m^2
$\vec{q}$	heat flux vector	W/m^2
q_l	heat flux from liquid to the interface	W/m^2
q_m	mass flow rate	kg/(s m)
$\dot{q}_m$	interfacial mass transfer rate	kg/(s m^2)
q_v	heat flux from vapor phase to the interface	W/m^2
r	position vector	m
r_0	specific heat of vaporization	J/kg
r_G	the position vector in model by Perez-Raya and Kandlikar (2018)	m
r_i	empirical constant in Lee model	s^{-1}
$\vec{R}_{pq}$	general representative of the interface drag term	kg/(m^2 s^2)
S_e	heat flux at the interface (source term)	W/m^2
T	thermodynamic (absolute) temperature in degrees Kelvin	K
t	time	s
T'	saturation temperature	K
T_∞	the free stream temperature	K
T_a	analytical solution to temperature field in solution to Stefan problem	K
$T_{cell,i}$	the temperature in the cell center of i-th cell	K
t_{end}	the simulation end time	s
T_G	the temperature in the nearest cell filled with	m

	liquid, i. e., the G-cell	
$t_{\text{inc. Min}}$	incubation time in quenching process	s
TKE	turbulent kinetic energy (specific)	m^2/s^2
T_l	liquid phase's temperature	K
T_lin	the temperature calculated using linear law (plane wall)	K
T_ln	the temperature calculated using logarithmic profile (cylindrical coordinates)	K
T_M	temperature in the mixture cell	K
T_n	the temperature as a result of numerical simulation	K
t_total	the total simulation time	s
T_v	the temperature of the vapor phase	K
T_w	the wall temperature	K
u_p	p-th phase velocity	m/s
V_c	cell volume	m^3
$V_{\text{c},i}$	the volume of i-th cell	m^3
$\vec{v}_q$	the velocity of the phase q (either vapor or liquid)	m/s
v_g	growth velocity	
v_Kr	critical cooling speed	m/s
v_ohl	cooling speed	m/s
w	flow velocity	m/s
$\overline{w}$	average velocity in a vapor film	m/s
X	interface position	m
x	spatial coordinate	m
$X'(t)$	the interface velocity	m/s
$X(t)$	the interface position	m
x_{ci}	x-coordinate of ci-th cell's center	m
$x_{\text{c},i}$	the axial coordinate of i-th cell's center	m
$X_{i,\text{a}}(\text{t})$	x-coordinate of interface position obtained by use of analytical solution to Stefan problem	m
$X_{i,\text{n}}(t)$	x-coordinate of interface position obtained by use of numerical solution	m
$y_{\text{c},i}$	the radial coordinate of cell center of i-th cell	m

Greek letters

Quantity	Description	Unit
α_l	the volume fraction of a liquid phase	1
α_v	the vapor volume fraction	1
γ	accommodation coefficient in the Schrage model	1
δ	vapor film thickness	m
$\overline{\delta}_\text{m}$	the average vapor film thickness	m
$\widetilde{\delta}_\text{m}$	the average dimensionless film thickness	1
$\widetilde{\delta}_{\text{B, 0}}$	the dimensionless initial layer thickness due to inflow from beneath the cylinder	1
ΔT_0	the bubble initiation temperature difference	K
Δt_i	the sampling time interval	s
Δt_s	the applied time step in the model of Stark	s

Quantity	Description	Unit
	and Fritsching	
ΔT_w	wall superheat	K
Δx	the approximated cell size	m
Δx_c	the length of the wall adjacent cell	m
ε_{ij}	strain rate tensor	m-1
η	the similarity variable	$m/s^{0.5}$
ϑ	temperature in degrees Celsius	°C
ϑ_{bulk}	the temperature of the bulk fluid	°C
ϑ_m	average temperature	°C
ϑ_s	solid temperature	°C
ϑ_{surf}	surface temperature	°C
λ	molecular thermal conductivity of a material	W/(m K)
λ_{eff}	effective thermal conductivity	W/(m K)
λ_{liq}	thermal conductivity of the liquid phase	W/(m K)
λ_s	thermal conductivity of a solid material	W/(m K)
λ_t	turbulent thermal conductivity	W/(m K)
λ_{uns}	thermal conductivity of the unsaturated phase	W/(m K)
λ_{vap}	thermal conductivity of a vapor phase	W/(m K)
μ_v	the dynamic viscosity of a vapor phase	Pa s
ν_v	the kinematic viscosity of a vapor phase	m^2/s
ξ	interface position constant	$m/s^{0.5}$
ρ	fluid density	kg/m^3
ρ_{mix}	the mixture density	kg/m^3
ρ_s	the density of the solid	kg/m^3
ρ_l	density of the liquid phase	kg/m^3
ρ_v	the density of the vapor phase	kg/m^3
σ	surface tension	N/m
$\bar{\bar{\tau}}_q$	the q-the phase stress-strain tensor	$kg/(m^2\ s^2)$
ϕ	kinetic mobility coefficient in Schrage equation	
χ	the similarity variable at the interface	
Φ_{cell}	the volumetric heat flow rate in a single computational cell	W/m^3
Φ_l	the heat flow rate from the interface to the liquid phase in a vapor-liquid phase change process	W/m^3
Φ_v	the heat flow rate from the interface to the vapor phase in a vapor-liquid phase-change process	W/m^3
Φ_{limit}	limiting volumetric heat source value in the model by Stark and Fritsching	W/m^3

Abbreviations

A	austenite phase
ACCI	AVL-code-coupling-interface
AIAD	algebraic interfacial area density
ALE	arbitrary Lagrangian-Eulerian

ALS	air lubrication systems
BiCGSTAB	stabilized bi-conjugate gradient method
BIT	bubble induced turbulence
CCT	continuous-cooling-time
CFD	computational fluid dynamics
CHF	critical heat flux
CHT	conjugate heat transfer
CLSVOF	coupled level-set VOF
CV	control volume
DFFB	dispersed flow film boiling
DNB	departure from nucleate boiling
DNS	direct numerical simulation
DOF	degrees of freedom
FMENA	University of Zagreb's Faculty of Mechanical Engineering and Naval Architecture
FEM	finite element method
FVM	finite volume method
GCL	geometric conservation law
GLIM	generalized large interface model
GUI	graphical user interface
IB	immersed boundary
IHTA	inverse heat transfer analysis
ITM	interface tracking method
LBM	large bubble model
LES	large-eddy simulation
LIM	large interface model
LSM	level-set method
M	martensite phase
M-CFD	multiphase computational fluid dynamics
MBDR	micro bubble drag reduction
MLH	mixing length hypothesis
MM	mixture model
MMAT	multi-material
P	pearlite phase
PDE	partial differential equation

PSI-BOIL	paralel simulator for boiling flows
SPH	smoothed particle hydrodynamics
TFM	two-fluid model
TTT	temperature-time-transformation
UDF	user defined function
VOF	volume-of-fluid

1 INTRODUCTION

1.1 Motivation

The sustainable development of the world's leading economies is strongly linked with optimized power engineering and metal processing industries. However, it is less known that these two industrial branches require well-optimized processes that involve boiling phenomena, to operate smoothly. Thus, the nucleate boiling regime is preferred among thermal power plants, since it allows for the removal of high heat fluxes with relatively small temperature differences at the heat transfer surface. Exceeding this limit, i.e., by surface overheating, may lead to a failure of the system with catastrophic consequences. This is the so-called film boiling regime. However, this unfavorable boiling mode in power plants is very common in the metallurgical quenching process, that is, the rapid cooling of a metal object to achieve certain microstructure that yields desired mechanical properties of the same, for example, hardness. To this end, a comprehensive set of experimental data is needed to achieve the safe and environmentally friendly work of these plants. But this experimental work is very costly and should be preceded by comprehensive theoretical and computational studies to extract the benefit from it. However, the computational studies of boiling incorporate very resource-demanding interface tracking methods (ITMs), that require very fine grid resolutions to model the interfacial phenomena; well known as the single-fluid methods, such as, for example, Volume-of-Fluid (VOF), coupled with Direct Numerical Simulation (DNS) of interface motion, in which the volume fraction of vapor/liquid is tracked by solving the advection equation. On the other hand, two-fluid methods can overcome this but require adequate closure models. Compared to the aforementioned single-fluid models, a two-fluid model is considered to be able to predict more accurate results on coarser mesh owing to the unnecessity of resolving the interface geometry/shape, though two sets of momentum and energy equations must be solved. However, due to the averaging process in the formulation of the governing equations, the shape, and area of the liquid-vapor interface are lost, and the dynamics related to the interface, e.g. surface tension and interphase forces, cannot be directly computed.

The increased hardness obtained by martensitic microstructure is, to a first approximation, the desired mechanical property that is to be achieved via the immersion quenching process of steels; to this end, the cooling process has to be carried out with the appropriate

temperature-time cooling characteristics. Whilst the metallographic phenomena inside the material are generally well understood, the boiling phenomena that prevail in the quenching process are still relatively unknown.

In brief, the main outcome of the present research can be summarized as follows. The key to successful numerical simulation of the phase change process studied here is in the correct estimation of the heat flux at the vapor-liquid interface that, in the case of the liquid at saturation temperature, reads:

$$\vec{q} = -\lambda_{uns} \frac{d\vartheta}{d\vec{n}}; \tag{1}$$

with λ_{uns} being the thermal conductivity of the unsaturated phase in a phase-change process in a laminar flow; however, since the industrial context imposes the application of turbulent flow, Eq. (1), should be reformulated as follows:

$$\vec{q} = -\lambda_{eff} \frac{d\vartheta}{d\vec{n}}; \tag{2}$$

with λ_{eff} being the sum of molecular and turbulent thermal conductivity, i. e., $\lambda_{eff} = \lambda + \lambda_t$, but of the continuous phase (liquid in the case of metal quenching),

The quenching process is taking place at the finally stages of the steel manufacturing process. So, it is very important to be carried out properly to minimize the manufacturing costs and maximally reduce the expenses associated with the failures in the heat treatment process.

Therefore, the proposed research is aimed at the modeling of film boiling using a two-fluid VOF model, with a long-term goal to model the complete boiling curve, starting from film boiling thereof. The method is implemented in the industrially relevant package ANSYS Fluent.

1.2 Quenching process

The heat treatment process in general consists of heating and cooling cycles to make changes in material properties as a result of changes in its structure. The heating process can be realized, for example, in a furnace and consists of three time intervals:

1. heating until the material surface reaches the predefined temperature ϑ_s;
2. heating or holding until the acceptable level of temperature uniformity is achieved, that is, $\vartheta_c \approx \vartheta_s$;
3. holding at predefined temperature for achievement of homogeneous chemical composition and phase transformation in the full microstructure of a treated part.

All these steps are characterized by diffusion-intensive microstructural transformations. On the other hand, if cooling is considered, the overlapping transformations overcome the diffusion ones. The first time interval refers to the time that is necessary for the outer surface of the material to achieve the desired temperature; it is succeeded by the time needed for the core to achieve nearly the same temperature. This is determined by the "thermodynamics thickness" of the material, represented by the dimensionless Biot number that reads:

$$Bi = \frac{h\, l_0}{\lambda_s}, \tag{3}$$

where h is the heat transfer coefficient, W/(m^2 K), l_0 is the characteristic length, m, and λ_s is the thermal conductivity of a solid material, W/(m K). This number physically represents the ratio between thermal resistance to a conduction heat transfer in a solid and a convection heat transfer in a boundary layer of a liquid surrounding the solid body; analogously as the Nusselt number corresponds to the thermal resistance between the conduction and convection (both on a fluid side) for a fluid medium. In heat treatment, as noted in [3], if $0 < Bi \leq 0.25$ the material is, say, "thermodynamically thin" and will faster achieve the temperature uniformity since it posses lower thermal inertia; a vice-versa is relevant for the "thermodynamically massive" material with $Bi > 0.25$. Note that this criterion differs from the one that is present in the heat transfer textbooks, e.g. in [4], that is, $0 < Bi < 0.1$, which refers to complete neglecting the spatially distributed temperature gradients and thus reduction of the heat conduction partial differential equation (PDE) to a simple form:

$$\vartheta(t) = \mathrm{f}_4, \tag{4}$$

that precedes the classical lumped unsteady temperature distribution model. The third phase in the heating process refers to the time needed for diffusion-determined structural transformations to occur. This period is aimed at the homogenization of the material's structure. According to Liščić *et al.* [5], the complete heating section of the heat treatment process is generally well understood and automated; hence, there is no need for special attention herein. In terms of heat treatment of steels, a process is termed quenching if the material has been rapidly cooled down from so-called austenitization temperature, that is, the temperature at which mono- or bi-phasic austenitic microstructure is achieved, to increase, in the most general case, the material hardness by the achievement of a fully martensitic structure after cooling; taking care thereby not to overreach the recommended austenitization temperature limits to achieve the desired size of the austenitic grain. The austenitization temperature is carbon content dependent; under-eutectic steels (carbon content lower than 0,8 %) require higher temperatures than the steels with higher carbon content, i.e. the over-eutectic steel (carbon content in a range from 0,8 % to 2,03 %). The structural transformations that occur during the quenching process can be successfully tracked using Continuous Cooling Transformation (CCT) diagram for continuous cooling by the involvement of cooling characteristics, Fig. 2. These diagrams are experimentally determined for every steel on a commercial market, and they are valid for the specific chemical composition of tested steel and austenitization parameters. The very slow cooling processes (i.e. with cooling rate lower than 1 K/s, e.g. cooling in a furnance) could be tracked in Fe-Fe_3C diagram for carbon steels or in pseudo binary diagrams for alloyed steels. For very fast cooling rates in quenching of steels (e.g. water cooling), the martensite transformation start, M_s, and martensite finish, M_f, temperatures could be determined from Upton's diagram. The M_s temperature is also shown in the Temperature-Time-Transformation (TTT) diagram of quenched steel.

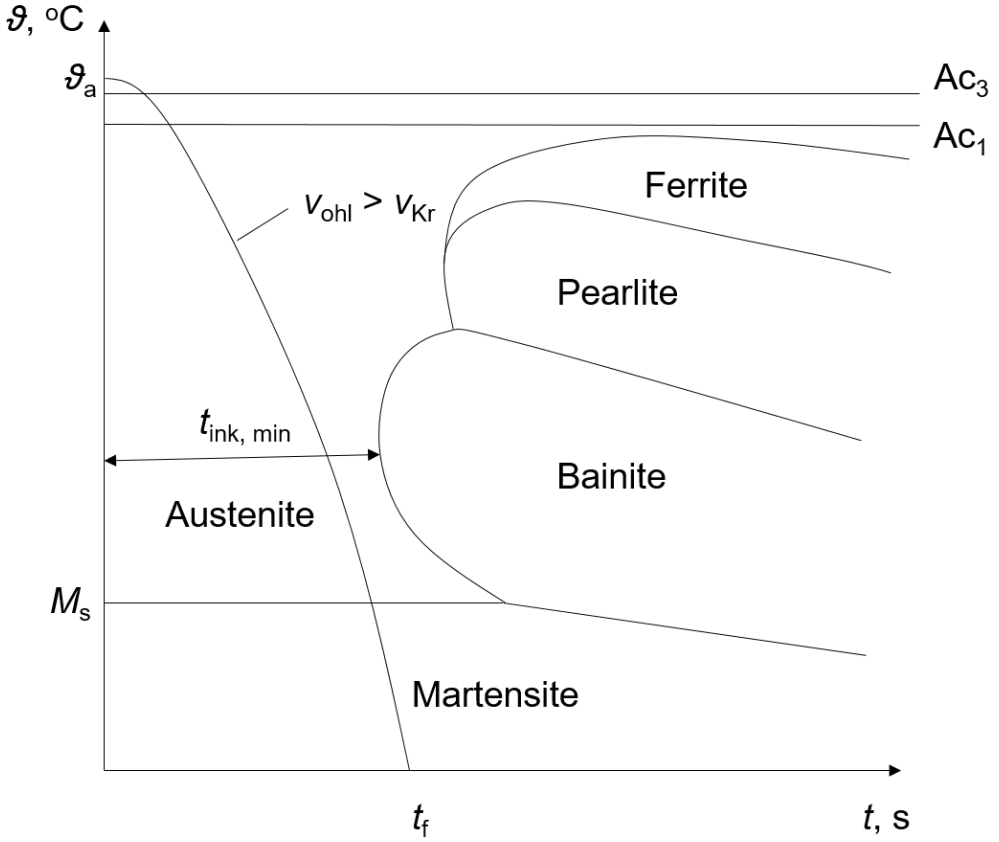


Fig. 2. A schematic representation of a CCT diagram for a continuous cooling of an undereutectoid steel; the achievement of a fully martensitic structure at the specific location for which the cooling characteristic is plotted.

Apart from the Fe-Fe_3C diagram, intended for very slow, equilibrium cooling (and heating) processes, and Upton's diagram for very fast cooling processes, the CCT diagram can represent the structural transformations under realistic cooling rates. The cooling rate can be obtained thereof by finding a tangent on the temperature distribution in the time frame with the temperature range from 800 °C to 500 °C, abbreviated as $t_{8/5}$, since in this temperature limits the change in temperature profile is slowest. In an ideal case of continuous steel quenching, the structural transformation from austenite to martensite would be deduced from the cooling curve in a CCT diagram for continuous cooling. Especially critical is thereby the temperature range from, according to Krumes [3], approximately 650 °C to approximately 400 °C where structural transformation may occur. These limits belong to the aforementioned temperature range $t_{8/5}$ where the temperature gradient ($d\vartheta/dt$) experiences the lowest change and also is characterized by a significant decrease in the temperature of the material since the nucleate boiling takes place

with corresponding high heat flow rate extraction. The main purpose of the quenching process is to achieve a fully martensitic structure when cooled from the austenite phase, thus avoiding the possible transformation into pearlite or bainite phase during the process. The pearlite phase is characterized by the possession of high ductility and low hardness in contrast to martensite, which has high hardness and low ductility; this contrast in phase properties is not suitable, for example, in the case of high dynamic loads in the operation of a material. On the other hand, the bainite phase has properties similar to those of martensite, but it is difficult to achieve it in a continuous cooling process; it rather can be achieved in an isothermal process (e.g. in a bath). The quenching is realized using the quenching mediums, quenchants, the fluids that can be categorized into three groups:

- The first group of quenchants is characterized by the occurrence of Leidenfrost point, that is, the formation of a stable vapor blanket immediately after the austenitized steel material is subjected to the medium; water, oil, and water-based solutions represent these types of quenchants.
- The second group of quenchants is the one whose boiling point is above the austenitization temperature of the steel; liquid metals and salt baths belong to this group.
- The third group of quenchants is gases, used in the cases of highly alloyed steels; air (quiescent or compressed), N_2, Ar, He. The vacuum also belongs to this group.

The main representatives of the first type of quenchants, water, and oil, differ in cooling rate; the water has a shorter period in the critical temperature range for structural transformations to occur, which is very good, but also after the martensite start temperature is reached, which may lead to significant stress generation (thermal and transformation stress).

In the second type of quenchants, the generation of the vapor phase is avoided, due to the melting temperature that is higher than the austenitization temperature. However, in some cases, environmental hazards may occur (e.g. hazardous Pb vapor). The third type of quenchants are suitable for highly alloyed steels and are characterized by small structural deformations due to low heat flow rates in the case of gas cooling.

From the heat transfer point of view, and the corresponding fluid flow, only the first type of quenchants involve the multiphase flow with heat transfer and phase change; the other two are dominantly characterized by a single-phase convection cooling.

To be quenched, the steel material has to fulfill the following conditions:

1. The existence of $\alpha \rightarrow \gamma$ metal cell transformation;
2. The sufficient carbon content;
3. Heated up to austenitization temperature, since the martensite can be achieved only from the austenite phase;
4. Cooled fast enough to ensure the transformation from austenite to martensite phase.

The fully martensitic structure can be achieved with a mild cooling rate if the steel is alloyed with α- or γ-genic alloying elements. Thus, the incubation time, $t_{\text{inc. min.}}$, is prolonged, that is, the transformation lines are shifted to the right in the CCT diagram.

In conclusion, the main outcome of the quenching process is, to a first approximation, the achievement of the desired material hardness. To this end, the steel material is firstly heated up to the austenite (A) phase and then rapidly cooled by immersion in a quenchant medium to the martensite (M) region. This is the so-called overlapping (diffusionless) transformation and may be applied to steels with A → M transformation to improve their mechanical properties, e. g. hardness. To estimate the hardness level that may be achieved by the quenching process, one needs to be acquainted with the cooling characteristic of a material, that is, the unsteady temperature distribution that is tracked in the CCT diagram. To accomplish this, a heat conduction equation needs to be solved in a solid, considering thereby the imposed heat and flow conditions in the surrounding, quenchant, medium. While the phenomena occurring inside the solid material has been extensively studied in the past and is generally well understood, the important features of coupled processes during immersion cooling are still relatively unknown. This is primarily due to the occurrence of boiling phenomena during the process, since the initial material temperature by far exceeds the saturation temperature of the quenchant medium. Thus, the correct estimation of the phase change process is needed to accurately model the heat transfer in a solid. More details about the boiling process are given in the next subsection.

1.3 Boiling

Consider a pool of water heated at the bottom surface, as is usually presented in standard heat transfer textbooks. After a sufficient amount of heat is transferred to a layer in the vicinity of the heated surface, especially if there is roughness with finite radii, $R > 0$, a vapor bubble may appear. The bubbles are generated at the so-called nucleation sites, whose number also depends on the heat flux at the heated surface. Once generated, the bubble receives the heat input from

the bulk liquid, since the liquid is in a meta-stable superheated state, and evaporates at the interface between the vapor and liquid. Thus the vapor bubble grows and, at a certain time instance, detaches from the nucleation site with the frequency of detachment that depends on the heat load imposed at the bottom surface. To transfer the heat from the liquid to vapor some, at least small, temperature differences exist. Thus, the temperatures of the vapor and liquid phase are different. The forces that act on a single bubble involve surface tension force, gravity force, and inertia force. In absence of gravity, the force balance yields a Laplacian pressure jump across the interface. Although favorable, in terms of bubble nucleation, it is not mandatory to have surface roughness to initiate the boiling process; thus it may appear at a perfectly smooth surface, such as a Hg surface, or higher superheats of a heat transfer surface.

If we consider boiling in a pool in the way it was done in the experiment by Nukiyama (1934), different boiling modes will occur under different heat loads. Thus, at the beginning we shall observe the convective boiling phase, that is, the boiling takes place at the free surface of the liquid pool. Further increase in heat input into the pool of water will lead to the generation of bubbles, that is, the nucleate boiling mode; characterized by high heat outputs at moderate temperature differences, a favorable, therefore, boiling mode in power engineering devices such as boilers. However, if a critical heat flux (CHF) point is exceeded, the heat transfer surface cannot be attained by the liquid anymore, since the vapor blanket surrounds the hot object, thus significantly reducing the cooling rate and causing high temperatures at the heat transfer surface. This is the film boiling mode and, apart from the fact that is unfavorable in power engineering devices, since it may cause the deterioration of the heat transfer surface, is very common in metallurgy, wherein a vice-versa situation is common in cooling of a heated solid in a liquid medium. Firstly, due to extremely high heat input, film boiling occurs. After the surface temperature reaches the minimum point, that is, the Leidenfrost, also known as the re-wetting temperature, the vapor film collapses and an immediate transition to nucleate boiling takes place. The transition boiling region, however, may be achieved in the case of the constant temperature of a solid surface instead of controlled heat flux; thus the intermittency between the nucleate and film boiling mode is present in the vicinity of the heat transfer surface.

From the viewpoint of the heat transfer coefficient, it reaches its maximum value slightly before departure from the nucleate boiling (DNB) point is reached, and decreases rapidly after it. Its slight increase after the Leidenfrost temperature exhibits flatter distribution in comparison to the nucleate boiling case. Before further examination of boiling heat transfer during the immersion

quenching process, a brief note on some fundamental issues in convective heat transfer regarding the estimation of the heat transfer coefficient, is given in the following two subsections.

1.3.1 Single-phase convection

The heat can be transferred by convection whether the motion of the fluid is induced by density (natural convection) or pressure (forced convection) differences. An analysis of single-phase convection stems from a control volume, wherein the temporal and spatial change of dependent variables is tracked using the laws of classical physics, namely: the conservation of mass, momentum, and energy; formulating thereby the set of partial differential equations (PDEs). The application of similarity theory in this equation set yields the dimensionless numbers used in the classification of the studied convection heat transfer case. Thus the Reynolds number, *Re*, is used in forced convection problems together with the Prandtl number, *Pr*, since it represents the ratio between the inertia and viscous (friction) forces, while the Grashof number, *Gr*, considers the strength of buoyancy forces and is used in the analysis of natural convection heat transfer, also in conjunction with *Pr*; the modes have in common the application of Nusselt number, *Nu*.

The main outcome of convection analysis is obtaining the heat transfer coefficient, *h*, that relates the heat flow rate transferred through the finite size heat transfer surface and the respective temperature difference between the solid surface and surrounding fluid medium. In doing so, the application of dimensionless numbers is a straightforward approach.

1.3.2 Two-phase convection

The convection heat transfer, i. e., the heat transfer coefficient in a two-phase flow with heat transfer can be roughly expressed as:

$$\alpha = C \cdot q^{n}, \tag{5}$$

where *C* is the model constant which depends on the fluid properties at a certain pressure level and solid medium, in particular, the thermal conductivity and the surface roughness; *q* is the

wall heat flux, whose higher value means more activated nucleation sites; and n is the empirical exponent.

It is noteworthy that the heat transfer coefficient, in the case of pure natural convection during pool boiling, is by far mostly influenced by the presence of a phase change process; in terms of forced convection flow, the flow itself contributes considerably lower to the overall heat transfer than the presence of phase change process. Thus, the correlation for natural convection boiling flow may be also used in the case of forced convection, since the phase change has the dominant influence on the heat transfer coefficient [5].

This is, however, not valid in the case of dipping the metal object into a liquid medium, since the solid temperature is above the Leidenfrost temperature and the film boiling takes place. Further cooling of the solid, and passing the Leidenfrost temperature yields nucleate boiling; the transition boiling mode, that precedes the nucleate boiling, according to [5] may be neglected for practical considerations. When the surface temperature falls below the saturation temperature, the nucleate boiling is replaced with the single-phase convection heat transfer.

1.3.3 Immersion quenching

In the immersion quenching technique, the material is dipped into a liquid medium; the temperature of the solid material exceeds the boiling temperature of the liquid and also the Leidenfrost temperature; hence, the film boiling takes place, as depicted in Fig. 3a. The vapor blanket, that appears during the film boiling regime, surrounds the body if it is a sphere, but not in the case of a cylinder, where it collapses at the bottom edge and the rewetting front advancing from the bottom surface of the cylinder shall be observed therein, see Fig. 3b. Finally, a single-phase convection heat transfer takes place (Fig. 3c).

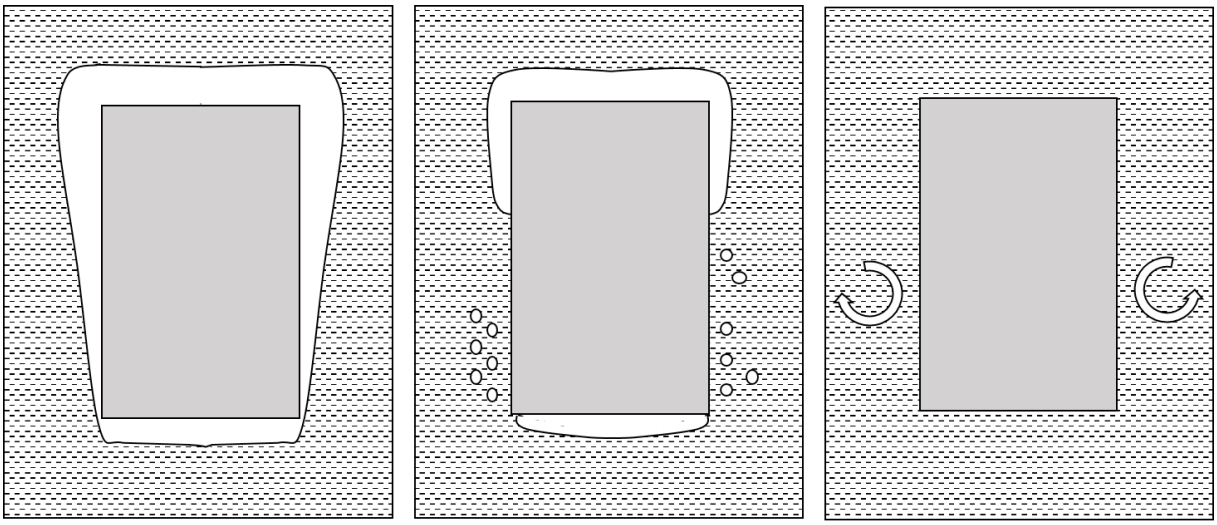


Fig. 3. A conceptual sketch of immersion quenching process: (a) film boiling mode; (b) rewetting of the specimen surface; (c) single-phase convection heat transfer.

The Leidenfrost temperature is higher if the dimensions of the specimen are smaller, the water is agitated ($w \neq 0$) and the bath is subcooled to a higher extent. From the viewpoint of heat transfer in the vapor film, it is most widely adopted that heat conduction is the dominant mode, albeit thermal radiation is also present therein; however, it can be neglected due to its small contribution in contrast to the heat conduction, as is briefly quantified in [5].

In stable film boiling the vapor film thickness is higher if the bath temperature is increased, which can be roughly quantified by an expression:

$$\delta = \frac{\lambda_{\mathrm{vap}}}{\dfrac{q_{\mathrm{m}} r_0}{A\left(T_{\mathrm{w}} - T'\right)}}, \tag{6}$$

where the contributions of bath subcooling and thermal radiation are neglected; that is the bath is considered at the saturation temperature together with the zero-emissivity of the specimen surface. Thus the resistance to the evolution of vapor blanket thickness is minimized, i.e., the vapor blanket thickness will depend primarily on the temperature difference between the specimen surface and the bath.

Higher bath temperatures, however, yield lower thermomigration, thus the heat transfer coefficients are lower during stable film boiling in a saturated liquid. The rewetting velocity is also lowered as the bath temperature is increased. As per Tensi [6], the knowledge of rewetting behavior in terms of knowing the rewetting velocity yields an accurate estimation of temperature distribution during the film boiling regime. The rewetting phenomenon may be involved in the simulation via the input of the space-time-dependent heat transfer coefficient in an inverse heat transfer analysis, as noted in Felde *et al*. [7].

The incipience of film boiling transition to rewetting phase would occur at somewhat higher temperatures (earlier) in the case of higher subcooling. The higher the subcooling, the higher is the temperature at which the transition appears. Thus the transition point may appear much earlier if the same cylindrical specimen is cooled down in a liquid medium at 25 ^{o}C or 40 ^{o}C, than in the case of, e.g., 95 ^{o}C, where it will be at some lower temperature.

The formation of a vapor blanket depends significantly on the specimen's geometry. Thus spherical object will be completely covered with the vapor film, while the cylindrical specimen would have a break-up at the lower edge, where the rewetting starts; as a compromise the cylinder with rounded bottom (semi-spherical) would yield the presence of rewetting at the lower temperatures, in comparison to one with a flat bottom and sharp edge.

The significant influence is played by the convection, the natural or forced. In oils and aqueous polymer solutions, forced convection has some additional impacts on heat transfer. In the case, for example, of quenching of a prismatic cylinder, the convection, that is, the imposed agitation velocity of the bath medium would not affect the rewetting start temperature, but its higher value will significantly reduce the temperature at which the rewetting process ends.

The heat transfer characteristics of the immersion quenching process are also important for the quantification of stress level in the material, that is, the residual stress caused due to transformation (volume change) and thermal (shrinking) stresses that are present during this transformation dominant process (in contrast to transformation-free processes, such as annealing). The residual stresses are the stresses generated in a solid material without being exposed to external force and/or moment; its resulting force or moment has to be equal to zero.

One may distinguish between three types of residual stresses, namely, the residual stresses of the first, second, and third kinds; the first being represented at the macroscopic level, whilst the last two being more microscopic; hence, the residual stresses of the first kind are the most relevant for practical purposes. In the estimation of stress level, the temperature gradients inside the material together with the temperature difference between the specimen center and slightly beneath the outer surface are significant; thus the impact of specimen dimensions (greater diameter → higher radial temperature gradients) and selected quenchant (sharp cooling rate in water; more moderate in oil) medium is of high importance.

1.3.4 A summary of boiling processes

In conclusion, the goal of the selected cooling technique is to minimize the stress level inside the material caused by the residual stresses; the stress generated in the workpiece is more pronounced during quenching in water, in contrast to oil quenching, due to higher cooling rates that are achieved, especially in the martensite transformation range. Since this is not a topic of the present work, the stress distributions would not be further considered in greater detail in this text. Furthermore, for the simulation of the immersion quenching process, it is of vital importance to get acquainted with the adequate modeling of boiling phenomena. Some of the published approaches aimed in this regard are reviewed in the forthcoming section.

1.4 Literature review

1.4.1 Fundamental studies

The relevant fundamental studies refer to the investigations that are focused more on microscopic phenomena and can be used for validation or verification purposes. The primary focus of the fundamental studies presented herein is the occurrence of film boiling in small-scale systems under, to a great extent, idealized physical conditions. This is mostly directed to computational studies, but there is also one experimental work that surpasses these conditions.

Two main verification studies are relevant when numerical methods for the computation of film boiling are considered: the one-dimensional Stefan problem and the two-dimensional bubble

growth case. Whilst Stefan problem refers to planar interface evaporation, the bubble growth shows the method's capability to handle the phase-change process with non-planar interfaces. Some studies consider only one of these two cases, such as in Pan *et al.* [8], Kim *et al.* [9], Koseiffi [10], and Sun *et al.* [11]; whilst, on the other hand, in Sato and Ničeno [12] and Perez-Raya and Kandlikar [13] both cases were examined.

The studies that incorporate empirical modeling approaches generally do not consider these fundamental issues and are predominantly presented in the next subsection.

The mass transfer model based on energy jump condition at the interface can be found in the study by Nichita [14]. The model is implemented within ANSYS Fluent as a part of coupled Level-set Volume-Of-Fluid (CLSVOF) approach in the set of governing equations method via the source term in mass and energy conservation equations. Thus the interfacial mass transfer rate, expressed in units kg/(m^2 s), is given by:

$$\dot{q}_{\mathrm{m,v}} = \frac{\left(\lambda_{\mathrm{l}}\alpha_{\mathrm{l}} + \lambda_{\mathrm{v}}\alpha_{\mathrm{v}}\right)\left(\nabla T \cdot \nabla \alpha_{\mathrm{l}}\right)}{r_0} = -\dot{q}_{\mathrm{m,l}}, \tag{7}$$

where subscripts *l* and *v* denote the mass flow rate due to phase change, thermal conductivity, and volume fraction of liquid and vapor, respectively; whilst r_0 is the specific heat of vaporization. This source term is involved in the mass conservation equation; its multiplication with the specific heat of vaporization yields the following expression for the heat flux:

$$S_{\mathrm{e}} = -\dot{q}_{\mathrm{m,v}} r_0, \tag{8}$$

which is the source term responsible for modeling energy transport across the interface in a phase change process. This mass transfer model has been applied in the computation of vapor bubble evolution in two different mediums, water, and R134a, by taking into account the dynamic contact angle.

A slug flow in a microchannel has been studied in Magnini [15]. The considered cases include isothermal flows; flows with heat transfer and flows with phase change, that is, the evaporative flows. The commercial software ANSYS Fluent has been extended in the direction of curvature calculation in the computation of surface tension body force in a single-fluid VOF model. To

this end, a height function algorithm has been implemented within the software and validated against the already available interface reconstruction algorithm in the software. Furthermore, an evaporation model has been also included; however, since the method is aimed at micro-scale simulations, the assumption of thermodynamics equilibrium at the interface does not hold anymore, that is, the temperature of the interface differs from the saturation temperature. Thus, the mass transfer is incorporated via the source term in the mass conservation equation as:

$$S_{\mathrm{m}} = \phi[T_{\mathrm{M}} - T'(p_{\mathrm{amb}})]|\nabla \alpha|, \tag{9}$$

where ϕ is the kinetic mobility coefficient, T_{M} is the interface temperature, T' is the saturation temperature at the system pressure, p_{amb}, and the last term is the magnitude of the volume fraction gradient, $\nabla\alpha$. The analyzed cases involve, among others, static droplet case, as verification for the calculation of curvature and determination of corresponding spurious velocities; elongated bubble flow under isothermal conditions in horizontal and vertical channels; and elongated bubble flow with heat transfer and phase change.

Another modified formulation of the energy jump mass transfer model and its application in film boiling relevant studies is proposed by Sun *et al.* [11]. The model is applied in solution to a one-dimensional Stefan problem and a film boiling on a horizontal surface, assuming thereby co-existence of saturated and unsaturated phases in the domain. Therefore, due to the reduction of the energy balance at the interface, only the temperature gradient on the unsaturated phase is relevant for the phase change process and the expression for the mass transfer rate per unit volume, kg/(m^3 s), reads:

$$\dot{m}_{\mathrm{s}} = -\dot{m}_{\mathrm{uns}} = \frac{2\lambda_{\mathrm{uns}}(\nabla \alpha_{\mathrm{uns}} \cdot \nabla T)}{r_0}, \tag{10}$$

with λ_{uns} as the thermal conductivity of the unsaturated phase, r_0 as the specific heat of vaporization, $\nabla\alpha_{\mathrm{uns}}$, and ∇T being the volume fraction and temperature gradient of the unsaturated phase, respectively. Furthermore, the equality of specific heat capacities of the phases, $c_{\mathrm{p,uns}} = c_{\mathrm{p,s}}$, and zero thermal conductivity of the saturated phase, $\lambda_{\mathrm{sat}} = 0$, are incorporated into the model. The model is incorporated in commercial CFD code ANSYS Fluent. The geometrical reconstruction method is applied for near-interface interpolation; the convective terms of energy and momentum equations are discretized using a third-order MUSCL scheme,

whilst the pressure-velocity coupling is accomplished by the application of the fractional step method.

A mass conservative method for the computation of phase change processes using a sharp interface representation is proposed by Sato and Ničeno [12]. The mass transfer rate is computed directly from the heat flux at the interface, thus allowing for the sharp distribution of the dominant mass transfer rate in the interface region; the interface thereby being denoted as an iso-surface (iso-line in 2 D) of the phase indicator (color function) equal to 0.5, and the cells bisected by this surface being marked as the interface cells. In the evaluation of temperature gradients, the orthogonal distances between the center of the interface cell and the interface are used. The interfacial mass transfer rate is computed as:

$$\dot{q}_{\mathrm{m}} = \frac{q_{\mathrm{l}} + q_{\mathrm{v}}}{r_0}, \tag{11}$$

where q_{l} and q_{v} are the heat fluxes from the liquid and the vapor phase, respectively, to the interface, r_0 is the specific heat of vaporization. The heat fluxes to the interface, q_{l}, and q_{v}, are calculated as:

$$q_{\mathrm{l}} = \lambda_{\mathrm{l}} \nabla T_{\mathrm{l}} \cdot \vec{n} \; ; q_{v} = -\lambda_{\mathrm{v}} \nabla T_{\mathrm{v}} \cdot \vec{n}, \tag{12}$$

with $\vec{n}$ as the outward pointing normal at the interface, directed from the vapor to the liquid phase. The mass transfer rate per unit volume, i. e., the volumetric mass transfer rate, is given by:

$$\dot{m} = \dot{q}_{\mathrm{m}} \frac{A_{\mathrm{i}}}{V_{\mathrm{c}}}, \tag{13}$$

where A_{i} is the interfacial area and V_{c} is the cell volume. The saturation temperature is imposed at the interface as the boundary condition, thus avoiding the need for the involvement of specific heat of vaporization in the energy conservation equation. The method is implemented within PSI-BOIL, in-house computational software for boiling flows, and the model validation is carried out using a three-dimensional bubble rise case in a zero gravity condition, preceded by classical one-dimensional verification studies. The verification conducted using a bubble growth

case shows the method's capability to work with non-planar interfaces. The spherical bubble of radius 50 μm, initially kept at the saturation temperature, is surrounded with the superheated liquid, and grows due to the heat input from the bulk medium until its radius is doubled. The temperature field outside the bubble region is initialized using the analytical solution at $t = 0.016$ ms, which corresponds to the aforementioned initial radius. The simulations were carried out for three different levels of superheat, that is, three different Jakob numbers and the agreement with the analytical solution has been reported. The model validation is carried out using the rising of a vapor bubble in a superheated liquid case. The final simulation of the nucleate boiling on a horizontal surface has proven the reliability of the method in resolving complex boiling phenomena. This study also addresses mass conservation in the phase-change simulations, using two distinct measures that are proposed to this end.

The study on film boiling in the vicinity of a sphere immersed in saturated water at atmospheric pressure, considering also the case with the involved radiation heat transfer, is carried out by Arevalo *et al*. [16]. The film boiling is studied for various solid surface temperatures, and the obtained heat flux values were compared with the results obtained using different correlations. Furthermore, an estimation of radiation coupling factors is done using numerical simulation. The Volume-of-fluid (VOF) method implemented in the computational software Fluent has been used for modeling the multiphase flow, while the modeling of the mass transfer has been done using the approach proposed in Nichita [14].

A theoretical foundation of the analytical solution to Stefan problem has been extensively reviewed by Perez-Raya and Kandlikar [17]. Furthermore, the authors presented a detailed description of the implementation of their VOF-based method for solving the Stefan problem in the ANSYS Fluent CFD package.

A comprehensive review of the computational models for the simulation of boiling and condensation phenomena is presented in Kharangate and Mudawar [18]. Among the reviewed models three distinct mass transfer models were outlined, namely: the energy jump, Schrage, and Lee model, and their characteristics are summarized in a tabular form. The reinterpretation of the table is given in Table 1. The energy jump model, already introduced via Eqs. (7), (10), and (11), stem from the heat balance at the phase interface and, in the general form reads:

$$\dot{q}_{\mathrm{m}} = \frac{\left(\lambda_{\mathrm{l}} \nabla T_{\mathrm{l}} - \lambda_{\mathrm{v}} \nabla T_{\mathrm{v}}\right)\vec{n}}{r_0}, \tag{14}$$

where $\vec{n}$ is the interface normal. The simpler form of this model is:

$$\dot{m} = \frac{\lambda_{\mathrm{eff}} \left(\nabla T \nabla \alpha_{\mathrm{v}}\right)}{r_0}, \tag{15}$$

where λ_{eff} is the effective thermal conductivity; however, the consideration of effective thermal conductivity is not completely physical since it considers the thermal conductivity of the saturated phase that doesn't participate in interphase heat transfer, but it is easier to implement such a model since it doesn't identify the exact interface location. Anyway, the energy jump based models require an identifiable interface due to $\nabla\alpha$ term to compute the mass transfer; thus being unsuitable for computations of bulk phase change processes wherein, for example, the subcooled liquid enters the domain and experiences the phase change after being subjected to high wall heat flux. The Schrage model, on the other hand, is derived from the kinetic theory of gases and is based on a premise that there exists a difference between saturation pressures of vapor and liquid phase at the interface and correspondingly the difference between the vapor and liquid saturation temperature. The model, in general form, reads:

$$\dot{q}_{\mathrm{m}} = \frac{2}{2 - \gamma_{\mathrm{c}}} \sqrt{\frac{M}{2\pi R_{\mathrm{m}}}} \left[\gamma_{\mathrm{c}} \frac{p_{\mathrm{v}}'}{\sqrt{T_{\mathrm{v}}'}} - \gamma_{\mathrm{e}} \frac{p_{\mathrm{l}}'}{\sqrt{T_{\mathrm{l}}'}} \right], \tag{16}$$

where γ_{c} and γ_{e} are kinetic transport related accommodation coefficients that refer to condensation and evaporation, respectively; M is the molar mass; R_{m} is the universal gas constant, 8314 J/(kmol K); p_{v}' and p_{l}' are the saturation pressures of vapor and liquid phase, respectively, while T_{v}' and T_{l}' are their respective saturation temperatures. The assumption of the equality of the condensation and evaporation accommodation coefficients, that is, $\gamma_{\mathrm{c}} = \gamma_{\mathrm{e}} = \gamma$, yields the following expression for computation of the mass transfer across the interface:

$$\dot{q}_{\mathrm{m}} = \frac{2\gamma}{2 - \gamma} \sqrt{\frac{M}{2\pi R_{\mathrm{m}}}} \left[\frac{p_{\mathrm{v}}'}{\sqrt{T_{\mathrm{v}}'}} - \frac{p_{\mathrm{l}}'}{\sqrt{T_{\mathrm{l}}'}} \right], \tag{17}$$

with the accommodation coefficient in the range $0 < \gamma \leq 1$. In a simplified form, the Schrage model is reduced to the Tanasawa model and reads:

$$\dot{q}_{\mathrm{m}} = \frac{2\gamma}{2-\gamma}\sqrt{\frac{M}{2\pi R_{\mathrm{m}}}}\left[\frac{\rho_{\mathrm{v}} r_0 (T - T')}{(T')^{\frac{3}{2}}}\right], \tag{18}$$

which, as noted by the authors, provides a basis for the Lee model. The mass transfer per unit volume in both, the Schrage and Tanasawa models, is calculated as:

$$\dot{m} = \dot{q}_{\mathrm{m}} |\nabla \alpha_{\mathrm{v}}|, \tag{19}$$

thus ensuring that the dominant mass transfer rate appears at the phase interface, but also requires the preexisting interface to induce the mass transfer. The value of the accommodation coefficient, γ, is case dependent and different researchers have reported the different values as relevant for their specific purpose; among them, relevant for this work, is the study by Magnini *et al*. [19], who reported $\gamma = 1$ in the case of film boiling. Furthermore, Kartuzova and Kassemi [20] found the same value as appropriate in the case of turbulent flow with phase change in a cryogenic application. The last of three popular methods is the Lee model which incorporates empirical constant r_{i} and is defined as follows:

$$\dot{m}_{\mathrm{v}} = -\dot{m}_{\mathrm{l}} = r_{\mathrm{i}} \rho_{\mathrm{v}} \alpha_{\mathrm{v}} \frac{T - T'}{T'}, \tag{20}$$

in the case with $T < T'$, that is, the condensation. The evaporation mass transfer, $T > T'$, is computed as:

$$\dot{m}_{\mathrm{v}} = -\dot{m}_{\mathrm{l}} = r_{\mathrm{i}} \rho_{\mathrm{l}} \alpha_{\mathrm{l}} \frac{T - T'}{T'}. \tag{21}$$

The following description of the models is carried out with an assumption of a multiphase flow system composed of a saturated and unsaturated phase. Thus, from the structure of Eqs. (20) and (21) it is obvious that the mass transfer occurs in the saturated phase and at the interface.

However, the determination of constant r_i requires fine-tuning, since it is very case-dependent, e. g. time-step size and mesh resolution. The reported values of r_i range from 0,1 to 10^7 s^{-1}.

Table 1. A brief overview of popular mass transfer models according to Kharangate and Mudawar [18]

	Energy jump	Schrage	Lee
Governing equation	$\dot{q}_m = \frac{(k_v \nabla T_v - k_l \nabla T_l)\vec{n}}{r_0}$	$\dot{q}_m = \frac{2}{2-\gamma_c}\sqrt{\frac{M}{2\pi R_m}} \cdot \left[\gamma_c \frac{p_v'}{\sqrt{T_v'}} - \gamma_e \frac{p_l'}{\sqrt{T_l'}}\right]$	Condensation: $\dot{m}_v = -\dot{m}_l = r_i \rho_v \alpha_v \frac{T - T'}{T'}$ Evaporation: $\dot{m}_v = -\dot{m}_l = r_i \rho_l \alpha_l \frac{T - T'}{T'}$.
Simplified form	$\dot{m} = \frac{\lambda_{eff}(\nabla T \nabla \alpha_v)}{r_0}$,	$\dot{q}_m = \frac{2\gamma}{2-\gamma}\sqrt{\frac{M}{2\pi R_m}} \cdot \left[\frac{\rho_v r (T - T')}{(T')^{\frac{3}{2}}}\right]$	None
Kinetic energy contribution	No	Yes	No
Physical basis	Energy balance at the inteface	Kinetic theory of gases	Discrepancy from saturation temperature induces the mass transfer
Empirical data needed	No	Yes	Yes
Bulk phase change available	No	No	Yes
Favourable boiling modes	Film boiling Flow boiling Nucleate pool boiling	Film boiling Flow boiling Nucleate pool boiling	Flow boiling

Stefan problem is used in the verification of the VOF-based phase change model proposed by Pan *et al*. [8]. The model is based on fixing the interface temperature to saturation temperature and was verified for three different working fluids: HFE7100, R113, and water.

Three different mass transfer models, namely Sun, Lee, and Rattner models, were applied in the case of the Stefan problem in the work by Kim *et al*. [9]. The influence of a comprehensive set of parameters on transient film thickness is examined for each model.

A study of the pool boiling process in which the film boiling regime is achieved as a consequence of exceeding the critical heat flux (CHF) limit is carried out in Sato and Ničeno [21]. The authors use the aforementioned approach [12] for handling multiphase flow with a phase change in an Eulerian framework, that is, using a single set of governing equations with a color function as an interface indicator, but adapting it to turbulent flow modeling using a large eddy simulation (LES) approach. Thus, the heat flux balance at the interface is now supplemented with turbulent thermal conductivity and the heat fluxes at the interface now read:

$$q_l=(\lambda_{liq}+\lambda_t)(\nabla T_l)\cdot\vec{n}\,;\, q_v=-(\lambda_{vap}+\lambda_t)(\nabla T_v)\cdot\vec{n} \quad , \tag{22}$$

The Smagorinsky coefficient used in the simulation is set to 0.17. The flow behavior is analyzed for different heat flow rates imposed on the heat transfer surface. The authors note that transition boiling can be modeled if the imposed heat flow rate is lowered. The study is designated as a conjugate heat transfer case, consisting of fluid and solid domains; the solid being included using the Immersed Boundary (IB) method. The computational domain is reduced, in comparison to the validation experiment from Gaertner [22], to decrease the necessary computing power needed for the simulation, maintaining thereby the necessary unstable film boiling wavelength by the selection of the appropriate reduced diameter of the cylindrical heater, that is, the diameter of the heater is larger than the critical wavelength of the vapor film. The performed simulations were run for eight different heat fluxes imposed at the bottom of the solid domain, which is located beneath the fluid domain. Also, the bubble nucleation sites were determined using the random number generator. The selected heat flux values correspond to nucleate and film pool boiling modes. The model utilizes one empirical parameter, C_{slope}, that needs to be calibrated based on the experimental data. Different values of C_{slope} result in different vapor geometry, that is, as demonstrated in the paper, the slimmer vapor bubbles are produced using the higher value of C_{slope}. This value has to be provided to establish realistic behavior in the simulation. The method also involves a micro-layer model, a thin liquid layer beneath the bubble. Thus, the total heat flux arriving from the bottom of the solid domain is partitioned on a solid-fluid interface into three components: bulk liquid, micro-layer, and continuous vapor. Among the presented results, the contours of color function (a phase indicator) and solid and fluid temperatures, clearly demonstrate the method's full capability in successfully resolving specific boiling regimes.

An OCASIMAT approach that requires only one cell in solution to mass transfer when a single-fluid Volume-of-fluid (VOF) model is used is presented in Perez-Raya and Kandlikar [13]. This approach uses one cell in the estimation of the temperature gradient at the interface and thus ensures sharp distribution of the mass transfer at the interface. To this end, the method uses three probes (Fig. 4):

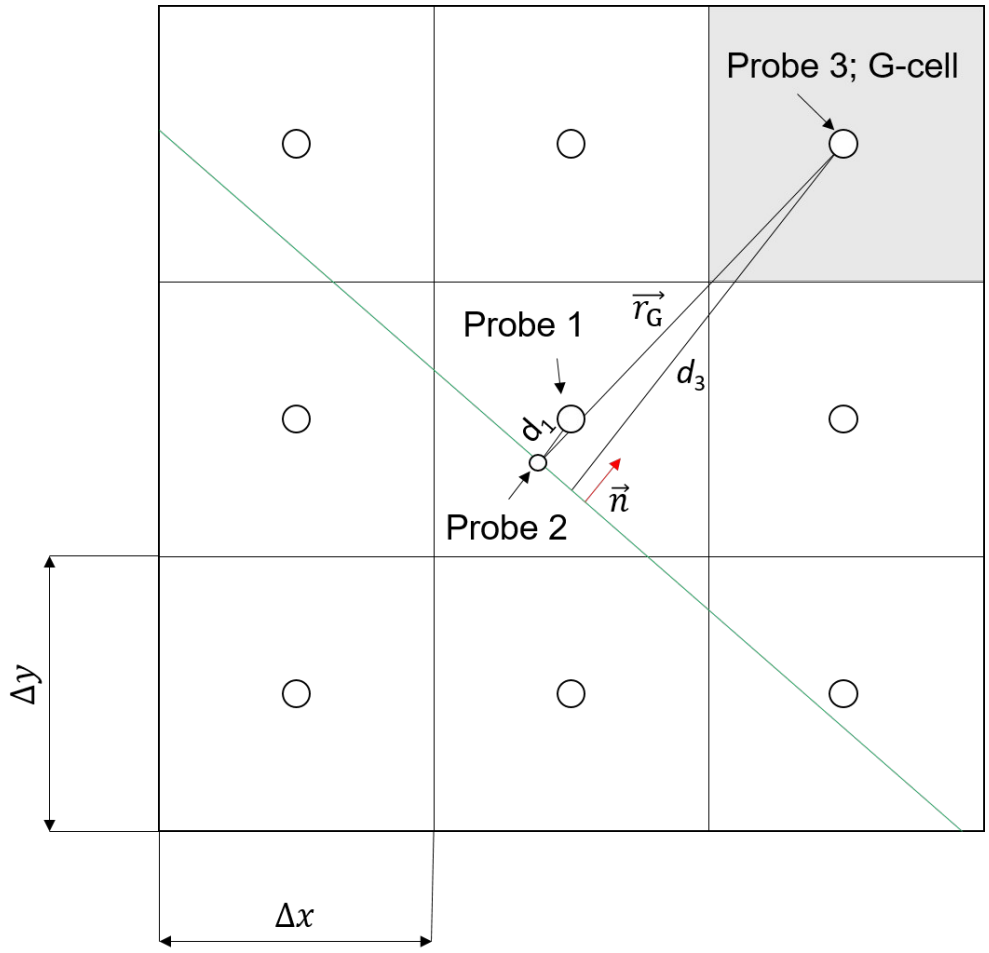


Fig. 4. Graphical representation of the OCASIMAT model.

1. The first probe coincides with the cell center of the mixture cell, i.e. the cell containing the interface. The shortest length from this point to the interface is denoted as d_1 and leads to "point a".
2. The "point a" serves as the second probe, and is used for estimation of the nearest liquid cell in the normal direction, the distance d_2 that is being evaluated as $d_2 > \sqrt{\Delta x^2 + \Delta y^2}$, where Δx and Δy are the horizontal and vertical mixture cell lengths, respectively.

3. The closest cell completely filled with liquid, which has been found using the probe 2, is marked as G-cell, that is, the gradient cell, since the distance of its center from the interface, named d_3 by the authors, is relevant for computation of the temperature gradient. The center of G-cell is referred to as the third probe.

The aforementioned distance from the nearest liquid cell, the G-cell, to the interface is obtained by calculation of the position vector $\vec{r}_{\mathrm{G}}$ from probe 2 to the center of the G-cell (probe 3) and its projection to the interface normal:

$$d_3 = \vec{r}_{\mathrm{G}} \cdot \vec{n}. \tag{23}$$

The mass flow rate is thus:

$$\dot{q}_{\mathrm{m}} = \frac{\lambda}{r_0} \cdot \frac{T_{\mathrm{G}} - T'}{d_3}, \tag{24}$$

while the temperature of the mixture cell is given by:

$$T_{\mathrm{M}} = T' + d_1 \frac{T_{\mathrm{G}} - T'}{d_3}, \tag{25}$$

that stems from the equality of the temperature gradients in points “a” and “b”. The method is implemented in a commercial CFD code ANSYS Fluent, and is validated against a one-dimensional Stefan problem and a two-dimensional bubble growth case; both using structural meshes.

The simulation of the dispersed flow film boiling (DFFB) regime using the level-set method (LSM) in conjunction with Direct Numerical Simulation (DNS) of turbulence is presented in Saini and Bolotnov [23]. The study is carried out using “in-house” computational software PHASTA, based on stabilized finite-element method, with the conditions at the inlet obtained from single-phase computation. Among the presented results, the normalized profiles of turbulent kinetic energy are shown. Although the fluid flow is assumed as adiabatic, a reference is made to a work wherein is pointed out how the occurrence of the smaller droplets in the flow leads to an increase in heat transfer coefficient, due to an increased heat transfer surface.

In addition to the aforementioned computational studies, one has to outline the fundamental experimental film boiling study during the quenching of different silver specimens in either saturated or subcooled water under atmospheric pressure examined in Momoki *et al.* [1]. The temperature is measured using sheathed K-type thermocouple placed centrally in the specimen, and the temperature histories were tracked with the acquisition time of 0.25 s. The Biot number reported in the paper is lower than 0.1, and therefore the uniform temperature distribution inside the material may be assumed. The temperature versus time dependency is highlighted for the case of the cylinder with the dimensions $D = L = 45$ mm, immersed in saturated and, to various degrees, subcooled water. It was found that lower degrees of subcooling lead to longer periods of film boiling regime, with the maximum duration in the case of saturated water.

1.4.2 Closure on fundamental studies

The outlined fundamental studies have revealed the basic phenomena associated with the film boiling processes; such as the unsteady interface evolution and were primarily focused on computational studies, except for the last two papers, which deal with experimental investigation of fundamental boiling phenomena associated with the stable film boiling. The presented computational studies belong to the so-called direct numerical simulation (DNS) of interface tracking and, as discussed above, are mostly directed to one-fluid methods such as Volume-of-fluid (VOF) that is mass conservative, but face difficulties with handling the interface topology, or the Level-set method (LSM) that handles easier the interface deformations, whilst fails on mass conservation. In both cases, a sharp mass transfer in the vicinity of the interface may be realized. In doing so, the mass transfer model needs to be supplemented with the gradient of the volume fraction field and the proper reconstruction of the temperature gradient at the interface; both in the case of the energy balance mass model. However, in these methods, detailed, i. e., sufficiently fine meshes and time steps are needed to reproduce properly the interface topology in a computer simulation; hence being expensive for further use in industrial-scale problems. This can be remedied by the application of more common for the application in industry, the two-fluid based methods, that are accompanied to the aforementioned methods in the next subsection.

1.4.3 Applied studies

To the author's knowledge, the first paper dealing with the numerical simulation of conjugate heat transfer in a quenching process is the one by Krause et al. [24]. The proposed approach utilizes Lee's mass transfer model with temperature-dependent constant β. The model is based on mixture model (MM) formulation that alleviates modeling of interphase transport since only one set of governing equations is being solved for both phases, that is, the phase mixture.

Shortly thereafter, an approach based on a two-fluid model (TFM) for numerical simulation of water quenching is presented in Srinivasan *et al.* [25]. The proposed mass transfer model is defined as:

$$\dot{m}_{\mathrm{lv}} = \frac{C_{\mathrm{b}} C_{\mathrm{m}} h \Delta T_{\mathrm{w}}}{r_0} A_{\mathrm{i}}, \tag{26}$$

where C_{b} and C_{m} are, respectively, boiling and interfacial area density correction factors, h is the heat transfer coefficient, ΔT_{w} is the wall superheat, r_0 is the specific heat of vaporization and A_{i} is the interfacial area. The interfacial area density is computed using the standard dispersed flow relation:

$$A_{\mathrm{i}} = \frac{6 \alpha_v}{d_{\mathrm{v}}}, \tag{27}$$

where α_{v} is the volume fraction of the vapor phase and d_{v} is the vapor bubble diameter. The heat transfer coefficient, h, in Eq. (26) is boiling regime dependent. The film and transition boiling regimes are taken into consideration with the proposed model, with constant Leidenfrost temperature as a switch criterion between the two. In the case of film boiling the computation of h is based on Bromley's correlation for heat transfer coefficient in a steady-state film boiling at a horizontal tube in a saturated liquid; derived analogously to Nusselt number correlation for film condensation. Although the TFM is used, the authors formulate the energy equation for a phase mixture, thus alleviating the necessity for modeling complex energy transport at the phase interfaces. Furthermore, the energy transfer at the fluid-solid interface is accomplished using AVL-code-coupling-interface (ACCI) with non-conformal cell arrangement between the two

domains. The proposed model is applied in the simulation of engine cylinder head quenching in Srinivasan *et al*. [26]. The discrepancy of the temperature field in comparison to experimental data may be addressed by the incorporated assumption of the constant Leidenfrost temperature in the model.

The aforementioned approaches, MM and TFM, possess a loss of information about the phase interface, due to the averaging procedure that underlies these approaches. Furthermore, these approaches are used in conjunction with the finite-volume method (FVM) for equation discretization. However, the usage of the instantaneous Level-set method (LSM) in conjunction with stabilized finite-element method (FEM) in the numerical modeling of the quenching process is proposed in Kosseifi [10]. This model is validated using a bubble growth case, and the transport of the vapor phase is established via convection reconstruction velocity; incorporating thereby the volume fraction gradient in the computation of surface normal. The goal of the validation against the two- and three-dimensional growing sphere problem was to establish a linear dependency, both in two- and three-dimensions, of sphere radius as a function of time. The melting case is defined with the initial sphere shape and the prescribed boundary conditions. The sphere is considered to be at a higher temperature than the ambient medium and the solution of the energy equation yielded the temperature field; the necessary information for the computation of growth velocity:

$$v_g = C(T - T')\mathbf{n}, \tag{28}$$

where C is the model constant, T' is the phase change temperature, and $\mathbf{n}$ is the interface normal, computed using the level-set function. After the growth velocity, that is, the velocity of the free surface between the phases is calculated, a re-initialization of the level-set function, i. e. the interface, is carried out. Further studies in this regard encompass isothermal bubble growth and merge with the prescribed growth, i. e. the interface, and velocity. Furthermore, a bubble rise is modeled with the incorporated surface tension model proposed in Brackbill *et al*. [27] preceded by the simulation of the bubble growth due to heat input from the slightly heated surrounding liquid in an enclosed domain. In the case of the rising bubble, only continuity and momentum equations were solved, supplemented with an anisotropic mesh adaption remeshing technique, to capture the changeable interface topology. The proposed model uses the variational multi-scale approach for efficient handling of mass and momentum equations in multiphase flows with high density and viscosity ratios across the interfaces. The specific heat of

vaporization in the model is considered via an energy equation. Furthermore, the boiling phenomenon that occurs during quenching is studied both, experimentally and computationally. In the presented experimental study, firstly the vapor distribution in the cases with constant bath temperature and different initial solid temperatures is shown; followed by snapshots of the vapor formations in the cases with constant initial solid temperature, but different bath temperatures. The performed numerical simulations have demonstrated the method's capability in resolving the vapor film and the obtained solid temperatures were compared with the experimental data. The applied numerical algorithm is an extension of the aforementioned one used in the case of bubble growth, that is, after the growth velocity is computed using Eq. (28) upon the calculated temperature distribution; the momentum equation supplemented with surface tension as a source term is solved and the velocity field is obtained. The sum of the growth velocity and the velocity computed as a dependent variable result in the transport velocity that precedes the solution of the convection reinitialization equation used to advect the interface.

An extension of the model proposed in Srinivasan *et al.* [25] in terms of the inclusion of additional momentum transfer closures, namely lift and wall lubrication forces, and the variable Leidenfrost temperature, together with another fluid-solid energy transfer coupling interface, termed MMAT, is shown in Kopun *et al.* [28]. The model is applied in the computation of quenching of a steep aluminum plate and an engine cylinder head. The structure of the applied mass transfer model is the same as in the base model in [25], but the variable Leidenfrost temperature is used as a criterion for determination of the boiling mode that is present in the flow domain, that is, as a switch criterion between the different correlations for calculation of the interphase heat transfer coefficient which, as shown in Eq. (26), directly influences the computed mass transfer. The authors emphasized the influence of the variable Leidenfrost temperature on the solution accuracy.

A numerical model for the simulation of spray quenching using the Eulerian two-fluid model is developed by Stark and Fritsching [29]. This model resolves film and nucleate boiling regimes that occur in the process as well as the convection heat transfer, but also the condensation processes that are present in the flow. To accomplish this, appropriate source and sink terms are included in conservation equations for mass, momentum, and energy transfer. To determine which of the aforementioned phase change phenomena takes place, in each computational cell two criteria are examined: the liquid temperature and the volumetric heat flow rate. Firstly, the temperature of the liquid in the cell is compared to the saturation temperature for relevant

absolute pressure in the system (hereinafter called saturation temperature). If the liquid temperature is higher, a limiting volumetric heat flow rate is computed using the following expression:

$$\Phi_{\text{limit}} = -\alpha_{\text{l}}\rho_{\text{l}}c_{\text{l}}\frac{T_{\text{l}}-T'}{\Delta t_{\text{s}}}, \tag{29}$$

where α_{l} is the volumetric phase fraction of the liquid phase in the cell, ρ_{l} is the density of the liquid phase, c_{l} is specific heat capacity (at constant pressure) of the liquid, T_{l} is the temperature of the liquid in the cell, T' is the saturation temperature and Δt_{s} is the applied time step in the calculation. Also, the volumetric heat flow rate is computed and reads:

$$\Phi_{\text{cell}} = -\alpha_{\text{l}}\rho_{\text{l}}c_{\text{l}}\frac{\Delta T_0}{\Delta t_{\text{s}}}, \tag{30}$$

where ΔT_0 is the bubble initiation temperature difference, calculated from the mechanical and thermal balance of a single vapor bubble; other physical quantities are as described in Eq. (29). Now, the second criterion is invoked and reads:

$$\Phi_{\text{cell}} > \Phi_{\text{limit}}. \tag{31}$$

If the statement in Eq. (31) is true, the boiling process takes place in the cell. Otherwise, the condensation occurs. This condensation is referred as “Condensation I”, and is consequence of the volumetric heat flow rate in the cell. Furthermore, the model considers the case when vapor temperature is lower than saturation temperature, that is, $T_{\text{v}} < T'$. Then, the condensation referred as “Condensation II” takes place. This approach is implemented within the framework of ANSYS Fluent computational software, and has been applied in numerical simulation of jet impingement cooling of a flat plate; a conjugate heat transfer problem used to, among other results, obtain the distributions of heat transfer coefficients and surface temperatures.

The different studies related to jet impingement cooling of a heated surface were conducted by Subhash [30]. The author used AVL Fire computational software and have modeled the jet impingment cooling using VOF and multi-fluid models; VOF for flows without phase change, aimed on studying hydrodynamic characteristics of the flow, the influence of turbulence model

on resulting wall heat transfer and the behavior of multiple jet impingement, whilst multi-fluid model was utilized for computation of boiling flows, that is, the quenching process. The importance of adequate modeling of turbulence in accurate estimation of wall heat transfer is emphasized, in particular the important role of turbulent kinetic energy. The quenching process is modeled using the model of Srinivasan *et al*. [25]. A model for estimation of surface temperatures and wall heat fluxes in the case of film boiling during circular or planar jet impingement is also proposed in the work.

A 3D industrial scale quenching model is proposed in Bahbah [31]. The author states how variational multi-scale approach, used in the study, corresponds to large-eddy simulation (LES) approach in resolving the flow fields during computations. The boiling flow during quenching of complex parts has been shown in the work.

1.4.4 Applied studies closure

The presented applied studies focus, in contrary to the fundamental simulation cases, on more macroscopic effects, and thus do not mandatory involve the direct methods. Hence, a wide variety of methods is applicable in order to tackle the problem. In addition to the direct methods, two more macroscopic methods are introduced, TFM and MM; the former being the most elaborate and capable of handling all types of multiphase flow, whilst the latter can be derived from TFM and thus represent its simplified form, wherein it is not mandatory to prescribe the complex interfacial transfer, since the equations are not written on a per phase basis. This approach would not considered further in the text, yet the macroscopic approach will be denoted as the TFM. This approach may lead to accurate results without prescription of interface, but, on the other hand, the problem with such approaches, but also and direct methods when we speak in terms of large scale, industrial problem cases, is in necessity of adoption of correction factors in terms of model constants in order to obtain to correct solution; with an exception of the last discussed case, wherein a detailed framework is adopted. Hence, in order to avoid relying on the empirical data, but still preserving all the features of the TFM, a large interface handling within the context of TFM becomes interesting to observe.

1.4.5 Conclusion on literature review

The fundamental studies have revealed the main issues regarding the mass transfer modeling; and demonstrated the main mass transfer models; among them, the energy balance model has been identified as the most prominent, since it does not rely on empirical constants and stems from pure energy balance at the interface between the fluids. Hence, the main issues in successful resolving of the film boiling during immersion quenching using this model will be:

1. the reconstruction of the temperature gradient at the vapor-liquid interface in the mass transfer model;
2. the adequate turbulence modeling.

The necessary prerequisite to this end (point 1) is the existence of the identifiable interface between the phases, such that the mass transfer may take place at the interface. This is due to gradient of volume fraction incorporated in the computation of interfacial area density. Furthermore, an additional remark has to be pointed out on turbulence modeling (point 2); since the turbulent heat flux is defined by Eq. (2), and has to be computed accurately in order to estimate the transient temperature distribution in a solid object correctly. Hence, a more elaborate turbulence modeling has to be carried out, since there is a complex interaction between the vapor and liquid phase in the process. However, these approaches are mostly assigned to one-fluid formulations, such as VOF or LSM, wherein a single set of governing equations is solved for both phases, and hence the individual phase modeling instead of mixture, becomes difficult to handle.

The applied studies, on the other hand, have shown how the application of TFM may lead to successful numerical simulations using coarse meshes, but the source terms used for modeling the interfacial transfer, that appear in the governing equations due to the averaging process used in derivation of the governing equations and are defined on a per phase basis, are needed to be supplemented with the adequate closures. Furthermore, since the equations are defined on a per phase basis the individual modeling of each phase is foreseeable, as well as the application of higher time steps in the simulations. However, the problem is that in the averaging process the information about the interface is lost, and implementation of the energy balance mass transfer model that involves the interface and doesn't require the empirical factors is made difficult.

To sum up, an ideal method would comprise the interface existence from single-fluid formulations, such as VOF or LSM, and the application of low-resolution meshes and high time steps together with individual phase modeling access from TFM. To accomplish this, a two-fluid VOF method comes in handy.

This kind of approaches are not strange in the field of multiphase CFD (M-CFD) modeling. Starting from work of Černe *et al*. [32] on, there were numerous attempts to combine the two approaches. A concise review of the work that has been carried out in the field two-fluid modeling with the identifiable interfaces can be found in Mer *et al*. [33].

Among the modeling approaches presented in [33], further exploration in the paper is made on the following models, namely: Large Interface Model (LIM), Generalized Large Interface Model (GLIM) and Large Bubble Model (LBM). The description of LIM is given in Coste [34]. LIM identifies the large interface, but does not reconstruct it. In order to determine the distance from interface to the adjacent cell, the method utilizes a three-cell stencil concept: one cell contains the interface, while other two are occupied by single representatives of the involved phases. The substantial difference in inteface handling between the LIM and the general interface tracking method is given in PhD thesis by Dènefle [35]; and is consisted in localization of the interface and extrapolation of the physical quantities near the interface: in LIM it is carried out using a three-cell stencil, with two cells containing a single phase, and one that belongs to the interface; whilst in ITM a color function is used to denote the interface, and the extrapolation is achieved via the gradient of the variable in question.

The general idea behind LBM can be found in Dènefle et al. [21]. LBM is three- or four-field approach in the framework of two-fluid model, that considers two continuous and one or two dispersed phases. The distinction between the continuous phases, that are simulated, and dispersed phases, that are modeled, is made with a spatial cutting length, while the mass exchange between the continuous and dispersed field of the same phase is established via the mass transfer terms. However, to the authors' knowledge, there appears not to exist evaluation of the two-fluid VOF for Stefan problem in the literature.

Within this work, the two-fluid VOF model available in CFD package Ansys® Fluent has been used in order to solve the quenching process by use of numerical simulation. The advantage of

the two-fluid VOF over the single-fluid VOF is in avoidance of averaging of the material properties in the energy equation, which reduces the accuracy in the heat-flux calculation [13].

The novelty of the present work is the application of two-fluid VOF method to quenching problem and the validation of the model to not only quadrilateral meshes but also triangular meshes. The originality of our model is the usage of local mesh size via the heat transfer coefficient, that, therefore, has a fictitious function, which is further explained in the section of the numerical model.

1.4.6 A brief disclaimer for Croatian readers

In our tradition inherited form Dresden School of Thermodynamics, is to denote the heat transfer coefficient with lowercase Greek letter "alpha", α. Within the context of the present research, the lowercase letter "*h*" will be kept to denote the heat transfer coefficient, as is usual in standard heat transfer literature written in English. The eventual collision with the specific enthalpy in the context of application of formulae that encompass both[1], that is, the average heat transfer coefficient in a film condensation on a vertical planar surface, is not foreseen in the context of the present study.

1.5 Objectives and hypothesis of the thesis

The goal of this PhD thesis is to develop a numerical model for the simulation of immersion quenching that is capable to predict the temperature field within material on the basis of given initial conditions: material and quenchant temperatures. This implies efficient numerical modeling of film boiling, which determines the success of the complete computation.

From there, the research hypothesis is derived and reads: "*Using Eulerian two-fluid model the accurate estimate of the temperature field at surface and inside the solid body in film boiling regime during immersion quenching could be achieved*."

1 The author thank to Professor Galović for pointing this out.

This hypothesis may be explained as follows. Since the film boiling is, due to its sharp interface nature and, therefore, as has also been shown in the previous subsections, a more convenient is to be simulated with single-fluid methods like VOF and LSM, in this study we state how this standard single-fluid simulation, cannot only be resolved with that approach; it can also be successfully solved using two-fluid simulation method.

1.6 Expected scientific contribution

Within the framework of this work, special attention has been made on estimation of the heat flow rates at the phase interfaces in order to achieve the main goal of this thesis. To accomplish this, as shown in the former subsections, a set of closures is mandatory to be defined; hence, we arrive at the first scientific contribution of this thesis that reads: "*the formulation of baseline closure model that is necessary in order to conduct to conduct the film boiling simulation with accompanying heat conduction in a solid phase*".

On the other hand, the second main scientific contribution is straightforward, and can be formulated as follows: "*the conduction of numerical simulation of film boiling phenomenon during metal material quenching using Eulerian two-fluid formalism*".

As shown in literature review, the numerical simulations literature on quenching process is scarce, and there is ample room for novel models in this field. Due to complex physics involved in the process, it is difficult to propose the model that would rely mostly on basic principles. Hence, with the approach presented in this thesis, a novel modeling approach in the area of metal quenching process is suggested that is based on application of basic principles, at lest to a great extend in the mass transfer modeling, in order to overcome this gap.

1.7 Thesis outline

Chapter 2 brings us a novel mass transfer model used in computation of, firstly, the Stefan problem in the scope of method verification and, afterwards, in the solution to conjugate heat transfer (CHT) during cooling of a cylinder specimen made of silver with presence of the film boiling mode of the convective heat transfer. By completion of Ch. 2 one may proceed to the final goal of the thesis, i. e., the numerical solution of CHT and a phase change process. In

Chapter 3, the numerical setup for final simulation has been presented. Ch. 4 brings out the computational results, whilst the important conclusions regarding whole work are summarized within Chapter 5 at the end of the thesis.

2 NUMERICAL METHOD

The cooling of a heated solid object in a vaporizable liquid medium possesses significant challenges from a viewpoint of a numerical simulation, as can be deduced from the previous chapter. In the preceding chapter the main methods used in the phase change computations were also outlined, and, their advantages, but also the difficulties related to their application in the framework of the large-scale computations. Two are main modeling approaches to this end: the more macroscopic one, i. e., the two-fluid related modeling; and the direct numerical simulation (DNS) of interface motion, such as LSM or VOF. The former approach has been primarily associated with the large-scale computations and comes with possibility to with larger time steps and coarser grids; wherein empirical closures are used in order to establish a complete mathematical model. On the other hand, the eventual fine tuning and, therefore, loss of generality, are limiting factors in adoption of such a modeling approach. In the latter approach – DNS – the interface is directly tracked, but sufficiently fine grid cell size and a time step are necessary to resolve all relevant time and length scales.

Therefore, in this chapter, a novel method for estimation of the mass transfer across the interface in a thermally driven phase change process is presented. The method is implemented within the two-fluid VOF formulation (available in the commercial CFD software ANSYS Fluent). It consolidates the benefits of the two multi-scale multiphase modeling approaches: the low resolution meshes and large time steps from the two-fluid formulation; whilst preserving the sharp interface treatment using geometrical reconstruction algorithm, that is, a property of the pure VOF method, used generally for DNS of interface motion.

In this chapter, furthermore, the governing and constitutive relations are provided. After this, a brief description of the Stefan problem is presented, together with the results obtained in numerical solution to the aforementioned one-dimensional planar interface evaporation case as a part of verification section. The success in solving laminar two-phase flow with a phase change, i. e., the Stefan problem, has been further investigated in the sense of conjugate heat transfer modeling of film boiling that is to appear during cooling of a silver specimen in a saturated liquid. Special care is, thereby, taken to the turbulence modeling in the carrier phase, i. e., the liquid turbulence.

More information on how this has been carried out within the scope of the present research, and which closures were necessary to define the computational model, are given in the next following subsections.

2.1 Mathematical model

Within the framework of the two-fluid model adopted here for solution of laminar two-phase flow with phase change, two separate sets of conservation equations are solved in each computational cell; one for each phase present in the domain. The theoretical foundations underlying the two-fluid model are given in Drew and Passmann, Refs. [36] and [37], while the model equations available in Fluent and applied in this study are taken from [38]. The communication between the two phases is established via source terms in the equations, referred to as phase interaction terms. In addition, a single pressure field is shared between the phases. The temperature in the liquid phase is assumed to be constant at the saturation temperature within this section.

2.1.1 Conservation equations

The evolution of planar liquid-vapor interface due to evaporation, studied here, is described with three laws of classical physics, namely: the conservations of mass, momentum and energy:

$$\frac{\partial}{\partial t}(\alpha_q \rho_q) + \nabla \cdot (\alpha_q \rho_q \vec{v}_q) = \dot{m}_{pq} \tag{32}$$

$$\frac{\partial}{\partial t}(\alpha_q \rho_q \vec{v}_q) + \nabla \cdot (\alpha_q \rho_q \vec{v}_q \vec{v}_q) = -\alpha_q \nabla p + \nabla \cdot \bar{\bar{\tau}}_q + \vec{R}_{pq} + \dot{m}_{pq} \vec{v}_{pq} \tag{33}$$

$$\frac{\partial}{\partial t}(\alpha_q \rho_q h_q) + \nabla \cdot (\alpha_q \rho_q \vec{u}_q h_q) = \alpha_q \frac{d p_q}{dt} + \bar{\bar{\tau}}_q : \nabla \vec{u}_q + \Phi_{pq} + \dot{m}_{pq} h_{pq} \tag{34}$$

where subscripts *q* and *pq* refer to particular phase and the phase pair involved in certain interfacial transfer process, respectively. Appropriate closure models are required for the interphase transfer terms that appear at the right-hand side in these equations, those are, interfacial mass transfer, $\dot{m}_{pq}$, the momentum transfer, $\vec{R}_{pq}$, and the heat transfer, Φ_{pq}, terms.

These terms stem from averaging process used in derivation of the set of conservation equations and more details regarding the closures applied therein is given in the forthcoming section.

2.1.2 Closure models

2.1.2.1 Interfacial area

The interphase transfer terms in the presented set of conservation equations for a continuum composed of interpenetrating phases have to be supplemented with suitable correlations. A common issue, however, in all the terms is related to modeling of the interfacial area. When free surface flow modeling is considered, the interfacial area per unit volume is computed as:

$$A_i = |\nabla \alpha_q| \tag{35}$$

This idea is also inherited for free surface modeling within Algebraic Interfacial Area Density (AIAD) modeling approach for handling different interface scales inside two-fluid model, presented by Höhne and Vallée [39]. Since the application of Eq. (35) yields the application of closure models only within the interface zone, the closures used in this study can be referred as "locally imposed closures"; as shown also in Kharangate *et al.* [40].

2.1.2.2 Interphase momentum transfer

In general, the interphase momentum transfer consists of the drag force, lift force, wall lubrication force, turbulent dispersion force and virtual mass force. Since in the solution of Stefan problem there is a distinction between the phases with a free surface, the incorporation of drag force is necessary according to the study of stratified two-fluid modeling by Štrubelj *et al.* [41]. The role of the drag force, as noted by the authors, is to ensure equal velocities of the phases within the interface region. The physical basis of the correlation applied for computation of the drag force coefficient is not mandatory since the drag force term has no real physical meaning in a stratified free-surface flow as it has in a dispersed flow – its presence in the momentum equation is due to averaging process used in derivation of two-fluid model. Thus, only the drag force is only considered in this thesis. The general formulation of interphase drag is given by:

$$\vec{R}_{pq} = K_{pq}(\vec{u}_p - \vec{u}_q) \tag{36}$$

where K_{pq} is drag force coefficient and $\vec{u}_p - \vec{u}_q$ is the relative velocity between the phases. In this study, the drag force coefficient is modeled using the default anisotropic drag model available in Fluent. This model allows for higher drag in the normal direction to the interface and lower drag in the direction tangential to the interface, with the default values of normal and tangential interfacial drag friction factors equal to 1e+6 and 1e+3, respectively. Hence, the equality of the phase velocities is established at the interface; the influence of bubbles in the flow is not taken into account in the present work. In addition, application of this model contributes to the stability of the computation [42].

2.1.2.3 Interphase heat transfer

The relation for computation of heat transfer across the interface between the phases involves the contributions to both sides of the interface. Since the saturation temperature liquid is assumed at this point, i.e., $T' = T_l$, and the heat flow rate from the interface to the liquid phase reduces to $\Phi_l = h_l A_i (T' - T_l) - \dot{m}_{lv} h' = -\dot{m}_{lv} h'$, the volumetric heat flow rate from the interface to the vapor phase reads:

$$\Phi_v = h_v A_i (T' - T_v) + \dot{m}_{lv} h'' \tag{37}$$

where h_v is the heat transfer coefficient at the vapor side of the interface, A_i is the interfacial area and $T' - T_v$ is the temperature difference between the interface and the vapor phase, $\dot{m}_{lv}$ is the volumetric mass transfer rate for a vapor-liquid phase pair in a phase change process, *h*" is the enthalpy of the saturated vapor at the system pressure. It is noteworthy that a heat balance between the phases exists, i.e., $|\Phi_v| = |\Phi_l|$. The heat transfer coefficient for a phase pair at the interface is given by:

$$h_{pq} = h_{qp} = \frac{\lambda_q Nu_p}{d_p} \tag{38}$$

where λ_q is the thermal conductivity of the fluid, while Nu_p and d_p are Nusselt number in the vapor phase and the user-prescribed characteristic dimension, respectively. In the present study,

the heat transfer coefficient, h_{pq}, is modeled using the two-resistance model; wherein the different correlation or expression of the heat transfer coefficient is applied at each side of the vapor-liquid interface.

At the vapor side, the heat transfer coefficient is computed using cell-size dependent Nusselt number correlation, which we proposed in this paper:

$$Nu_{p}=\frac{2\,d_{p}}{\Delta x} \tag{39}$$

where d_{p} is the user-prescribed vapor phase characteristic dimension and Δx is the approximated cell size. The derivation of Eq. (39) is given in Appendix A. Note that the vapor phase diameter, d_{p}, defined in Eq. (39) is canceled, when it is substituted into Eq. (38). Thus, an arbitrary value can be given as d_{p}. The cell size is calculated as:

$$\Delta x=\sqrt[3]{V_{c}} \tag{40}$$

where V_{c} is the volume of a cube (cell volume).

At the liquid side, the saturation temperature is maintained at the interface using the zero-resistance model. This model refers to application of a large heat transfer coefficient, $h_{v} \rightarrow +\infty$, to ensure the saturation temperature at the interface throughout the computation process. This idea corresponds to the application of large coefficient method to fix the saturation temperature at the interface, as discussed in the work from Perez-Raya and Kandlikar [13].

2.1.2.4 Interphase mass transfer

The mass transfer at liquid-vapor interface is modeled using the thermal phase change model implemented in Fluent that reads:

$$\dot{m}_{lv}=-\frac{C_{v}h_{v}A_{i}\left(T_{v}-T'\right)+C_{l}h_{l}A_{i}\left(T_{l}-T'\right)}{r_{0}} \tag{41}$$

where A_i is the interfacial area computed with Eq. (35), T' is saturation temperature, r_0 is the latent heat of vaporization, C_v and C_l are, respectively, vapor and liquid phase's scaling factors, h_v and h_l are, respectively, the heat transfer coefficients at vapor and liquid side of the interface, while T_v and T_l are temperatures of vapor and liquid phase, respectively.

In Eq. (41), C_v and C_l equal to unity theoretically, although they are treated as the tuning parameters in Fluent. Since we intend to obtain a solution of the governing equations without introducing any tuning parameters except computational mesh, they are set to be unity in this thesis.

2.1.3 Discretization of equations

The interpolation near the interface is accomplished using geo-reconstruct scheme. Furthermore, the momentum and energy equations are discretized using second-order upwind interpolation scheme. The pressure equation is solved with PRESTO! method [38], while the gradient discretization is carried out using a cell-centered least squares method. The coupling between pressure and velocity fields is realized using phase coupled SIMPLE algorithm. The governing equations are discretized in time using the implicit first-order Euler method.

2.2 Model verification

2.2.1 Additional relevant studies

Prior to proceeding to the verification case, the Stefan problem – a one-dimensional planar interface evaporation via the method proposed herein; we need to outline two studies that were not mentioned in the introduction part, that cover important aspects of the present model. Furthermore, two additional studies that address other important features of the present model are also covered.

2.2.1.1 Two-fluid solution to Stefan problem

The application of two already mentioned two-fluid model formulations with the identifiable interface, namely: LIM and LBM, were used in the solution to Stefan problem presented in Fleau [43]. The author clearly shows the amount of cells involved to describe the interface, and the corresponding temperature field. However, in contrast to the current study, extensive computations of two-phase flow in LES framework have been carried out.

2.2.1.2 Local mass transfer and/or non-uniform/triangular meshes

The idea of incorporation of a gradient of volume fraction field into a model that relies on empirical constant is proposed in Chen *et al.* [44]. By considering the cell size, Chen's approach can be applied to non-uniform quadrilateral mesh. The idea behind involvement of gradient of volume fraction in a mass transfer model has been explained in Kharangate *et al.* [40]. Thus, the closures, i. e., the source terms in the governing equations sets, that encompass the gradient of volume fraction field are applied in vicinity of the interface and interfacial cell itself; however, in the study carried out by the authors, within the context of falling film evaporation using single-fluid VOF method. The application of interface tracking method in solution of phase change using unstructured meshes is shown in PhD thesis by Pertant and Balarac [45]. The authors has demonstrated the solution to film boiling that occurs on a horizontal surface using triangular grid.

2.2.2 Theoretical solution of Stefan problem

The analytical solution of Stefan problem, presented here, refers to expressions for computation of interface position and temperature distribution during planar interface evaporation in the system composed of superheated vapor and saturated liquid, reinterpreting thereby the work of Perez-Raya and Kandlikar [17]. The equations involved in derivation process are the energy balance at the interface and one-dimensional heat conduction equation in a continuum. In what follows, a concise exposition of the theoretical framework is given.

2.2.2.1 Conditions at the interface

In the analytical solution used in this study, the interface condition that accounts only for occurrence of heat conduction in the system is incorporated. This is because in the case with superheated vapor and saturated liquid the heat transfer takes place only in vapor phase,

$$\frac{\partial T_1}{\partial x}=0 \tag{42}$$

Hence, the interface condition is given by:

$$X'(t)\rho_v r_0=-\lambda_{vap}\left.\frac{\partial T}{\partial x}\right|_{X(t)} \tag{43}$$

where $X'(t)$ is the interface velocity, ρ_v is the vapor density, r_0 is the latent heat, λ_{vap} is the thermal conductivity of the vapor, while the negative signed gradient denotes heat flux in normal direction to the interface. Therefore, the mass generated in phase change process is proportional to the balance of the heat fluxes applied from each phase in normal direction to the interface.

2.2.2.2 Interface position

In order to derive analytical model for this moving boundary problem, introduction of similarity variable, η, is required to relate the spatial coordinate, x, and time, t, as:

$$\eta=x/\sqrt{t} \tag{44}$$

Written in terms of the interface position, that is, $x=X(t)$ and $\eta=\xi$, this relation yields the equation for determination of interface displacement:

$$X(t)=\xi\sqrt{t} \tag{45}$$

where ξ is the constant that has to be determined using iterative procedure. The derivation of Eq. (45) with respect to time gives the interface velocity:

$$X'(t)=\frac{\xi}{2\sqrt{t}} \tag{46}$$

The substitution of Eq. (46) into Eq. (43) and involvement of solution that is obtained from incorporation of similarity variable in one-dimensional unsteady heat conduction equation gives:

$$\chi r_0=\frac{c_v(T_w-T')}{\sqrt{\pi}\exp(\chi^2)\mathrm{erf}(\chi)} \tag{47}$$

where χ is constant that has to be determined using an iterative procedure, c_v is the specific heat capacity of the vapor, T_w is the temperature of the superheated wall and T' is the saturation temperature. The constant χ embeds the value of similarity variable at the interface, that is, the constant ξ, and is defined as:

$$\chi=\frac{\xi}{2\sqrt{a_v}} \tag{48}$$

where a_v is the thermal diffusivity of the vapor phase. Substitution of Eq. (48) into Eq. (46) yields the instantaneous interface position in the case with superheated vapor and saturated liquid [17]:

$$X(t)=2\chi\sqrt{a_v t} \tag{49}$$

In the cases where initial vapor layer is needed for computational purposes, the necessary time shift of the simulation time is accomplished using Eq. (49).

2.2.2.3 Temperature field

The analytical solution of the temperature field inside the system composed of two phases, vapor and liquid, distinguished by a sharp interface, is derived from the partial differential equation (PDE) for one-dimensional unsteady heat conduction in a single continuum. The time and space coordinates present therein are transformed using the similarity variable

introduced in the previous section. Two boundary conditions are required to obtain the solution of the PDE: at the interface and at the wall. The temperature distribution at certain time instance, t, is computed as:

$$T_a(x,t) = T_w - (T_w - T') \frac{\operatorname{erf}\left(\frac{x}{2\sqrt{a_v t}}\right)}{\operatorname{erf}(\chi)} \tag{50}$$

2.2.3 Conditions of simulations

2.2.3.1 Material properties

Since our final objective of the simulations is an application to engineering problems, we select the water as the working fluid instead of an artificial material. The properties of the water at 1.013 bar are listed in Table 2. The saturation temperature is 373.15 K at this system pressure.

2.2.3.2 Computational domain and boundary conditions

The computational domain is designed as a beam divided into finite number of cells in the x-direction of the two-dimensional (2-D) Cartesian coordinate system and with one cell layer in the y-direction, i.e. a special case of 2-D domain that is also known as 1.5-D mesh. A schematic view of the computational domain together with the boundary conditions and initial phase distribution is shown in Fig. 5.

Table 2. The properties of vapor and liquid at 1.013 bar [46].

	Density [kg/m^3]	Specific heat capacity [kJ/(kg K)]	Dynamic viscosity [μNs/m^2]	Thermal conductivity [W/(m K)]	Latent heat of vaporization [kJ/kg]
Vapor	0.597	2.03	12.55	0.025	2256.7
Liquid	958.3	4.22	277.53	0.679	

The left boundary of the computational domain is the wall, where the constant superheat of 10 K, ΔT, is prescribed for all the simulation cases. The symmetry condition is imposed on the top and bottom boundaries to ensure the one-dimensionality. The right boundary is defined as the pressure outlet, with prescribed value of volume fraction and the bulk liquid's temperature.

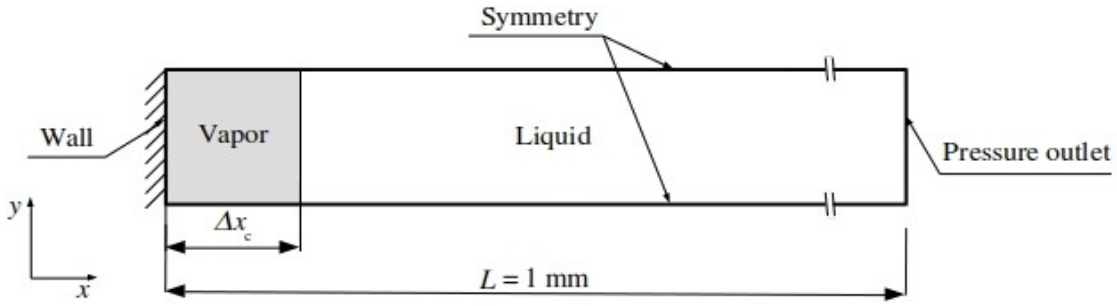


Fig. 5. A schematic representation of the domain accompanied with the applied boundary conditions and initial phase distribution.

2.2.3.3 Initial conditions

The vapor volume fraction is set to unity in the first cell adjacent to the superheated wall, while in the remainder of the domain is set to zero; a vice versa approach is applied for liquid volume fraction as depicted in Fig. 6a. Here Δx_c is the cell length of the wall adjacent cell. The velocity fields of both phases are initially set to zero in all the cells throughout the domain. The initial vapor temperature inside the vapor phase is defined by linear profile changing from $T' + \Delta T$ to T' as illustrated in Fig. 6b. The initial liquid temperature is, on the other hand, set to T' in the whole domain.

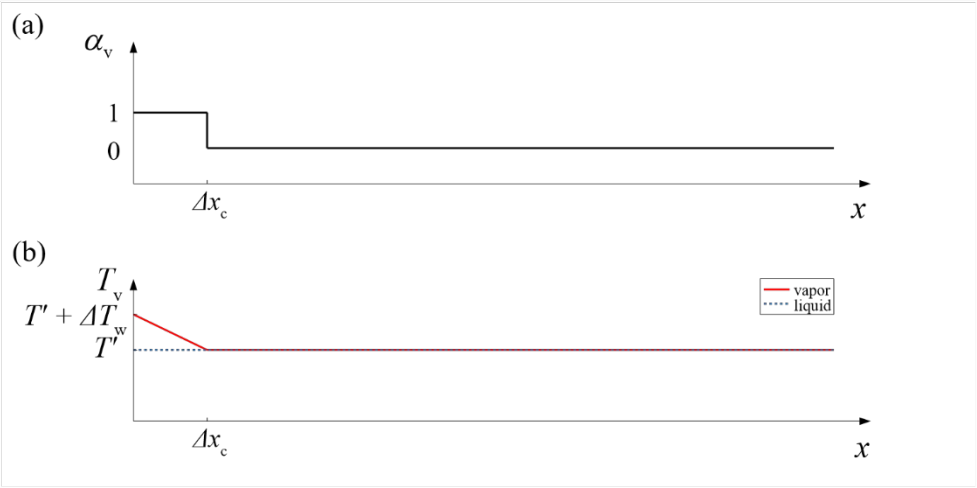


Fig. 6. The initial condition of the vapor volume fraction (a) and the vapor temperature (b).

2.2.3.4 Computational mesh

The presented numerical model for solution of Stefan problem using two-fluid VOF model has been assessed to three different types of computational meshes: (a) uniform quadrilateral, (b) stretched quadrilateral and (c) the hybrid of stretched quadrilateral and triangular cells (hereinafter also named hybrid mesh), as shown in Fig. 7, respectively. The mesh is generated by using the GMSH code [47].

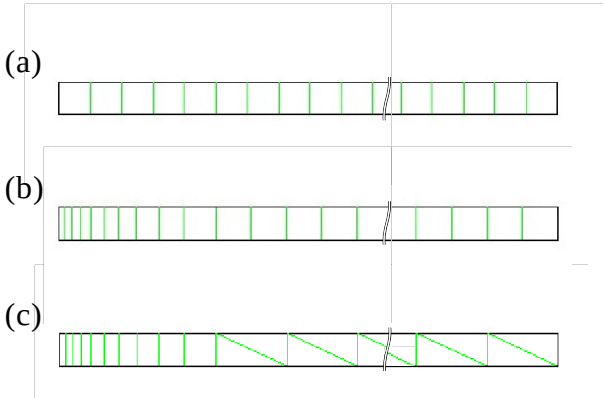


Fig. 7. Types of meshes used in computations: (a) uniform quadrilateral, (b) stretched quadrilateral and (c) hybrid of stretched quadrilateral and triangular cells.

The first mesh type is referred as the standard mesh, while the last two types serve to prove the capability of the proposed model under more realistic conditions regarding computational domain, that is, when the gradients of the dependent variables are computed using graded mesh in wall adjacent region. With respect to mesh resolution, the model verification is carried out using meshes with 50, 100 and 200 cells, hereinafter also named coarse, medium and fine, respectively. The graded mesh, where included, is composed of ten quadrilateral cells with an expansion ratio of 1.2, while the number of cells with the dominant cell-shape has been varied.

The time steps applied in the simulations are mesh resolution dependent and written in Table 3. The total simulation time is divided into two parts. Firstly, the simulation is run for 0.1 ms to obtain more accurate initial distribution of interface displacements; otherwise, an initial discrepancy from the analytical solution is observed that shifts the normal interface evolution to later time. Thus, two-orders of magnitude lower time step size than in the remainder of simulation is used together with the number of time steps that is 10 % of the number of time steps in the second part of the simulation. Then, the simulation is run for 0.1 s with increased time step size. Furthermore, due to presence of initial vapor cell in the simulation, the simulation time has to be shifted for a constant value obtained from Eq. (49). Therefore, the results at specific time instances are obtained using linear interpolation from neighboring values.

Table 3. A general, mesh size dependent, time stepping procedures applied for the uniform and stretched meshes.

Number of cells	Simulation time				Total simulation time [s]
	First part		Second part		
	Number of time steps	Time step size [s]	Number of time steps	Time step size [s]	
50	20	5.00e-6	200	5.00e-4	0.1
100	40	2.50e-6	400	2.50e-4	
200	80	1.25e-6	800	1.25e-4	

The simulations carried out using medium and fine hybrid meshes required, however, finer time step sizes, listed in Table 4.

2.2.3.5 Implementation in Fluent

Since the two-fluid modeling approach utilized the concept of interpenetrating continua, in each cell of the computational mesh the relevant dependent variable's has to be assigned for both phases. Thus, three field variables are initialized on a per phase basis using Define-Init User-Defined Function (UDF) macro: volume fraction, velocity and temperature. Furthermore, the proposed correlation for computation of the heat transfer coefficient, Eq. (38), is incorporated into the Fluent code using Define-Exchange-Property UDF macro. Finally, in the cases where the hybrid mesh is used, the interface position is calculated using Define-Report-Definition-FN UDF macro.

Table 4. Time stepping procedures for the cases of certain hybrid meshes.

Number of cells	Simulation time				Total simulation time [s]
	First part		Second part		
	Number of time steps	Time step size [s]	Number of time steps	Time step size [s]	
100	80	1.25e-6	800	1.25e-4	0.1
200	100	1.00e-6	1000	1.00e-4	

In all the computations, the default relaxation factors for the iterative calculations implemented in Fluent were used.

2.2.4 Results and discussions of the verification case

2.2.4.1 Definition of the interface position

In the computations performed with the meshes composed of quadrilateral cells, the interface is considered as an iso-surface of vapor volume fraction equal to 0.5, that is, $\alpha_v = 0.5$.

Thus, the information on interface position is obtained by tracking the *x*-coordinate of the iso-surface. In the case of hybrid mesh, inside the mesh region composed of triangular cells, this definition of interface, however, leads to interface distributed over two or more cells in a piecewise-linear segments. Therefore, a cell-shape independent approach is used, with the interface position given by:

$$X(t)=\frac{\sum_{i=1}^{n}\alpha_{\mathrm{v},i}V_{\mathrm{c},i}}{\sum_{i=1}^{n}V_{\mathrm{c},i}}L \tag{51}$$

where $\alpha_{\mathrm{v},i}$ is the vapor volume fraction in *i*-th cell, $V_{\mathrm{c},i}$ is *i*-th cell's volume and L is the length of the domain. The sum in denominator of Eq. (51) is the volume of the domain.

2.2.4.2 Definition of computational errors

We define the computational errors of the interface position and the temperature field here. The relative error of the interface position at time *t* is given by:

$$E_{\mathrm{X}_i}(t)=\frac{|X_{i,\mathrm{a}}(t)-X_{i,\mathrm{n}}(t)|}{X_{i,\mathrm{a}}(t)} \tag{52}$$

where $X_{i,\mathrm{a}}(t)$ and $X_{i,\mathrm{n}}(t)$ refer to the *x*-coordinate of the interface position obtained from the analytical solution and the numerical simulation, respectively. In this study, the relative error of the interface position is calculated for two time instances: in the middle of the simulation, $t=t_{\mathrm{end}}/2$, and at the end of the simulation, $t=t_{\mathrm{end}}$.

We evaluate the relative error in the temperature field at the end of the simulation time which is defined as:

$$E_{\mathrm{T}}=\max\left(E_{\mathrm{T}}(x_{\mathrm{c}1},t_{\mathrm{end}}),E_{\mathrm{T}}(x_{\mathrm{c}2},t_{\mathrm{end}}),\ldots,E_{\mathrm{T}}(x_{\mathrm{cn}},t_{\mathrm{end}})\right) \tag{53}$$

where $E_T(x_{ci}, t_{end})$ is the error of the temperature at the cell center of *ci*-th cell calculated by:

$$E_T(x_{ci}, t_{end}) = \frac{\left| T_a(x, t_{end}) - T_n(x_{ci}, t_{end}) \right|}{\Delta T_w} \tag{54}$$

where $T_a(x, t_{end})$ and $T_n(x, t_{end})$ are the temperatures at the location of the cell center, x, for the analytical solution and the numerical simulation, respectively, and ΔT_w is wall superheat. The temperature of the vapor is used for T_n, although in the two-fluid modeling approach two energy equations are solved and two temperature fields are present in the domain. This is because the temperature field calculated from the energy equation of the liquid phase is constant at the saturation temperature.

2.2.4.3 Uniform mesh

The advancement of vapor-liquid interface in the performed numerical simulation reproduces the analytical solution with a commensurate level of accuracy. This is shown in Fig. 8a. Additionally, the obtained result is supplemented with ± 2 % error band in order to make a stringent estimation of solution accuracy, as indicated in Figs. 8b and 8c.

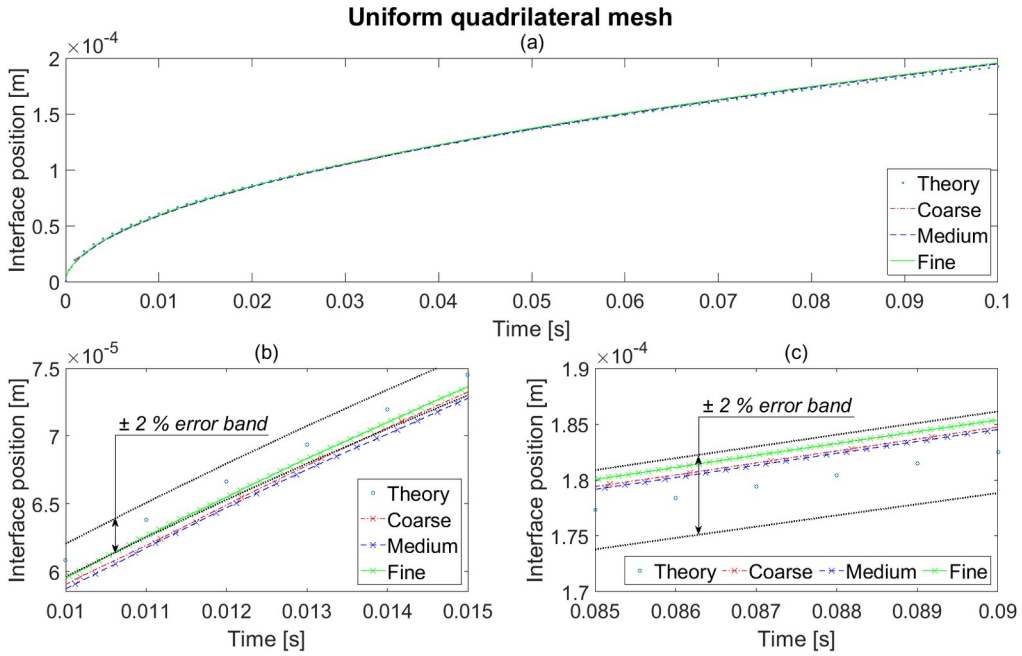


Fig. 8. Evolution of the interface position using the uniform quadrilateral mesh: (a) for the whole simulation time, (b) the detailed view at the beginning, and (c) near the end of the simulation.

The comparison between Fig. 8b and Fig. 8c, together with exact values given in Table 5, points out that increased mesh resolution does not necessarily provide the result that is more accurate. This is in accordance with the study in Gauss *et al.* [29], where is shown that, when two-fluid model is used in typical interface tracking case, the solution is not fully dependent on the mesh size. Here, close to the start of the computation, within the period from 10 % to 15 % of the total simulation time (Fig. 8b), the solution obtained on fine mesh exhibits the highest accuracy. However, when the end of the simulation is being approached, that is, 85 % to 90 % of the prescribed total time (Fig. 8c), the result obtained using medium mesh is found as the most accurate.

Table 5. The relative computational error in estimation of interface position at selected two time instances for different resolutions of uniform quadrilateral mesh.

Mesh type	Number of cells	Relative error in interface position [%]	
		$t = 0.05$ s	$t = 0.1$ s
Uniform mesh	50	0.54	1.38
	100	0.28	1.24
	200	0.91	1.70

The temperature field inside the domain at $t = 0.1$ s exhibit distributions shown in Fig. 9. Near the interface a discrepancy from exact, linear, temperature profile is observed. In this case the increased mesh resolution leads to more accurate result, as quantified in Table 6.

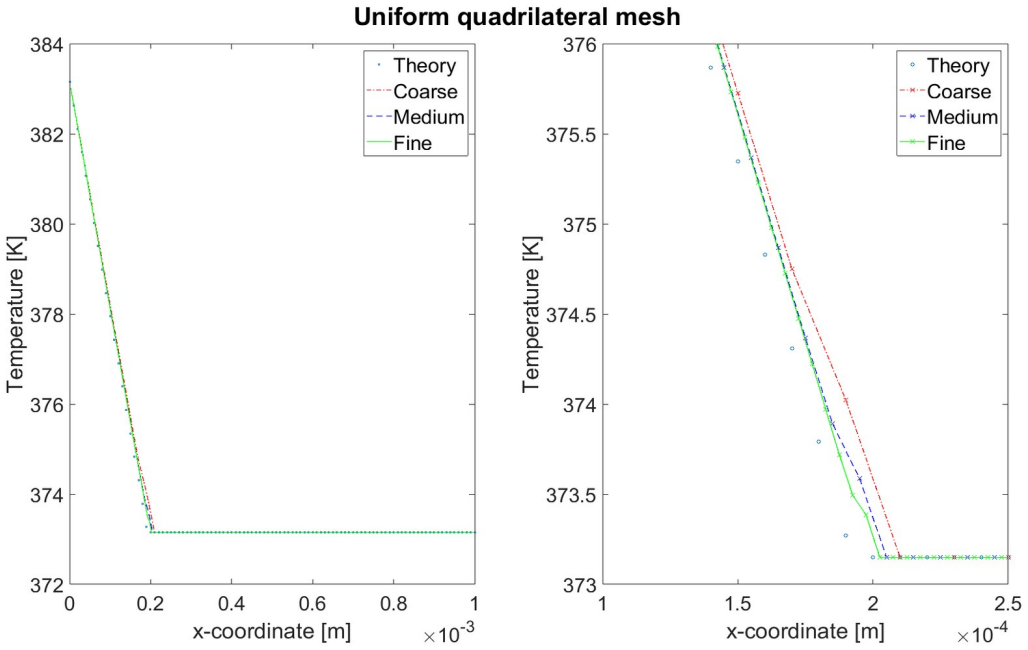


Fig. 9. The comparison of temperature at t = 0.1 s between the analytical solution and the simulation: whole domain (left) and the closer view near the interface (right).

Table 6. The maximum relative computational error in estimation of vapor phase's temperature field inside the domain at t = 0.1 s for uniform quadrilateral mesh.

Mesh type	Number of cells	Maximum relative error in temperature field [%]
Uniform mesh	50	7.49
	100	4.38
	200	3.44

Since the solution of Stefan problem with the approach presented here improves the standard solutions obtained with single-fluid approach, it is noteworthy to outline some additional features of the model.

The consideration of liquid phase at saturation temperature imposes as the primary goal to study the vapor phase's temperature field. However, due to application of two-fluid model, there is

also a temperature field associated with liquid phase that is distributed throughout the domain, as shown in Fig. 10. Fixing the liquid phase's temperature at the interface to saturation temperature by application of zero-resistance heat transfer model ensures stagnant temperature profile of the liquid, present also in the cell adjacent to interface zone with $\alpha_l=0$ that is preceded by a jump in temperature decrease.

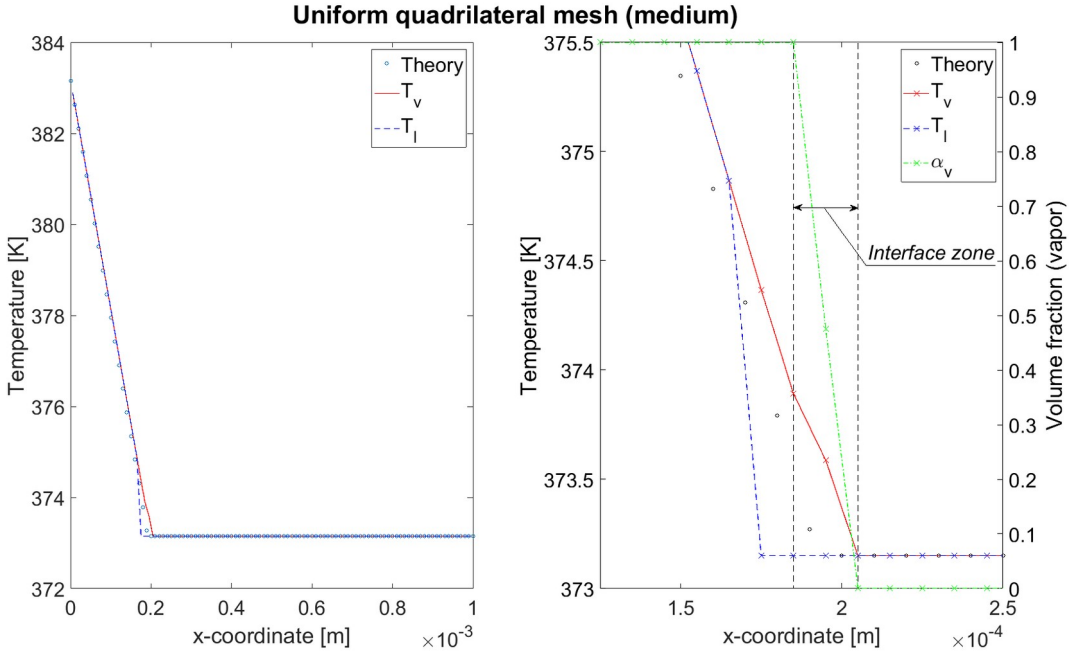


Fig. 10. The vapor and liquid phase's temperature distributions in the domain composed of 100 quadrilateral, uniformly distributed, cells compared with analytical solution and accompanied with distribution of vapor volume fraction: whole domain (left) and the closer view near the interface (right); the markers denote cell center values. The plot represent the result at $t = 0.1$ s.

The tendency to equalize the velocities of the phases by application of the appropriate drag model, mentioned before, is shown in Fig. 11. The close agreement of the maximum velocity magnitude of the vapor (square marked) and liquid phase's velocity magnitude is outlined in the interface zone.

The liquid phase's temperature distribution and the velocity magnitude field of both phases are general features of the model and, therefore, are not considered further in this study.

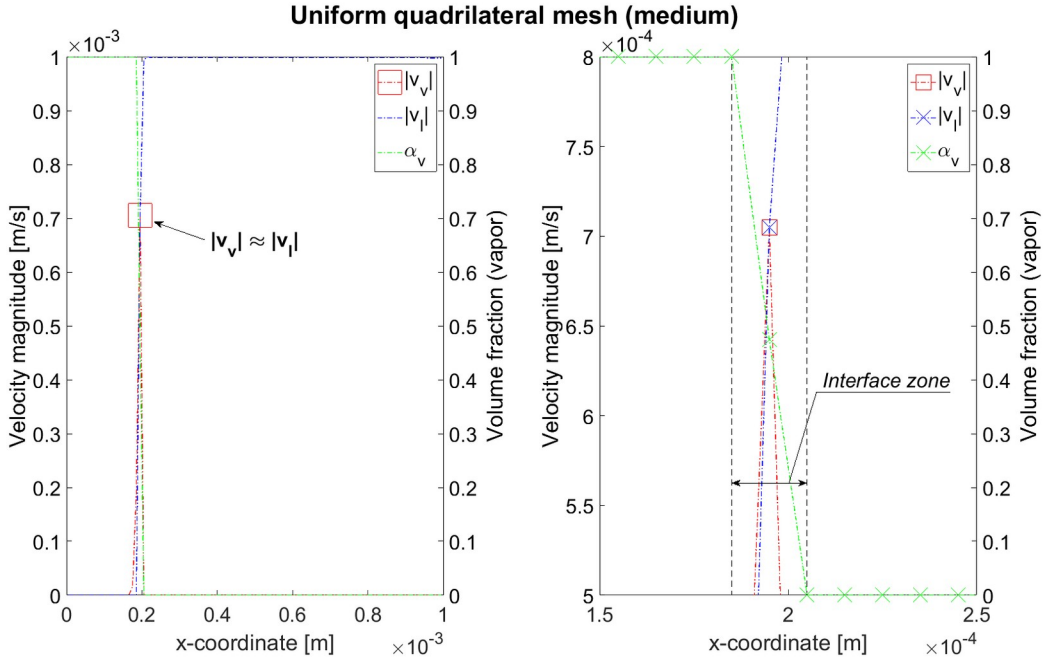


Fig. 11. The distribution of vapor and liquid phase's velocity magnitude field in the domain composed of 100 quadrilateral, uniformly distributed, cells together with the profile of vapor volume fraction: whole domain (left) and the closer view near the interface (right); the markers denote cell center values. At $t = 0.1$ s.

2.2.4.4 Non-uniform meshes

2.2.4.4.1 Stretched quadrilateral mesh

The incorporation of stretched mesh in near wall region of a quadrilateral mesh also results in accurate estimation of interface displacement, as shown in Fig. 12a. Although shortly after the simulation start only the result obtained on the fine mesh enters the prescribed error band, as displayed in Fig. 12b, finally, as shown in Fig. 12c, it is accompanied with the coarse mesh solution.

According to exact measures, at two selected time instances, as indicated in Table 7, the interface displacement solution obtained with fine stretched quadrilateral mesh is more accurate than the solution obtained with quadrilateral uniform mesh of same number of cells. The medium mesh that yields most accurate interface displacement in the selected time instances in the case of uniform cell distribution, however, in this case has highest discrepancy, but still in reasonable limit, that is, lower than 5 %.

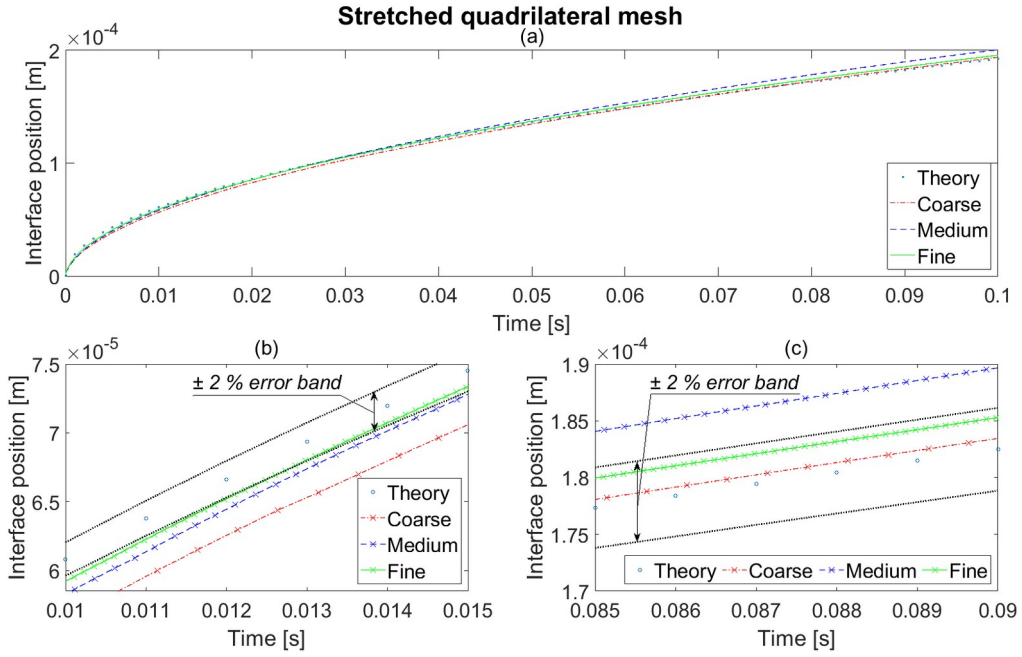


Fig. 12. Evolution of the interface position using the stretched quadrilateral mesh: (a) for the whole simulation time, (b) the detailed view at the beginning, and (c) near the end of the simulation.

Table 7. The relative computational error in estimation of interface position at selected two time instances for different resolutions of stretched quadrilateral mesh.

Mesh type	Number of cells	Relative error in interface position [%]	
		$t = 0.05$ s	$t = 0.1$ s
Stretched quad.	50	0.97	0.69
	100	2.25	4.22
	200	0.80	1.65

The temperature field obtained using stretched quadrilateral meshes, shown in Fig. 13, has the maximum relative error in computation of temperature field lower than 10 %, when all the applied mesh resolutions are considered, Table 8. In the case of medium mesh, however, the better results are obtained in the case without stretched cells in wall adjacent zone.

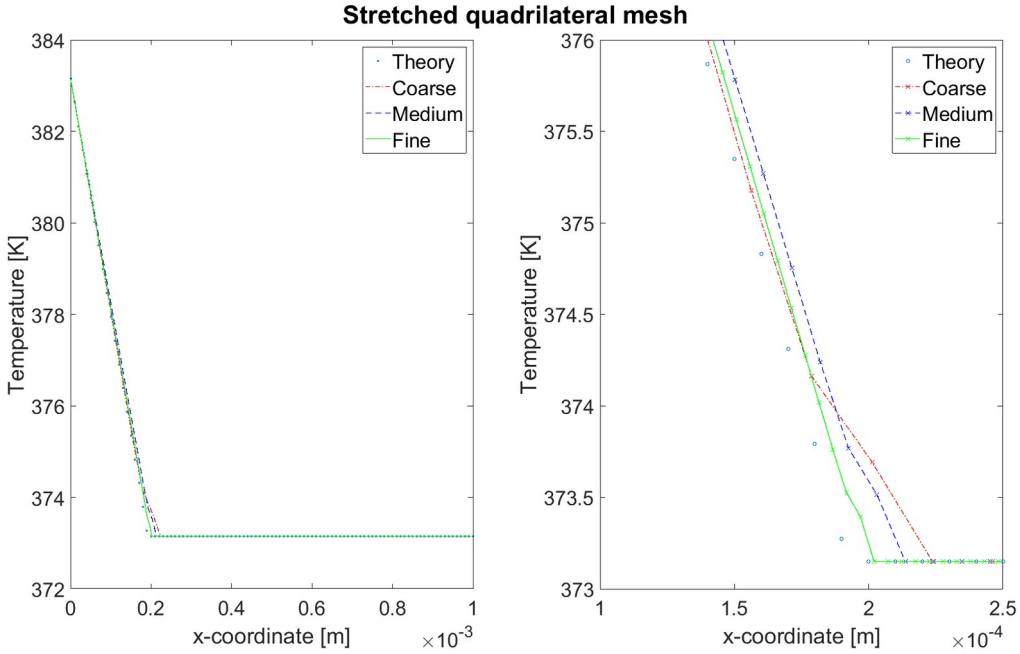


Fig. 13. The comparison of temperature at t = 0.1 s between the analytical solution and the simulation: whole domain (left) and the closer view near the interface (right).

Table 8. The maximum relative computational error in estimation of vapor phase's temperature field inside the domain at t = 0.1 s for different resolutions of stretched quadrilateral mesh.

Mesh type	Number of cells	Maximum relative error in temperature field [%]
Stretched quad.	50	5.43
	100	6.19
	200	3.45

2.2.4.4.2 Hybrid mesh

The interface displacement in the case of hybrid mesh is calculated using Eq. (51) and exhibits the distribution shown in Fig. 14. Although detailed view in Fig. 14b suggests the solution obtained using the fine mesh as the most promising one, the result in Fig. 14c together with the exact values of the interface displacement error, given in Table 9, indicate the reliability of medium size mesh.

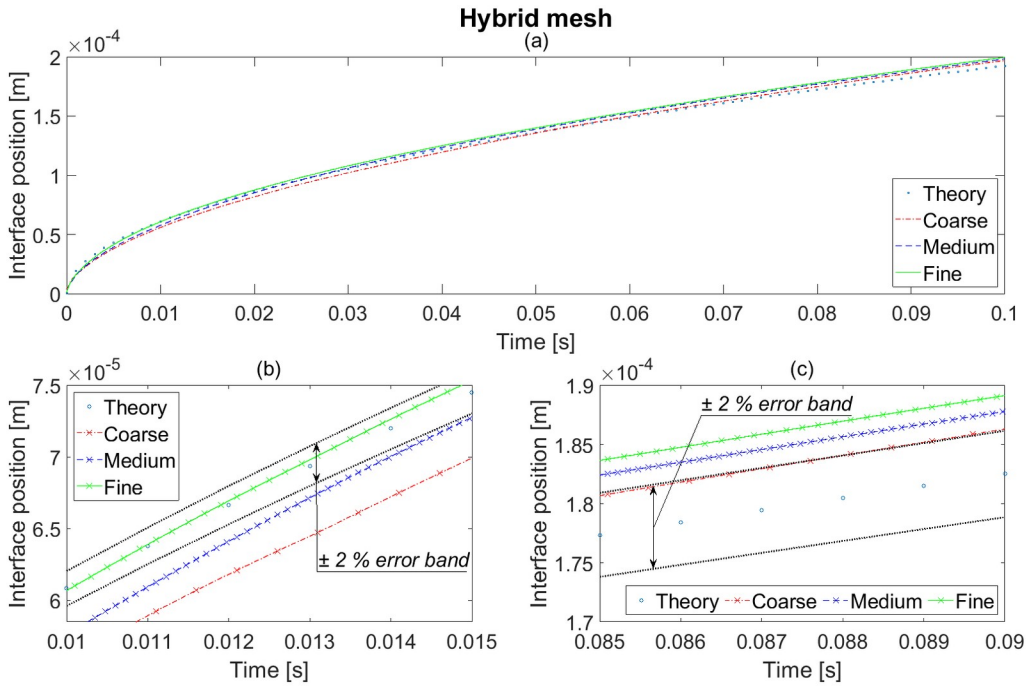


Fig. 14. Evolution of the interface position using the hybrid mesh: (a) for the whole simulation time, (b) the detailed view at the beginning, and (c) near the end of the simulation

Table 9. The maximum relative computational error in estimation of vapor phase's temperature field inside the domain at t = 0.1 s for different resolutions of hybrid mesh.

Mesh type	Number of cells	Relative error in interface position [%]	
		t = 0.05 s	t = 0.1 s
Hybrid mesh	50	0.31	2.36
	100	2.09	3.06
	200	2.88	3.79

Sampling the temperature field data from cell's centers yields a "zig-zag" temperature field distribution inside the zone composed of triangular cells in the hybrid mesh, as shown in Fig. 15. The error in computation of temperature field for coarse and medium resolution mesh is in the range of the errors already reported for other types of meshes with these resolutions, that is, less than 10 %. However, the maximum relative temperature field error obtained using fine mesh at the simulation end time is, compared to fine mesh calculations with other mesh types, the largest, Table 10.

The distribution of the volume fraction of the vapor phase and the temperature for the hybrid mesh at $t = 0.1$ s are shown in Fig. 16. The volume fraction sharply changed from zero to one, and the temperature field features linear change from the wall temperature to the saturation temperature in the vapor phase.

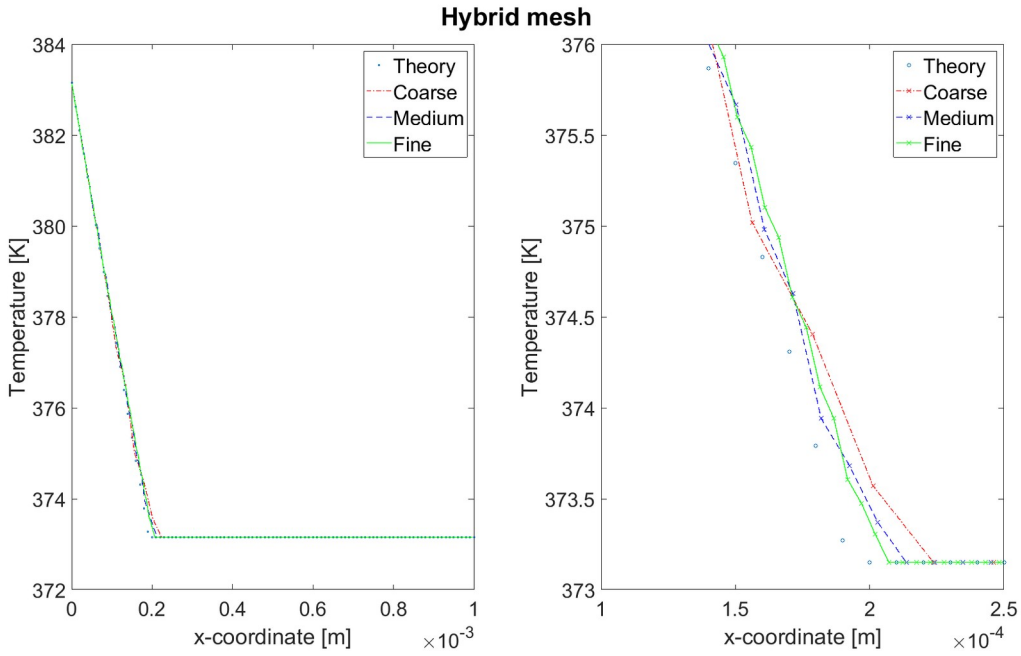
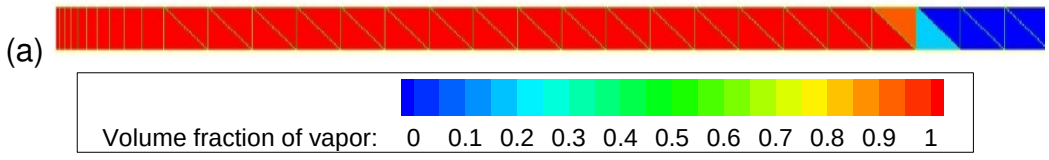


Fig. 15. The comparison of temperature at t = 0.1 s between the analytical solution and the simulation: whole domain (left) and the closer view near the interface (right).

Table 10. The maximum relative computational error in estimation of vapor phase's temperature field inside the domain at t = 0.1 s for different resolutions of hybrid mesh.

Mesh type	Number of cells	Maximum relative error in temperature field [%]
Hybrid mesh	50	5.49
	100	5.32
	200	4.96



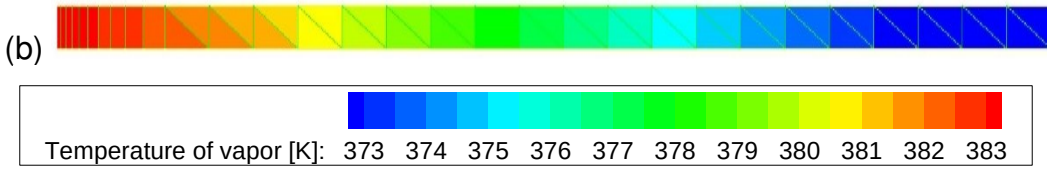


Fig. 16. Distribution of (a) volume fraction of vapor and (b) vapor temperature for the hybrid mesh.

2.3 Model validation

2.3.1 Description of the validation experiment

A film boiling experiment in the case of saturated and subcooled bath medium is reported in Momoki *et al.* [1], and used as a validation study in this work. The specimens of different sizes were submerged into liquid coolant and the temperature distribution was measured in the specimen center. The specimens were made of silver, thus, due to small Biot number, that is, $0 < Bi < 0.1$, a lumped transient heat conduction model is relevant for estimation of solid temperature due to inexistence of significant temperature gradients with respect to space coordinates in the solid body. A sheathed K-type thermocouple was placed in the center of the specimen, and the sampling time was 0.25 s.

In the context of present work, a cylinder specimen with dimensions 45 mm in diameter and 45 mm in length, for which the transient temperature distribution is available, is used as a validation benchmark. The specimens that are made of materials without structural transformation during the process are used in determination of cooling characteristics of a quenchant medium.

2.3.2 Additional considerations regarding turbulent flow modeling

By insertion of an average turbulent kinetic energy in all the cells except the ones in the immediate neighborhood of the heat transfer surface, i. e. the specimen surface's adjacent cells, one may enhance the heat extraction from the solid and thus achieve better agreement with the experimental data.

This is due to the enhanced heat flux at the interface that reads [21]:

$$\vec{q}_{\mathrm{n}} = (\lambda + \lambda_{\mathrm{t}}) \frac{\partial T}{\partial \vec{n}}, \tag{55}$$

where λ is molecular thermal conductivity (W/m K), λ_{t} is the turbulent thermal conductivity (W/m K), and $\partial T / \partial \vec{n}$ is the temperature gradient in the normal direction to the interface. Joining together molecular and turbulent thermal conductivity gives effective thermal conductivity:

$$\lambda_{\mathrm{eff}} = \lambda + \lambda_{\mathrm{t}}. \tag{56}$$

Analogous to the turbulent kinematic viscosity, ν_{t}, that is a flow quantity and is present only if the flow is turbulent, the turbulent thermal conductivity is also a flow quantity.

In the validation case, the flow is considered as turbulent, although the turbulence transport equations are not being solved; yet the turbulent kinetic energy (TKE) is prescribed in all the cells of the computational domain, thus affecting the turbulent dynamic viscosity, μ_{t}, and, correspondingly, the turbulent thermal conductivity.

The turbulent viscosity is directly proportional to the square of turbulent kinetic energy, $\mu_{\mathrm{t}} \propto TKE^2$, and is involved in computation of effective thermal conductivity, Eq. 56. While the molecular thermal conductivity is well-known physical property of a continuum, the turbulent thermal conductivity is computed analogously to the molecular Prandtl number, using the turbulent Prandtl number that is defined as follows:

$$Pr_{\mathrm{t}} = \frac{\mu_{\mathrm{t}} c_{\mathrm{p}}}{\lambda_{\mathrm{t}}}. \tag{57}$$

Hence, the effective thermal conductivity has the following form:

$$\lambda_{\mathrm{eff}} = \lambda + \frac{\mu_{\mathrm{t}} c_{\mathrm{p}}}{Pr_{\mathrm{t}}}, \tag{58}$$

where the turbulent Prandtl number is kept constant, 0.85.

This approach can be referred as the “frozen turbulence” approach, since the governing equations of turbulent transport are not being solved, yet the turbulent kinetic energy contributions to the effective thermal conductivity, and thus the heat flow rate extraction from the solid specimen, are considered by prescription of TKE values thorough the domain.

Furthermore, a dispersed formulation of realizable k-ε turbulence model has been chosen for the computations herein. Thus, only the bulk phase turbulence is modeled with transport equations, while the dispersed phase turbulence modeling is carried out using the Tchen correlation [48], according to [38].

2.3.3 Description of the case and geometry

An axis-symmetric domain is constructed with the cylinder specimen placed in the middle of the domain height, as shown in Fig. 17. The computational domain spans over the area $x \in$ [-1.025e-1, 1.025e-1] m $\times$ $y \in$ [0, 1,025e-1] m, and is composed of fluid and solid part, separated via the fluid-solid interface. At the domain top, a 15 mm high outlet region is prescribed, containing the vapor phase. In the vicinity of the solid specimen, a one-cell vapor layer is initially placed, with a thickness of 0.61 mm, required for the mass transfer model in order to induce the mass transfer. In Fig. 17, the vapor blanked is, for the sake of simplicity, enlarged.

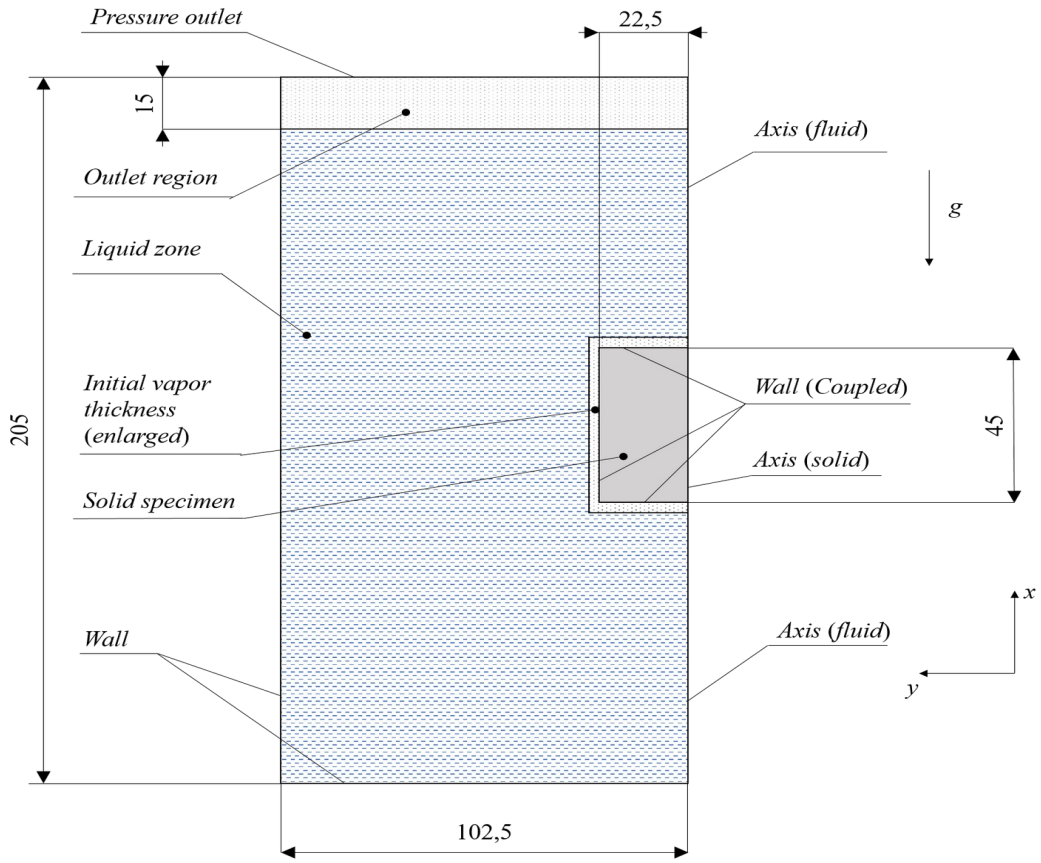


Fig. 17. A schematic representation of the validation model with the applied boundary conditions. The dimensions are in mm.

The domain is composed of 7938 quadrilateral cells (Fig. 18a), with the refined cell zone adjacent to the specimen surface (Fig. 18b). The specimen is made of silver and has equal diameter and height, 45 mm.

The boundary conditions are assigned to the domain's top, bottom, and left side surface for both the phases, whilst the domain symmetry axis is defined as "axis" in the applied software. Thus, the top of the domain is set to pressure outlet condition, with prescribed outlet temperature 100 °C for both phases and the unit backflow vapor volume fraction. The bottom and left surface are defined as solid walls. The specimen surface is composed of three walls that interact with the fluid region via "coupled" condition.

The initial conditions involve the initial distributions of phase volume fractions, temperatures and velocities, supplemented with the initial profile of turbulent kinetic energy that is, in contrast to other aforementioned dependent variables, maintained constant thorough the

simulation, since the turbulence equations are not being solved - so-called „frozen turbulence" approach. The velocity fields of both phases were initially set to zero elsewhere in the domain, although the turbulent kinetic energy is initially set to a non-zero value everywhere except the initial vapor layer.

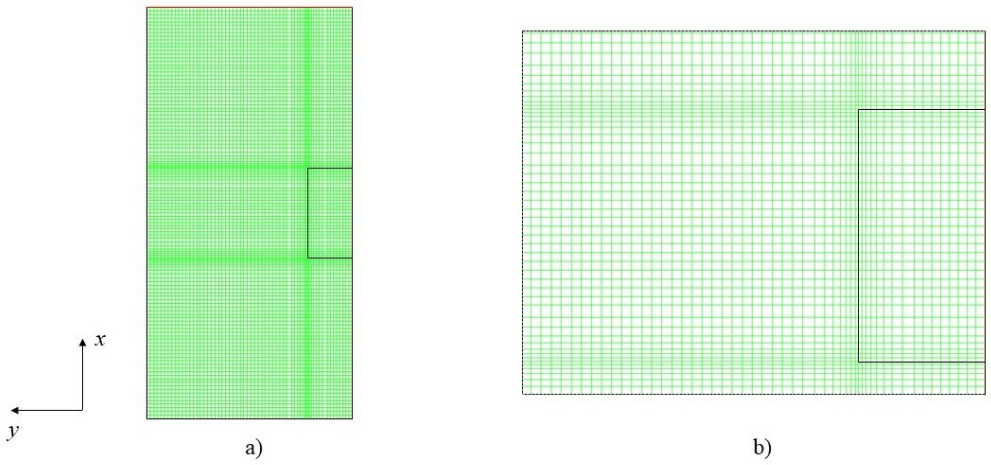


Fig. 18. The computational mesh (a), a detailed view on cell distribution in the vicinity of the fluid-solid boundary (b).

The initial temperature of a solid specimen is set to 600 °C, as per experiment in Momoki *et al.* [1]. The liquid and outlet zone were set to initial temperature of 100 °C.

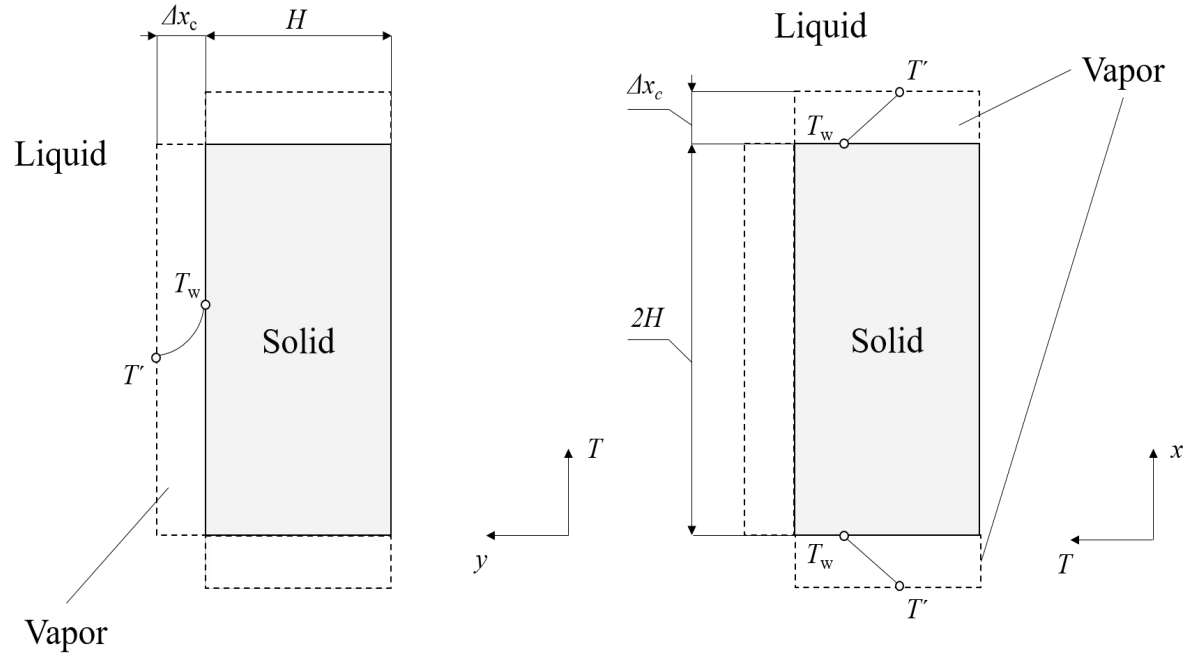


Fig. 19. A schematic representation of initial temperature field distribution: in radial direction, in vicinity of the vertical surface (left); in the immediate neighborhood of top and bottom horizontal surface (right).

Inside the vapor layer, an initial temperature field is prescribed as follows. In radial direction along the cylinder height, due to analytical solution of heat conduction equation in the radial direction of a cylindrical coordinate system, a logarithmic temperature profile is imposed as follows:

$$T_{\text{cell},i} = \frac{T' - T_{\text{w}}}{\ln\dfrac{H + \Delta x_{\text{c}}}{H}} \ln\frac{y_{\text{c},i}}{H} + T_{\text{w}}, \tag{59}$$

whilst in the axial direction, at top and bottom surfaces, respectively, it follows the linear law due to same reason as in the former case (the analytical solution to heat conduction PDE in the axial directions of the cylindrical coordinate system):

$$T_{\text{c},i} = \frac{T' - T_{\text{w}}}{\Delta x_{\text{c}}}\left(x_{\text{c},i} - H\right) + T_{\text{w}}; \tag{60}$$

$$T_{\text{c},i} = \frac{T' - T_{\text{w}}}{-\Delta x_{\text{c}}}\left(x_{\text{c},i} + H\right) + T_{\text{w}}. \tag{61}$$

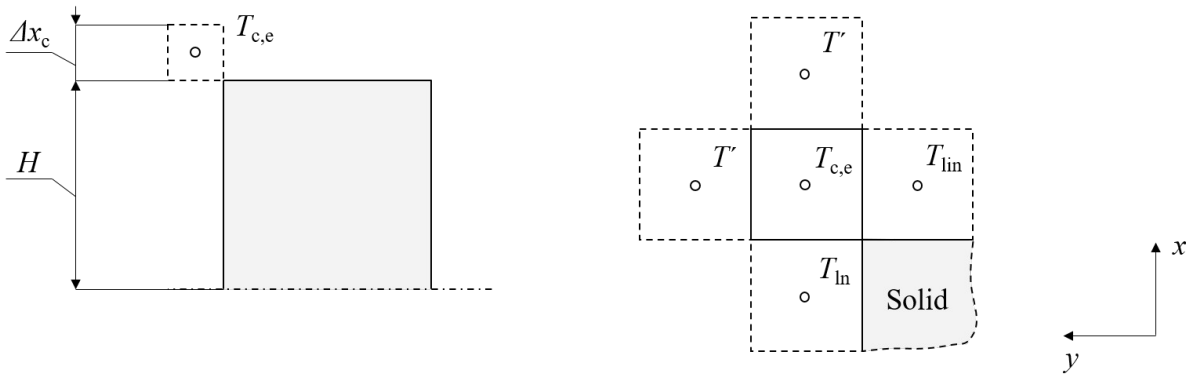


Fig. 20. A conceptual sketch on determination of initial temperature in the edge control volume.

The edge element is filled with the initial temperature computed as:

$$T_{c,i} = \frac{T_{ln} + T_{lin} + 2T'}{4}, \tag{62}$$

that stems from an energy balance on a knot in the cell center assuming thereby that face temperature of neighbor cells are those of their respective cell centers. This yields, however, the initial temperature in the edge control volume (CV) that is lower than these other two temperatures, due to cooling contributions from two sides that remain at, significantly lower, saturation temperature.

The time step applied in simulation is divided into two parts. Firstly, ten time steps with a size of 1e-6 s were carried out. Then, a 2e-4 s time step size has been applied in the remainder of the simulation.

2.3.4 Turbulent kinetic energy

The one half of the sum of principal stresses in a non-linear Reynolds stress tensor, that appears in momentum conservation equation after the Reynolds averaging of dependent variables is applied due to fluctuations of these quantities in a wide spectrum of wavelengths and frequencies, forms the turbulent kinetic energy, see e. g. in Markatos [49], as follows:

$$TKE = \frac{1}{2}\overline{v'_i v'_i}, \tag{63}$$

where v'_i is the fluctuating velocity component in the *i*-th direction (index notation). Hence, the turbulent kinetic energy is strongly interlinked with another flow variable, the turbulent viscosity, ν_t, that is relevant only for turbulent flow. Since it appears in the effective thermal conductivity term, it is thus plausible for heat rejection from a cylinder specimen. An analogy between film flow and free jet flow near the nozzle exit can be made; since the initial core with a laminar flow inside precedes the disturbed flow. The disturbance that appears in a downstream direction is a Kelvin-Helmholtz instability and is, according to Hoppe and Breurer [50], consequence of different tangential velocities across the interface between two fluids; the disturbance of this type is due to surface instabilities, and is noticeable in the case of large bubbles wherein the significant influence has the surface tension in contrast to small bubbles of small radii. The turbulent kinetic energy is, furthermore, in close relationship with turbulence intensity, an another measure of a turbulent flow. The experimental work by Philip [51] has revealed that in the case of annular jet flow, the peaks of turbulence intensities appear in the shear layers; thus, as claimed by the author, the turbulence occurs in the shear layers. The study by Kimber [52] has revealed that turbulence intensity profile closely follows the TKE distribution in a single jet flow. As per Padet [53], in a boundary layer flow over a flat surface, the TKE is being generated at the interface between the viscous sub-layer and logarithmic layer. It is the bubble induced turbulence (BIT), studied in Ničeno *et al*. [54], wherein the liquid flow is turbulent, whilst the flow inside the vapor phase is laminar. Another analogy is with the flow of breaking sea vawes in the surf zone; the studies of Kashima *et al*. [55] and Mori *et al*. [56] provide more detail in this regard; while the numerical assessment of this topic has been presented in the simulation in Makris *et al*. [57]. The authors conducted a detailed study using a Lagrangian method that corresponds to LES approach.

As per Cascioli *et al*. [58], in a co-flow of a jet, a strong shear between the jet and surrounding fluid domain contributes to turbulent kinetic production; on the other hand, the overall heat transfer rate, extracted from the solid object and transferred to the vapor-liquid interface, is significantly dependent on flow condition, i. e., the shear force driving the flow of liquid in the immediate neighborhood of the interface, as can be concluded from theoretical exposure given in Sakurai *et al*. [59].

As in the case of the jet or liquid film flow, in film boiling around a vertical cylinder two distinct zones are defined according to Momoki *et al*. [1]: the zone of smooth interface and the zone where the interface is wavy.

In contrast to flow of liquid film, that can be represented as Coutte flow, as shown in Javed [60], or a flow film boiling, where the maximum velocity, regarding the film, is in the vicinity of the upper part of the film; in this case, i. e., the film boiling in a liquid pool, a more convenient approximation is a pipe flow, that is, a non-slip condition at the outer surface of the film.

It is interesting to note, however, that these values correspond to a great extend to the ones obtained with the equation for turbulent kinetic energy proposed in Hillier *et al* [61] that, in the context of the present research, read:

$$TKE \propto \frac{1}{4}\rho_{\mathrm{mix}}\frac{\Delta w_{\mathrm{rel}}{}^{2}\left(F_{\mathrm{v}}F_{\mathrm{l}}\right)^{\frac{1}{2}}}{\left(\sqrt{F_{\mathrm{v}}}+\sqrt{F_{\mathrm{l}}}\right)^{2}}, \tag{64}$$

where ρ_{mix} is the mixture density, Δw_{rel} is the relative velocity difference across the layer and F_{v} and F_{l} are the ratios between the density of vapor or liquid, respectively, and the sum of phase densities. The mixture density, ρ_{mix}, is defined as:

$$\rho_{\mathrm{mix}}=\left(\rho_{\mathrm{v}}\rho_{\mathrm{l}}\right)^{\frac{1}{2}}; \tag{65}$$

whilst density ratios, F_{v} and F_{l} read::

$$F_{\mathrm{v}}=\frac{\rho_{\mathrm{v}}}{\rho_{\mathrm{v}}+\rho_{\mathrm{l}}}; \tag{66}$$

$$F_{\mathrm{l}}=\frac{\rho_{\mathrm{l}}}{\rho_{\mathrm{v}}+\rho_{\mathrm{l}}}. \tag{67}$$

The velocity profile in the case of immersion quenching has, at least to a certain extend, a parabolic like profile, thus an assumption of Poiseuilles flow may be applied in obtaining the velocity distribution across the vapor layer, assuming thereby that the flow inside the layer is laminar, that is, $\lambda_{\mathrm{eff}} = \lambda$. This assumption is justified that, in the case of pool film boiling around a vertical surface of a cylinder, non-slip conditions at the interface between vapor and liquid,

and a the stationary wall of the cylinder. Hence, a parabolic-like, as in the case of pipe flow velocity profile may be considered.

The relative velocity, that is, the velocity input in the above expression has to reflect the velocities in both the phases; hence, we assume that liquid velocity is zero, due to pool boiling conditions, thus the stationary interface between the phases may be assumed, the so-called "non-slip" condition[2]. Consequently, inside the vapor film, a parabolic velocity profile may be assumed, that spreads over the vapor layer of thickness δ; hence, an averaged velocity thorough the vapor film is used in estimation of TKE, calculated from the continuity equation, that is, the mass conservation law as follows:

$$\bar{w} = \frac{q_{\mathrm{m}}}{\rho_{\mathrm{v}} \bar{\delta}_{\mathrm{m}} \pi}, \tag{68}$$

where q_{m} is the mass flow rate per unit circumference, kg/(m s), ρ_{v} is vapor phase density, kg/m^3, and $\bar{\delta}_{\mathrm{m}}$ is an average thickness of the vapor layer, m, calculated as shown in Appendix B.

The computational model for analysis of the heat transfer phenomena during film boiling on a vertical surface is proposed in Yamada *et al*. [62], being derived for the case of film boiling at the vertical plane surface. Hence, a rectification of the unit width is conducted here by multiplication with π, when a cross-section of fluid element perpendicular to the flow direction is considered in obtaining the average velocity, Eq. (68). The authors in the aforementioned article distinguish four different cases at the vapor-liquid interface, considering thereby the conditions at the bottom horizontal surface of the cylinder; hence, a non-slip condition at both, the vapor layer beneath the cylinder and at the vertical surface is taken into account in this study, due to the pool boiling conditions that are present in the flow.

The mass flow rate is defined analogously to Nusselt's film condensation theory, from the momentum balance on the fluid element, with an exception of multiplication by 1/12 instead of 1/3[3]

2 The term „non-slip" is quoted since, as shown in Liščić *et al*. [5], there is certain velocity at the interface; but, for the sake of simplicity, we neglect it in our mathematical model.

3 The multiplication of the r.h.s. terms with 1/3 is also in the case with film boiling when slip, i.e., zero velocity gradient, is present at the top of the boundary layer, as shown in Yamada *et al.* [62].

$$q_{\mathrm{m}} = \frac{\rho_{\mathrm{v}}(\rho_{\mathrm{l}} - \rho_{\mathrm{v}})\, g}{12\mu_{\mathrm{v}}} \left(\bar{\delta}_{\mathrm{m}}\right)^3, \tag{69}$$

where local layer thickness is replaced with the averaged one, computed as explained above.

The assumption of laminar flow inside the vapor layer may be approved with calculation of Reynolds number:

$$Re = \frac{\bar{w}\, d_{\mathrm{eqv}}}{\nu_{\mathrm{v}}}, \tag{70}$$

where $\bar{w}$ is the mean velocity of the vapor phase, m/s, d_{eqv} is the equivalent diameter, m, and ν_{v} is the vapor phase's kinematic viscosity, $\mathrm{m^2/s}$. The equivalent diameter is calculated as a difference between the outer diameter of the vapor film, i. e., $D_{\mathrm{v}} = d + 2\delta$, and diameter of cylinder, $d = 0{,}045$ m; or the equivalent diameter can be calculated as $d_{\mathrm{eqv}} = 4A/O = 2\delta$. This yields a value of 33.3, and thus confirms the accepted assumption of laminar flow inside the vapor film.

2.3.5 Additional remarks regarding the heat transfer during cooling of heated metal object

The volumetric absorption, and thus the emission, that originate from the presence of a three-atomic gas, i. e., the water vapor, H_2O, may have some content due to very high temperatures that are involved in this film boiling process. However, due to very small thickness of the vapor layer, discussed before, and presence of silver material, whose emissivity factor is quite low, i.e. 0.02 in a case of polished surface at 20 °C (in the normal direction) as per [63], the selective radiation of gases has been neglected in the present research. The presence of thermal radiation heat transfer in the context of three or more atomic gases is a volumetric phenomenon in contrast to solid surfaces and liquids, wherein the thermal radiation heat transfer is fully dependent on the conditions at the surface of the material. These gases, say, CO_2 and H_2O, emit thermal radiation in the spectrum of thermal radiation wavelengths that spans over several spectra, capturing thereby the infra-red thermal radiation. If, for example, a layer of such a gas (three or more atomic) is irradiated with a blackbody radiation, one may distinguish

there are three wavelength intervals whence these gases would exhibit the volumetric radiation properties; hence, this type of thermal radiation is called selective radiation, since it only occurs in several wavelength intervals, otherwise these gases are fully transparent to thermal rays, i. e., there are no absorption or emission that would take place in a gas medium. A detailed description of wavelength intervals in which CO_2 and H_2O participate with volumetric absorption and emission one may found in Galović [4], while the application of radiation model in a CFD framework is Krasniqi [64]; a computational study in which the author conducted combustion in a steam generator study using ANSYS Fluent.

2.3.6 Computational results

2.3.6.1 Temperature field

The temperature distribution in a solid specimen agrees well with the experimental data by Momoki *et al.* [1] in approximately ten percent of total film boiling period[4], as shown in Fig. 21.

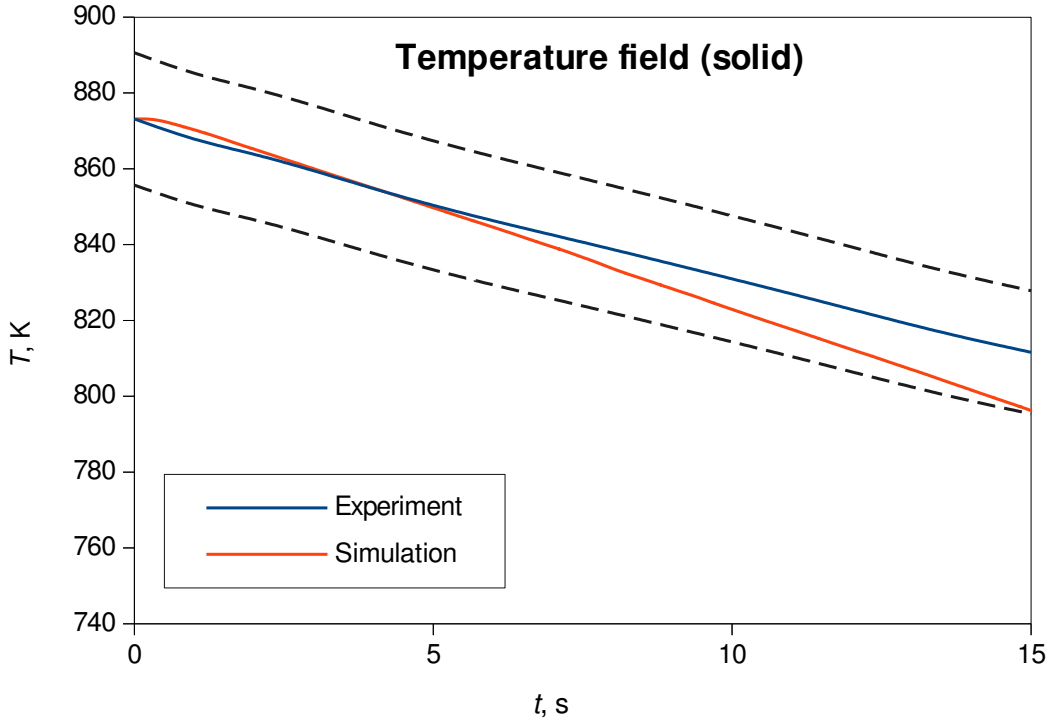


Fig. 21. The temperature evolution in a solid specimen during approximately first 15 s of the simulation; the data is compared to the experimental results from Momoki et al. [1]*, extracted using* [65]*. The dashed line denotes ± 2 % error band.*

4 The inflection point may be regarded as $t \sim 140$ s in [1], in the case of stable film boiling at the saturation temperature.

The experimental data is extracted from [1] using [65], and supplemented with ± 2 % error band, showing the accuracy of the method in the selected time period. The time shift is accomplished using Eq. (49), since there is no known analytical solution to Stefan problem in cylindrical coordinates, as outlined in Galović [66]; yet there is a quasi-steady approximate solution that is valid for low Stefan number, $Ste = c_p(T_w - T\text{-})/r_0$, that is, in the case of the low wall superheats.

2.3.6.2 Comparison of calculated heat transfer coefficients

The area weighted average heat transfer coefficients were extracted using the graphical-user interface; the data is stored approximately every 0.2 s. The calculated heat transfer coefficient, h, in the performed numerical simulation stems from the Newton's cooling law:

$$h = \frac{q_w}{T_w - T_\infty}, \tag{71}$$

where q_w is the heat flux at the specimen wall, T_w and T_∞ are the wall and free stream temperature, respectively. The area-weighted heat transfer coefficient is extracted from the graphical user interface (GUI), considering thereby the heat transfer rates at bottom, top and vertical (circumferential) surface of the cylinder; that is, the overall heat transfer coefficient is taken into account; instead of separate, per-surface heat transfer.

The analytical solution to average overall heat transfer coefficient is presented in Momoki *et al.* [1] and reads:

$$\bar{h} = \left[\frac{\bar{h}_A + 4\{\bar{h}_{B1} L_{B1} + \bar{h}_{B2}(L - L_{B1})\}/D + \bar{h}_C}{2 + 4(L/D)} \right], \tag{72}$$

where $\bar{h}_A$ and $\bar{h}_C$ are, respectively, the average heat transfer coefficient at the bottom and top horizontal surface of the cylinder; $\bar{h}_{B1}$ and $\bar{h}_{B2}$ are the heat transfer coefficients at the vertical surface in the region of smooth and wavy vapor-liquid interfaces, respectively, whilst L and L_{B1} denote the total and smooth interface length, respectively; D is the diameter of the

cylinder. In their study, the authors impose the ± 15 % error bandwidth on the. Hence, we will stick here to the value obtained using the Eq. (72), and the result is shown in Fig. 22.

In the formulae for average heat transfer coefficient during film boiling around a finite length cylinder specimen, Eq. (72), the contributions from each heat transfer surface via its own heat transfer coefficient noted above, the vapor phase is considered and superheated and thus the thermal properties of the vapor phase were taken for mean temperature, $\vartheta_m = (\vartheta_w + \vartheta')/2$, from [63] using the linear interpolation technique, and are listed in Table 11.

Table 11. The thermal properties of superheated vapor used in estimation of film boiling heat transfer coefficient at the temperature 350 °C.

Phase	ρ , kg/m^3	c_p, kJ/(kg K)	λ, W/(m K)	Pr, -
Vapor	0.3484	2.0396	0.040475	0.9137

The liquid (water) is considered as saturated, hence among the thermal properties of the water, only the density is used, ρ_l = 958.41 kg/m^3, also taken from [63].

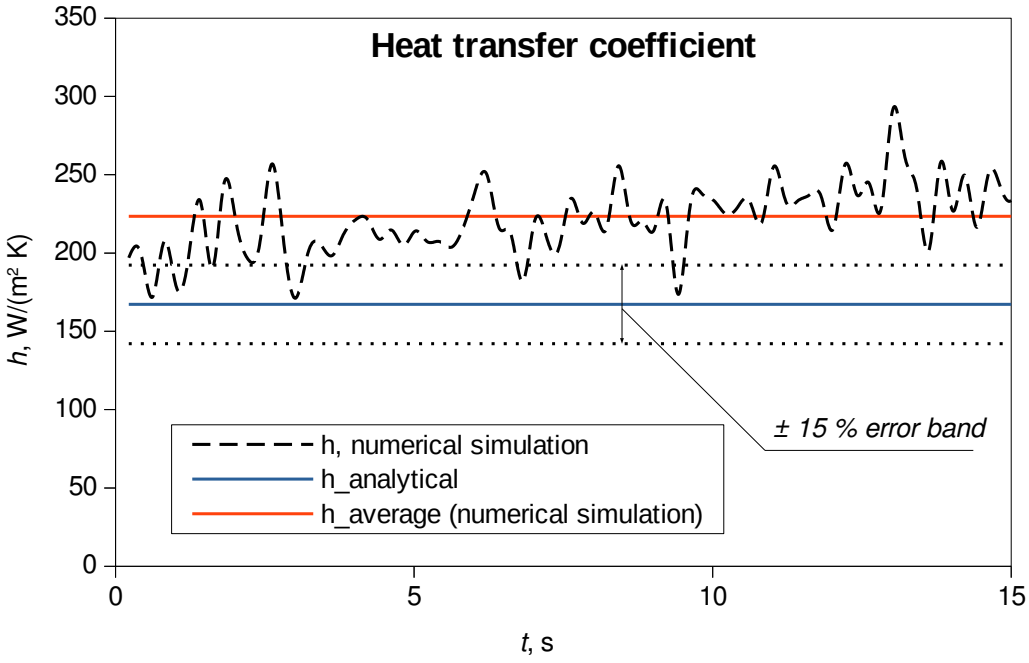


Fig. 22. The calculated heat transfer coefficients using numerical simulation in comparison to ones obtained using Eq. (72).

The discrepancy is found to be slightly more than 30 % in the present numerical simulation. The average heat transfer coefficient from the numerical simulation is calculated as:

$$\bar{h}_{\text{simul.}} = \frac{\sum h_i \Delta t_i}{t_{\text{total}}}, \tag{73}$$

where, $\bar{h}_{\text{simul.}}$ refers to a calculated heat transfer coefficient using numerical simulation, Δt_i is the time segment for which the heat transfer coefficient is taken from GUI, and t_{total} is the total simulation time, say,15 s.

In Fig. 22 one can observe the cyclic behavior of the heat transfer coefficient. This is due to cyclic behavior of the vapor-liquid interface during the film boiling process, that has been also noted in study by Tsui *et al.* [67]. The heat transfer coefficient, obtained via the numerical simulation, enters the upper limit of the error band, that is 15 %, prescribed by the authors of the correlation.

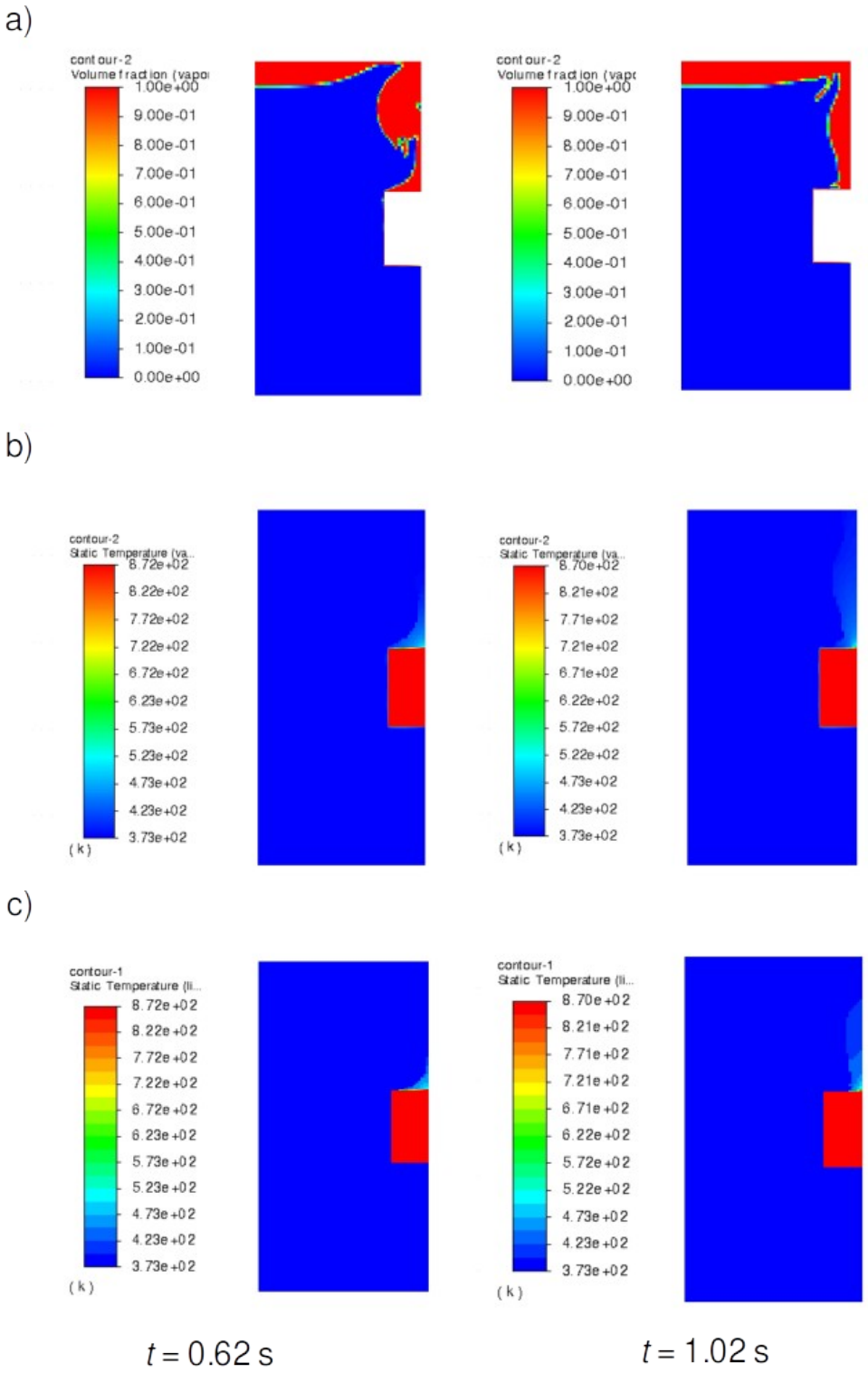


Fig. 23. Transient behavior of: (a) vapor film; (b) temperature evolution in the vapor phase; (c) temperature evolution in the liquid phase.

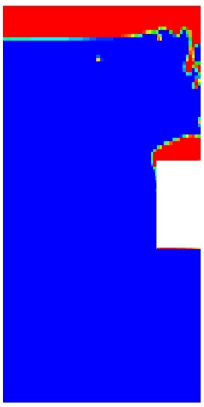
The vapor evolves from the top horizontal surface and is being advected due to buoyancy to the free surface of water, as shown in Fig. 23; forming thereby the vapor jet, as observed also in

other studies. Similar flow patterns were observed with photographic study in Tsui *et al. [67]* and Jurić and Tryggvason [68]; both being calculated for film boiling on a horizontal surface.

The temperature field, on the other hand, exhibits slightly overheating above the top of the cylinder, while being uniform elsewhere. The superheats may be found as comparable, at least quantitatively, to those in the film boiling study by Sato and Ničeno [21]. The uniform temperature distribution in a solid is due to its small Biot number and, therefore, inexistence of spatial temperature gradients in a solid. Since the vapor temperature doesn't differ significantly from the liquid temperature, the latter would be studied any further in this text.

An analysis of a single bubble using Newton's second law, that is, the momentum conservation equation, shows how the bubble shape is influenced by inertia, buoyancy, viscous and surface tension forces. The study by Yamada [69] reveals the true behavior during film boiling of a cylinder specimen studied here, but with different dimensions. It is rather difficult to make a direct comparison with the experimental observation, but at least qualitatively one may obey similarity between the performed simulation and the experiment that is conducted using silver specimen of similar dimensions and wall superheat.

Table 12. Joint comparison of experimental and the flow fields (volume fraction) obtained with usage of numerical simulation.

Quantity	Simulation; 45 × 45 mm	Experiment [69]; 32 × 32 mm
Flow field		
t, s	10.22	15
ΔT_w, K	444,9	~345

In Table 12, a comparison of the flow fields obtained in the numerical simulation and the one in experiment is made. The influence of surface tension is in the tendency to minimize the contact area between the bulk fluid and a vapor phase, i. e., the surface tension force acts on the vapor, and tends to minimize the shape of vapor bubble.

2.3.6.3 The justification of the applied turbulent kinetic energy value

The effective thermal conductivity in a liquid phase, as outlined before, has been found to be crucial in appropriate modeling of heat extraction from a solid specimen. Hence, since the molecular thermal conductivity of the liquid phase remains constant thorough the computation, one should affect the turbulent part of the effective thermal conductivity; which, on the other hand, is a function of a turbulent viscosity since the turbulent Prandtl number is assumed as constant. The turbulent viscosity, from the viewpoint of truly relevant dependent variables, is a function of turbulent kinetic energy, although there is also a coefficient C_μ, that in the case of the selected two-equation turbulence model is a variable, that is, it has not its default value 0.09 as in standard and RNG instances of the model. However, we will now focus on turbulent kinetic energy as the key parameter in turbulence modeling; similar has been also pointed out in thesis by Subhash [30]. Within the framework of the present work, the TKE value has been obtained using a parametric investigation. A parametric study has been carried out in order to determine the TKE value for which the temperature evolution would agree with the experimental result. In this case it was 0.25 m^2/s^2. This value, however, may be obtained from Eq. (65) if the velocity input is taken from numerical simulation; the volume-weighted average velocity magnitude field of the vapor phase in the boundary layer in vicinity of the vertical surface of the cylinder. In doing so, the one-cell boundary layer thickness may be found as appropriate since the two-fluid model is used, and the mesh resolution does not play an important role in obtaining the accurate solution, as shown in early mentioned study by Gauss *et al.* [70]. In addition, the usage of fine mesh resolution is regarded as inappropriate in the framework of Euler-Eulerian modeling, as noted in the study by Pointer and Liu [45]. Fig. 24 compares the calculated TKE values using Eq. (64) and the one obtained with parametric study and used in this validation case.

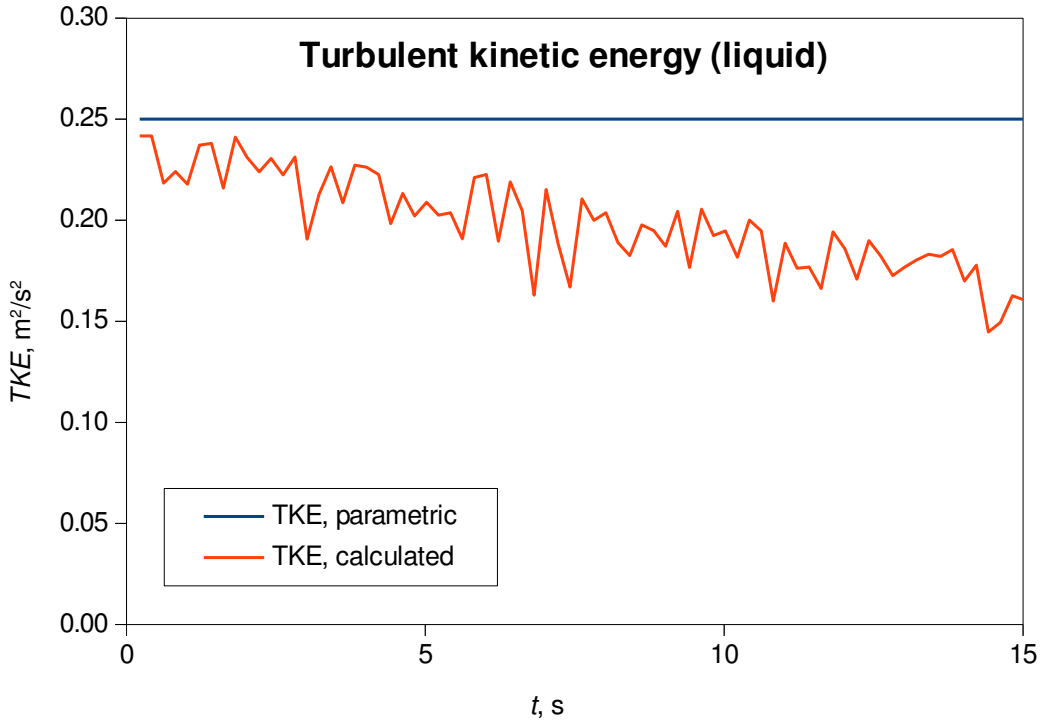


Fig. 24. The comparison of the applied, constant, TKE value obtained using a parametric study and calculated ones using Eq. (64).

It is, however, obvious that the applied TKE value obtained using the parametric investigation is slightly overestimated in the very beginning of the film boiling process (first 5 s of the process), whilst being completely overestimated in the later section of the process; when compared to calculated values using Eq. (64).

This range of TKE values, say, ~ 0.15 m^2/s^2 to ~ 0.25 m^2/s^2, could be related to the studies that follow. The study by Kashima *et al.* [55] brings us the study from Svendsen (1987), in whose model, if the TKE values in the range from 0.05 m^2/s^2 to 0.15 m^2/s^2 are used together with a certain turbulent length scale, one may obey the energy dissipation rate, in the context of breaking surf zone wave analysis.

It is interesting to note that these values coincide with the TKE values obtained in instability of a stable vapor flow study presented in Zimmer and Bolotnov [72]. In their study, the authors found 0.15 m^2/s^2 value of TKE as the threshold value in causing the instability of the stable slug flow. Also, the authors have proposed the correlation for which average value of TKE the instability may occur. Furthermore, these findings, obtained in the present research, are in close correspondence with the TKE value obtained in an analysis of a single jet flow in Kimber [52],

wherein a 0.2 m^2/s^2 is obtained slightly beneath the jet core. On the other hand, the TKE value of 0.25 m^2/s^2 has been chosen as the highest TKE input value in the simulation of dispersed two-phase flow using LES method in the context of atmospheric turbulent boundary layer modeling in Vinković *et al*. [73]. Furthermore, a study on jet flow in an indoor environment, presented in Heschl *et al*. [74], has also shown similar order of magnitude of TKE values in

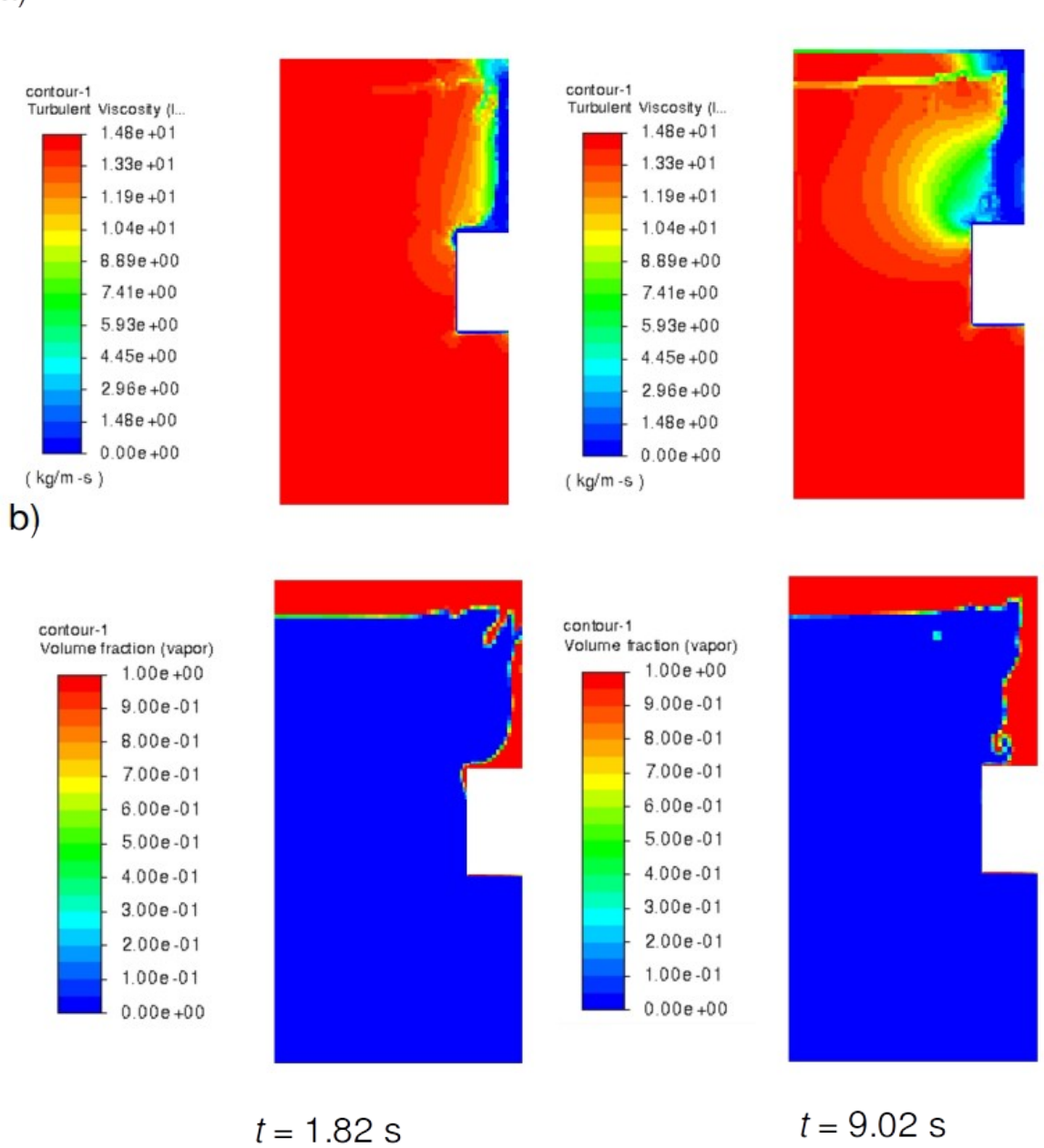


Fig. 25. The turbulent viscosity (a) and volume fraction (b) field for two different time instances in the conducted simulation of film boiling around a vertical cylinder in a saturated liquid medium.

downstream[5] region of a wall jet[6], that are successfully captured using the experimentally calibrated nonlinear model proposed by the authors.

Contrasting the temperature field in a solid specimen (Fig. 21) with the calculated TKE values may reveal that the constant TKE value resulted in too strong cooling after initial say 5 s of the process; yet the variable TKE value should be considered in further studies.

The visual observation of turbulent viscosity and corresponding vapor volume fraction fields shown in Fig. 25., reveals how the former closely follow the pattern of the latter. This may be addressed to the selected mode of the applied turbulence model, i. e., the dispersed mode, wherein the turbulence is being modeled only in the continuous phase, whilst Tchen correlation has been used in the dispersed phase. In addition to this, there is also a changeable turbulent viscosity coefficient, C_μ, that is present in the selected, although not solved, turbulence model. This may be found relevant in obtaining the turbulent viscosity adjacent to the interface, in the liquid phase; the transition values from zero to a constant value that is in the bulk, since the k is assumed as a constant. Hence, it is obvious that a laminar flow is concerned within the vapor phase, implying the existence of the BIT in the performed numerical simulation. Speaking in terms of analogy with a turbulent jet flow, the Realizable k-epsilon turbulence model is recommended for such flows.

2.3.6.4 The C_μ coefficient – a short discussion

In the present case, the C_μ is a function of strain rate, that is, the non-diagonal elements of a strain rate tensor (momentum equation) that can be found in standard continuum mechanics or fluid mechanics textbooks and reads [75]:

$$\varepsilon_{ij} = \frac{1}{2}\left(\frac{\partial u_i}{\partial x_i} + \frac{\partial u_j}{\partial x_j}\right), \tag{74}$$

where i and j are indexes of spatial coordinates in index notation (i, j = 1, 2, 3; meaning: x-, y- and z-coordinate), with u as the fluid velocity in the i-th direction, and correspond to tangential

5 At a location x = 0.6 m.
6 The jet that is issued from the orificie slightly beneath the floor of a room and, under the difference of static pressures, is attached to the wall; also known as Coanda effect.

stresses (friction). Hence, the distribution of the turbulent viscosity exhibits the pattern shown before in Fig. 25; it experiences smooth transition in the areas in the liquid that are occupied with a vapor-liquid interface. This friction is further transferred into the liquid in nearby zone to the interface between the phases. Once more, we prove, at least quantitatively, the necessity of the application of such an instance of the selected turbulence model (realizable) in modeling such a phenomenon (film boiling).

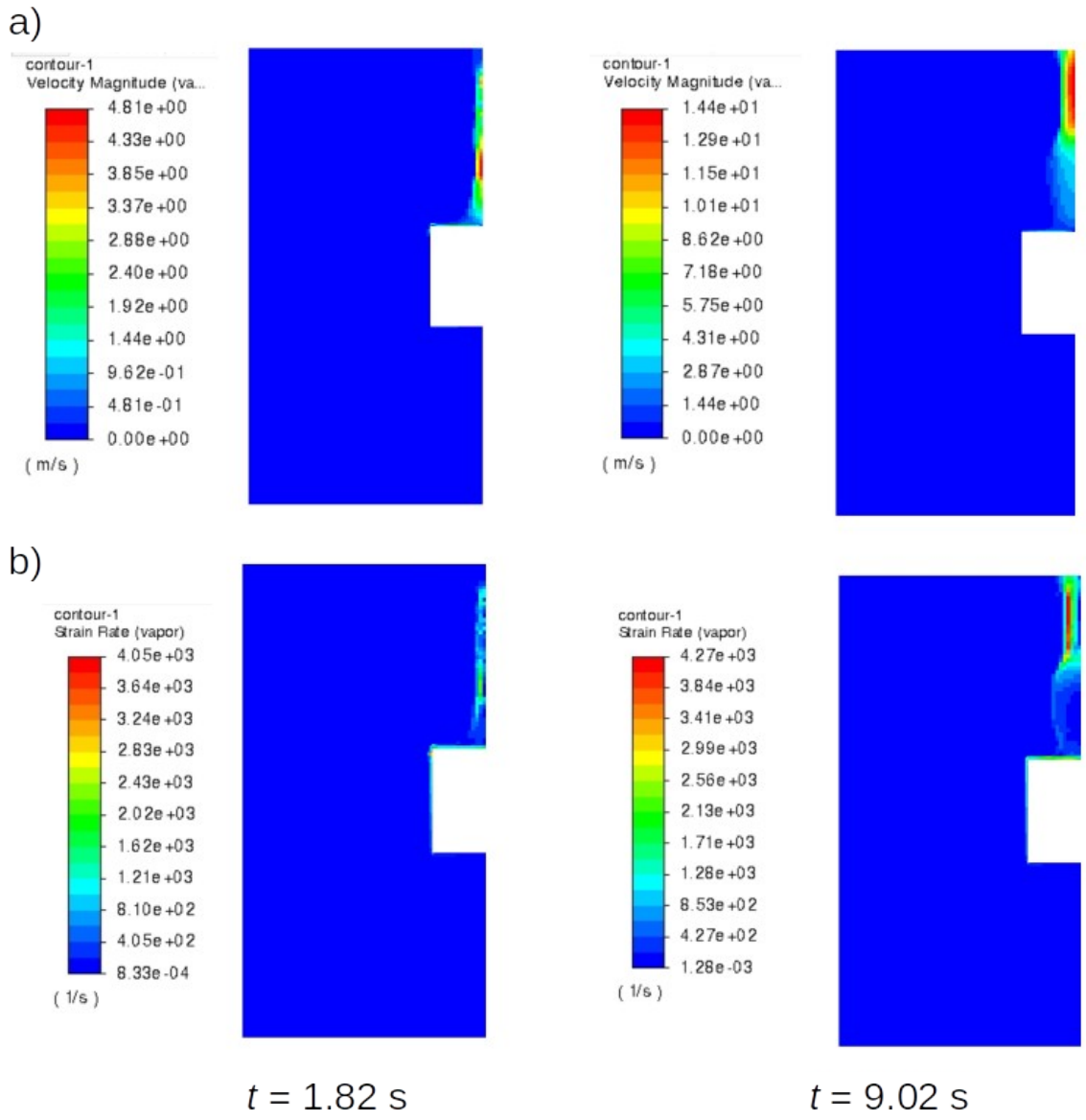


Fig. 26. A view on vapor phase's velocity magnitude (a) and strain rate (b) distrubutions; the strain rate follows closely the interface shape, thus featuring the presence of friction at the interface between the phases.

A joint view of velocity magnitude of the vapor phase and its strain rate shows how the friction is about to occur at the interface nearby zone, say, the “shear layer” in the context of the turbulent jet flow, Fig. 26, where velocity gradients are the highest. A discussion on application of this model in the context of jet flow in a confined space in available in Heschl [76].

2.4 Conclusion of Chapter 2

In this chapter, a novel method calculating mass transfer for two-phase flows with phase change has been proposed. The method is based on a two-fluid VOF formulation, and involves two asymptotic-like behaviors, i. e., the equality of the velocities and temperatures of the involved phases at the interface; thus, mimicking the pure VOF calculation. The method is verified using an analytical solution to Stefan problem, using thereby the computational meshes of three different cell types, namely: quadrilateral, stretched and hybrid cell type meshes. Furthermore, the method is validated using the experimental data for pool film boiling during cooling of a silver specimen, available in Momoki *et al*. [1]. To accomplish this, a zero-equation like turbulence modeling approach has been found appropriate; in addition to the proposed mass transfer model. Thus, all the prerequisites for conduction of a real quenching case that is industrially relevant have been completed and are subject of the following chapter.

3 NUMERICAL SIMULATION OF METAL MATERIAL QUENCHING

3.1 Introduction

The main goal of this thesis, i. e., the numerical simulation of metal material quenching using immersion technique is carried out in this chapter. Hence, a computational model that is able to estimate the temperature distribution inside a solid specimen during film boiling phase of immersion quenching process has been presented in the following subsections, based on the prescribed initial temperatures of the solid specimen and the liquid quenchant. In addition, the turbulence effects have to be considered using the assumed turbulence kinetic energy value, that remains constant thorough the simulation. The studied material is nickel alloy Inconel 600, for which the extensive experimental data is available, since it is part of ISO 9950 and ASTM 6200 standard. This material, however, exhibits significant change with temperature in specific heat capacity and thermal conductivity that has to be taken into account; but also, the material is no longer immersed in the liquid medium from the very beginning of the simulation process; yet it has to be immersed during the simulation run.

First of all, we need to distinguish between two types of interfaces that are present during the water entry of a heated cylinder: the free surface and the interface. The free surface of water relates to a large scale interface between two bulk mediums; whilst the interface is designated as the surface between the two phases in a phases change process, that is, between the vapor phase, generated in boiling process, and a bulk liquid phase. The chapter starts with the concise review of the relevant studies that primarily deal with the isothermal multiphase flow or thermal phenomena in the solid phase; since this study is aimed on thermal interaction between the fluid and a solid phase, these studies were omitted in the literature review presented in the introductory chapter. In the remainder of the chapter, a concise exposition of the setup underlying this simulation is presented. The chapter closure, located at the end, summarized the important features of the simulation conducted herein.

3.2 Related studies

3.2.1 Water entry

In naval hydrodynamic, the water entry is an interesting phenomenon from the viewpoint of investigation of hydrodynamic loads on floating bodies when they are being immersed into liquid medium. These studies usually focus on wedge-like objects, spheres and horizontal cylinders. The analytical solutions from Wagner and Von Kármán exist to this end; both being presented in PhD thesis from Toso [77]. In numerical simulation of such a phenomena, two distinct approaches may be found with respect of the way the body is immersed: a free fall, and a constant velocity drop-down; both approaches being applied in Kleefsmann *et al.* [78], whilst the latter has been, although in a fully Lagrangian manner, solved in Bašić *et al. [79]*. Within the studies focused on free fall, further two modeling approaches are used in regard of computation of drop-down velocity, i. e., from accounting the forces that act on a falling body: the 6-DOF (degrees of freedom, DOF) and the computation of velocity upon a previous time step.

Apart from the aforementioned isothermal water entry studies, we shall outline the studies with immersion of heated solids into liquid mediums. To this end, in a study by Li *et al.* [80], the stability of vapor-liquid interface was studied for different degrees of subcooling and/or wall superheats. Still being in the context of naval hydrodynamics is the application of so-called air lubrication systems (ALS), but using water vapor as a medium instead of air bubbles. In that sense is the study by Jetly *et al.* [81], wherein the influence of vapor film formation around a sphere on flow hydrodynamics was examined during water entry of heated sphere in a liquid FC-72 medium using experimental investigation. The influence of Leidenfrost effect within the framework of water entry, i. e., the formation of vapor blanked around a spherical body on flow enhancement during immersion of a heated sphere in liquid, has been discussed from theoretical point of view in Gylys *et al.* [82]. The authors evaluated the energy consumption required in realization of such cases.

However, a study that encompass the water entry and immersion of a heated cylindrical body, investigating thereby also the temperature evolution inside the material (conjugate heat transfer, CHT) together with incorporating the phase change phenomena that occurs in the liquid phase,

using numerical simulation technique and basic principles approach, has not been found in the open literature.

3.2.2 Drag reduction

As noted before, the Leidenfrost phenomenon is also termed as a drag reduction method in the case of classical marine hydrodynamic example, that is, the water entry problem. Hence, apart from the classical industrial appearances of boiling processes, briefly shown in the introduction of the thesis, is the application of boiling flow in the field of naval architecture, where it can be addressed to, already well-established, air lubrication systems used in reduction of ship resistance; however, without involving the phase change process. From the numerical point of view, two distinct approaches may be found in the literature in this regard: the more fundamental ones, dealing with micro-bubble drag reduction (MBDR); and the macroscopic studies aimed to study the flow features around the bodies. An example of the former is the numerical simulation of an MBDR on a flat plate conducted using the two-fluid model in Mohanarangam *et al*. [83]. In the latter case, a scaled bulk carrier is a subject of the study by Sindagi *et al*. [84]. Using the single-fluid VOF method the ship resistance is obtained for two different ship speeds; different air injection rates and different diameters of the air injection holes.

3.2.3 Quenching

The inverse heat transfer analysis (IHTA) of Inconel 600 probe is presented in Felde [85]. Since only one temperature is measured, that is, at the center of the probe, only the heat transfer coefficient in the immediate vicinity of that axial point (at the radius of that axial point) may be obtained, $h_c(\mathbf{r}, T)$; where index c denotes the central point of a specimen, $\mathbf{r}$ is the position vector, and T is the absolute temperature in degrees Kelvin. The obtained heat transfer coefficient values may either compose steep and/or linear distribution. The linear distribution, also discussed in [5], is adopted in [85]. The inverse heat transfer analysis has been also used in a study by Demirel [86]. The author coupled the it with finite element method (FEM) in order to predict the temperature evolution in a solid material; it is clearly shown by the author how the heat transfer coefficient estimated by the IHTA refers to a specific, local, zone of the material in question.

An investigation on temperature-time distributions during quenching of a nickel Inconel 600 alloy has been reported in Landek *et al*. [2]. The authors, nevertheless, have shown the temperature and the heat transfer coefficient calculations using an analytical expression and inverse heat transfer analysis, respectively. Only the temperature in a geometric center of a probe was evaluated experimentally using a K type thermocouple; whilst the surface temperature has been calculated on a basis of transient heat conduction analytical model. Furthermore, two distinct approaches were used in estimation of temperature, and thus the time; distributions of the heat transfer coefficient; the one proposed by the authors, and the one obtained by the *ivfSmartQuench* system commercial software.

Speaking in terms of the aforementioned software, the *ivfSmartQuench* system, it is the standardized method for estimation of quenching power of liquids and is explained in more detail in Troell [87]. Furthermore, the fundamentals of inverse heat transfer analysis together with the examples in realistic quenching application using computational software is described by the authors.

Furthermore, in his PhD thesis, Landek [88], has studied the influence of thermal effusivity, $b=\sqrt{\rho c_s \lambda}$, a material ability to transfer the heat into surrounding medium; however, in the framework of the spray quenching processes. It was observed in PhD thesis from Tenzer [89], that the Leidenfrost temperature decreases with the increase in thermal effusivity, also within the context of spray quenching. A recent study by Jagga and Vanapalli [90] reveals how the standard boiling modes are only valid in the case of high thermal effusivity materials, whilst in the opposite situation this the materials may exhibit different behavior. Its value in calculation of Leidenfrost temperature in the case of forced convection film boiling has been reported in [91].

3.2.4 A brief summary on the related studies

As a main outcome of the present research is to establish a conjunction between the two presented approaches; that is, to encompass an immersion process (usually isothermal) with conjugate heat transfer study (usually without moving boundaries), incorporating thereby the phase change and turbulence phenomena that occur in the liquid phase. As can be concluded from the abovementioned studies that deal with the phenomena in solid, that is, the quenching studies, the heat transfer coefficient has been selected as an input parameter, determined using

previously conducted experiment and an inverse heat transfer analysis. Thus, a temperature field inside the material is obtained and can be supplemented to further analysis (stress and strain analysis).

However, the goal is to avoid any kind of experiment that needs to precede the investigation on the temperature distribution in a solid; that is, that the temperatures and heat transfer coefficient stem from the solution obtained using initial temperature of the solid and a quenchant medium. In order to do so, the following subsections present a novel approach that alleviates the experimental input and provide sufficiently accurate results.

3.3 Description of the experiment

The specimen is initially placed 170 mm above the free surface of water, and is manually immersed into the quenchant medium; a 0.13 m/s constant velocity translatory motion of specimen may be assumed in the model according to estimation in [92]. In doing so a steel rod is connected to the specimen's top horizontal surface. This steel rod has been neglected in the present numerical study for the sake of simplicity. The temperature is monitored in the central point of the specimen, i. e., 30 mm above the bottom surface; the specimen is made of Inconel 600 alloy and is 12.5 mm in diameter and 60 mm in high. The temperature acquisition starts when temperature at the measuring location reaches approximately 850 ^{o}C; the initial specimen temperature is taken as 855 ^{o}C. The immersion stops when the bottom surface of the specimen is 260 mm below the free surface of the water. The thermoelement is expected to register the radial temperature change before the axial one, due to small radial thickness in comparison to the axial one, i. e., the distance from the thermocouple to the cylinder bottom surface.

The snapshots of the solid specimen immersion quenching is shown in Fig. 27[7]. Please note that the studied specimen is heated to a predefined high temperature in a furnace, and then dipped down to a quiescent liquid that has been previously heated until the temperature of ca. 52 ^{o}C is reached. Please consider the vapor bubble formation beneath the horizontal bottom surface, and at the cylindrical surface of the specimen.

7 The author thanks to Professor Landek and Ms. Izabela Martinez for carrying out this experiment and reproducing the data.

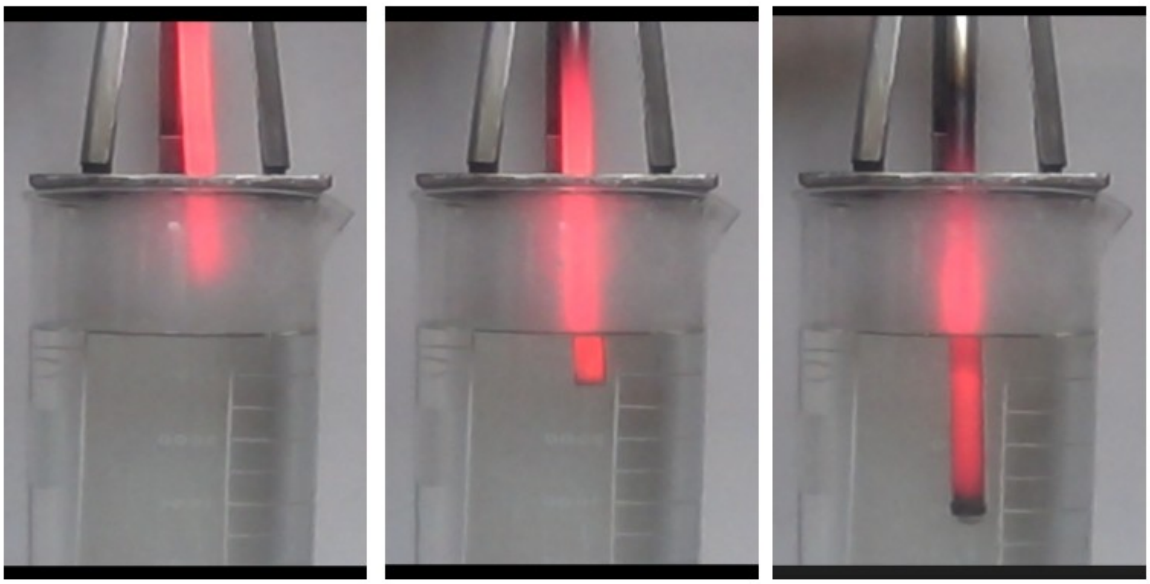


Fig. 27. The experimental investigation of Inconel 600 quenching in quescient liquid-water pool at initial temperature of ca. 52 °C: (a) immediately before the immersion; (b) after the top of the body has been immersed; (c) at later stage of the immersion quenching process.

Furthermore, it is noteworthy to identify the advancement of the temperature in a bottom-up fashion in the axial direction, and from the outer side to inner part of the body in the radial direction, thus featuring the existence of significant temperature gradients with respect to space in the solid object, i.e., the case with $Bi \rightarrow +\infty$.

3.4 Numerical method

3.4.1 Description of the case and geometry

3.4.1.1 An overview

The test case is designed as shown in Fig. 28. Two distinct fluid zones, namely vapor and a liquid zone, are present in the domain, together with one cell zone occupied by a solid. The computational domain is designed as an axis-symmetric and of dimensions 100 mm in radius and 960 mm in height, divided into two continua: fluid and a solid continuum; the fluid part thereby contains vapor and water medium, whilst the solid material is made of Inconel 600 alloy

and its material properties are discussed in the forthcoming section. The material properties of the liquid and a vapor phase are defined based on the interface temperature and are taken as listed in Table 2; hence, a thermal equilibrium is assumed at the interface, that is, the interface is kept at the saturation temperature due to macroscopic scale of the studied film boiling phenomena.

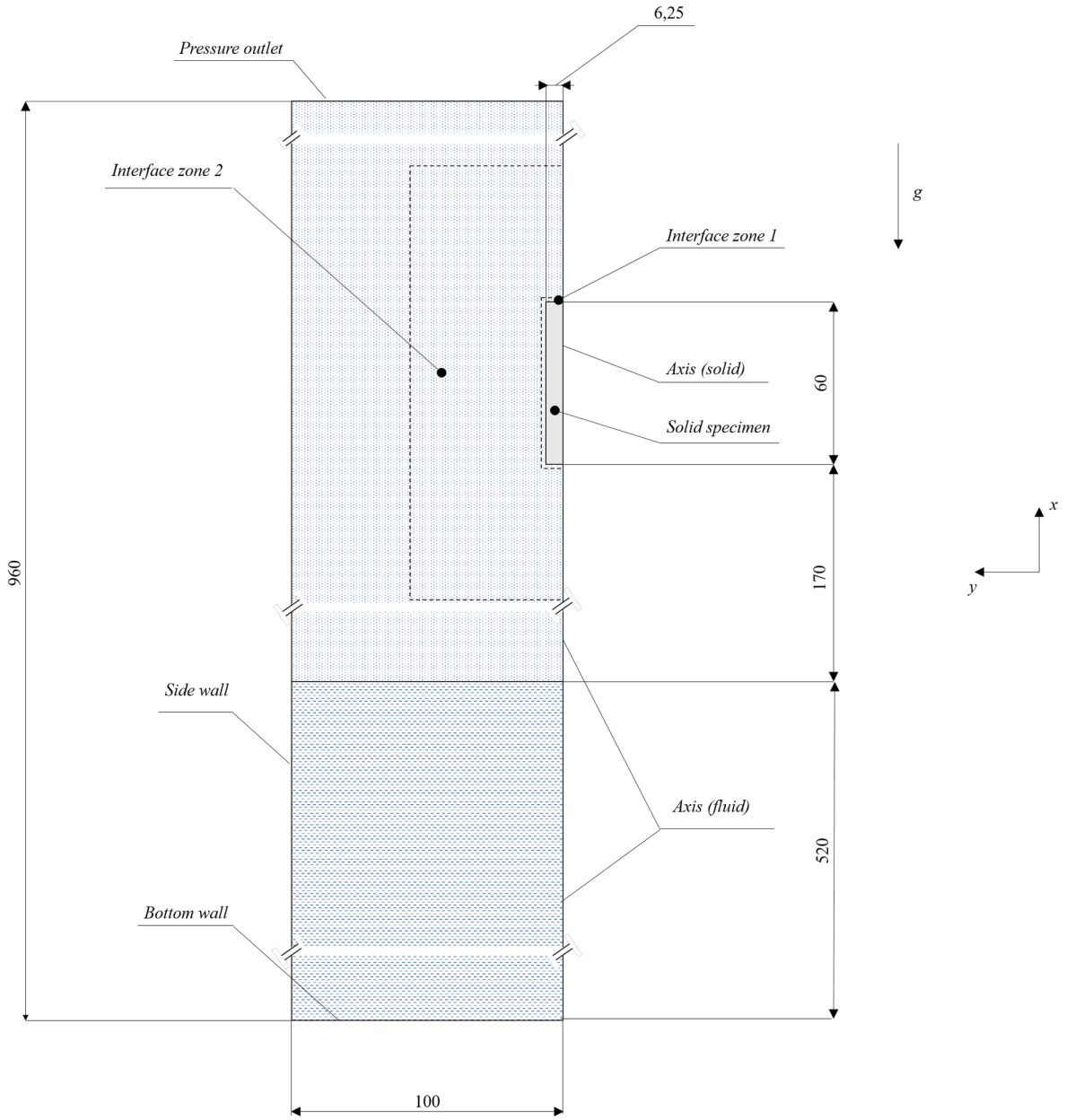


Fig. 28. An overview of the computational domain with selected boundary conditions; a "Coupled" prescribed boundary condition is ommited from the sketch for the sake of clarity. The dimensions are expressed in mm.

3.4.1.2 Material properties

The solid continuum is of dimensions 6,25 mm radius and 60 mm height, that occupies a zone on a symmetry axis as shown in Fig. 28. These physical properties, namely: density, ρ_s, thermal conductivity, λ_s, and specific heat capacity, c_s, assigned to the solid part are those of Inconel 600, nickel alloy used in the experiment from Landek *et al*. [2], and were taken from the properties listed in a book of Hännoschöck [93]; however, due to strong temperature dependence of thermal conductivity and the specific heat capacity, these values were approximated by a polynomial function. Hence, the material properties applied in the present study for a solid specimen read:

$$\lambda_s = 1{,}336\ \text{E-}10\ T^3 + 2{,}745\ \text{E-}6\ T^2 + 1{,}240\ \text{E-}02\ T + 1{,}087\text{E+}01; \tag{75}$$

$$c_s = -1{,}415\ \text{E-}09\ T^4 + 4{,}129\text{E-}06\ T^3 - 4{,}251\text{E-}3\ T^2 + 2{,}025\ T + 1{,}144\text{E+}2; \tag{76}$$

whilst the material density is taken as constant value, $\rho_s = 8470\,\text{kg/m}^3$, and with the temperatures, T, expressed in degrees Kelvin. However, this approach with approximation of the specimen thermal properties using a polynomial function has not been adopted in the present work; yet those are used in plots depicted in Figs. 29 and 30. The thermal effusivity is thus as depicted in Fig. 28, using the temperature dependent thermal conductivity and specific heat capacity according to Eqs. 75 and 76.

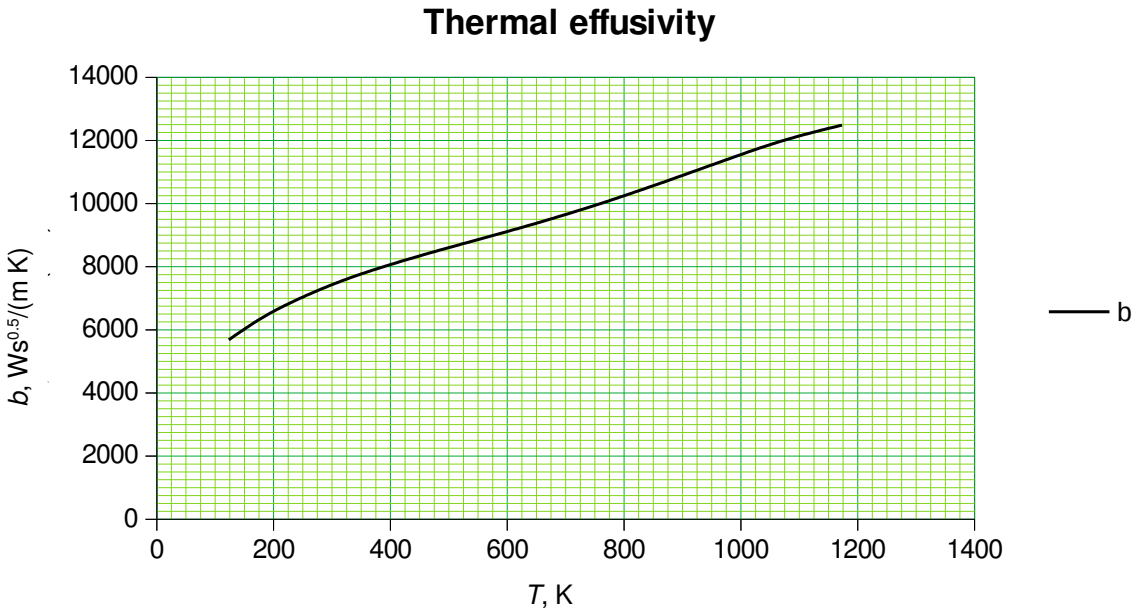


Fig. 29. Thermal effusivity of Inconel 600 with respect to temperature.

The relatively high values of the thermal effusivity indicate the standard boiling modes would occur during cooling of a high temperature object made of this material. The thermal diffusivity, defined as $a_s(T)=\lambda_s(T)/(\rho_s\ c_s(T))$, on the other hand, follows the pattern depicted below, Fig. 30, and is computed using Eqs. 75 and 76 together with a constant density input.

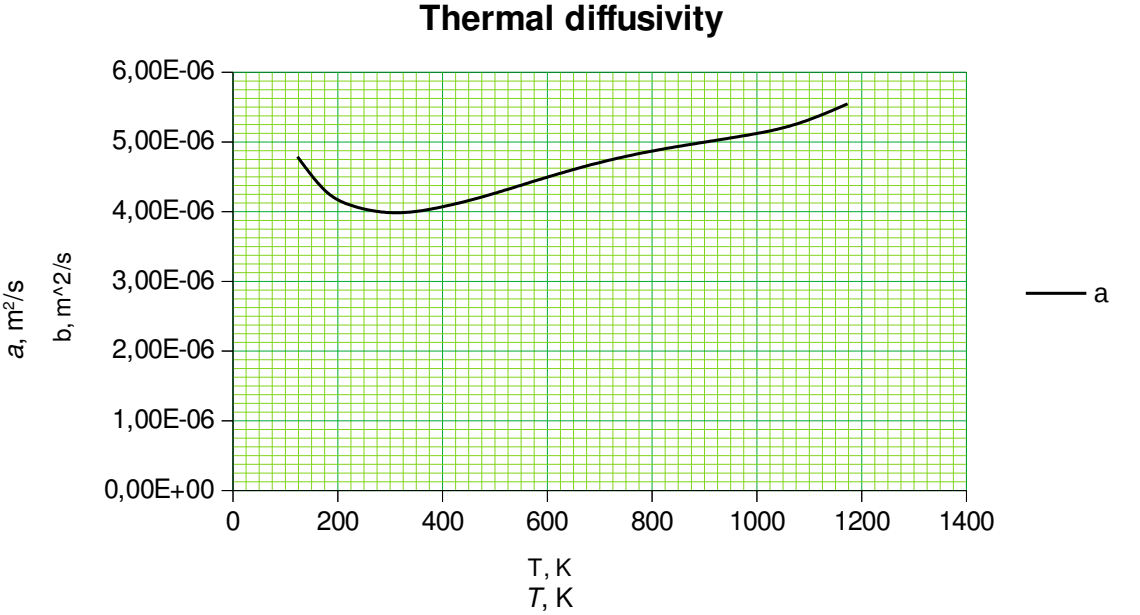


Fig. 30. Thermal diffusivity of the studied material.

The properties, λ_s and c_s, were in the performed numerical simulation, on the other hand, approximated using piecewise-linear segments according to data listed in [93]. Thus, four different points: 200 °C, 400 °C, 600 °C, and 800 °C, were taken for approximation of specific heat capacities; whilst five points were used in extraction of data for thermal conductivities: 200 °C, 400 °C, 600 °C, 800 °C, and 900 °C.

3.4.2 Initial and boundary conditions

The initial and boundary conditions closely follow the ones reported in validation section. However, some small changes have to be carried out since the mesh motion is present in the case and the liquid is not anymore at saturation temperature; it is in subcooled condition instead. Hence, the initial distributions of volume fraction (both liquid and vapor), TKE (liquid only) and temperature are imposed in the computational domain together with the zero-velocity field in a manner similar as before, using the Define-init user defined function. Fig. 28 depicts the initial vapor and liquid fields, i. e., the respective volume fraction distributions, while dashed lines outline the two interface zones; first one being as in the former case, used in order to induce the mass transfer and specify the laminar zone in an initial vapor layer, the so-called "Interface zone 1"; whilst the second one is used for turbulence modeling purposes, i. e., the TKE value, that may calculated by the procedure similar to those in validation part, is imposed only in these cells, the so-called "Interface zone 2". In order to prevent the occurrence of the mass transfer between two bulk phases, vapor and a liquid, the complete domain, with the exception of the specimen wall adjacent single cell layer, is set to 60 °C. Otherwise, due to existence of temperature and volume fraction gradient at the interface, a mass transfer would take place.

3.4.3 Moving boundary problem

As was noted before, the solid body is immersed using 130 mm/s velocity in the downward direction; thus, invoking the necessity to treat the problem as the moving boundary problem, since the specimen boundary changes its position with respect to certain part of the performed numerical simulation. This is accomplished via the "interface zone 2", shown in Fig. 27, which moves at a constant speed downward, embracing thereby all the subset zones: "interface zone 1", and the solid zone. The motion is established for initial ~2 s, that is

determined by the known distance that is to be passed by the bottom horizontal surface of the specimen. The forthcoming subsection provides more detail regarding modeling aspect in this regard.

3.4.4 Dynamic mesh handling

3.4.4.1 Mesh motion

In order to establish a linear translatory motion of a solid specimen, an arbitrary Lagrangian-Eulerian (ALE) scheme is used for establishment of the motion of the computational mesh in conjunction with the constant velocity in the downward direction and the remeshing technique. Hence, the governing equation for all the dependent variables in the case of mesh motion involves the velocity of the moving zone. Furthermore, in order the mesh motion to be valid, a geometric conservation law has to be fulfilled during mesh deformation. The pioneering study in this field is addressed to Noh [94], and the evolution of the approach has been concisely reviewed in dipping study by Aubram [95].

3.4.4.2 Remeshing

The computational mesh is being deformed under motion of the solid body and its adjacent zone, and the computational cells that are not selected to be fixed, in this case the significant part of triangular cells, are exposed to topological change[8]; i. e., they are being replaced with new ones, whilst the solution is interpolated from the past mesh. The solid body is moving together with its nearby zone, whilst the remainder of the domain is exposed to a deformation and/or remeshing, that is, the generation of novel cells after the specific mesh criteria are met. To accomplish this, a triangular mesh zone is defined outside the „Interface zone 2", wherein a topological change is adopted. Regarding the settings that are to be applied, ANSYS Fluent has an option to adjust them to the mesh, by a simple procedure. Apart from the usage of ALE solvers in the area of surface tracking, wherein the interface shape is a consequence of flow conditions, such as in, for example, some bubble dynamics with explicit interface definition via a one dimension lower mesh (line in 2D or surface in 3D), here the

8 The topological change can be refered to as the fact that one cell may not have the same neighbors thorugh the simulation; that is, the cell connectivity is being changed.

interface defined via a computational mesh remains constant. An application of remeshing within the scope of ALE solvers may be found in Dobrzynski [64].

3.4.5 Computational mesh

As stated above, the hybrid mesh composed of both, the triangular and quadrilateral cells is used in the present numerical simulation, as depicted in Fig. 31.

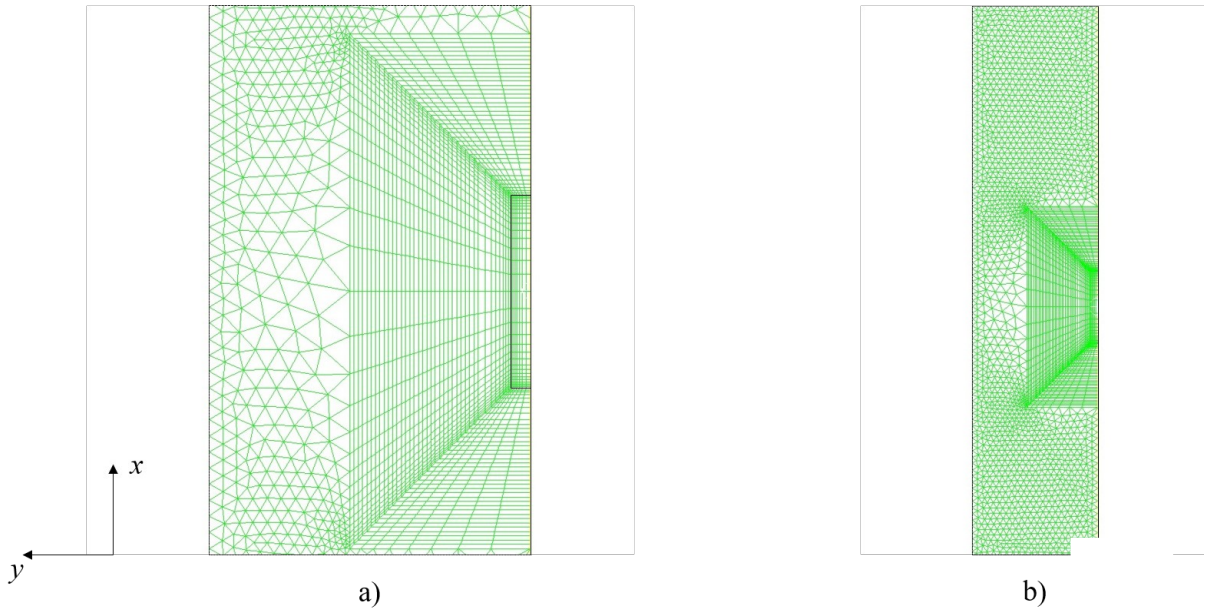


Fig. 31. A view on computational mesh: (a) the area in the vicinity of the specimen; (b) a broader view.

The computational mesh is composed of 254 cells that consist the solid part, contributing to in total 10354 cells that compose the whole computational mesh. This mesh size is not constant during the computation; yet it is increased due to remeshing procedure. The mesh is designed as a hybrid mesh, since it is composed of both, the isotropic triangular and quadrilateral finite volumes. The usage of triangular cells in now mandatory due to remeshing technique that is used for immersion of a solid object into liquid medium. The nicely places triangles may be

addressed to application of Delaunay triangulation method[9,10]. The nearby zone to a solid specimen is consisted of quadrilateral cells in order to preserve accuracy.

3.4.6 Turbulence modeling

In the former subsection it has been outlined that the turbulence kinetic energy is specified in the region outside the near wall adjacent zone consisted of one-cell layer, that may be denoted as „interface region 1", but being thereby limited in the outer region with the boundary of „interface region 2" according to Fig. 32.

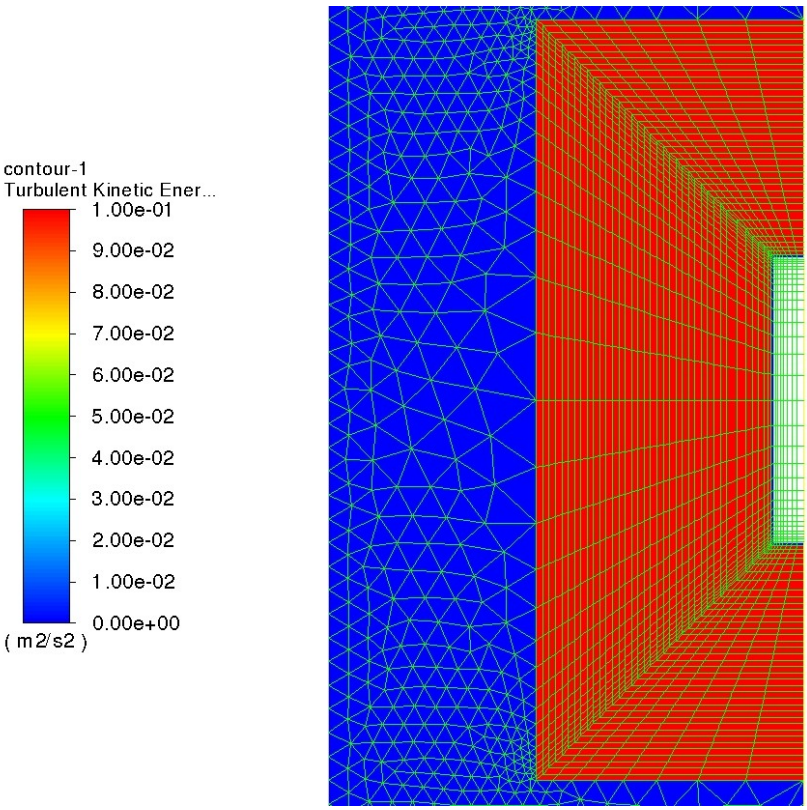


Fig. 32. The initial TKE distribution in the analysed case.

The turbulence kinetic energy levels in the case of pool film boiling may be found to be similar ti ones in the case of wave flow, according to results obtained in the preceding chapter; a

9 In Delaunay triangulation method each triangle in the triangulation of a surface is constructed in a such way that his points, when beeing connected with a circumcircle, contain no points from other triangles; see e. g. in [97] for detailed description.

10 The Delaunay triangulation method is also one of three main automatic mesh generation methods; other two are the octree and the advancig front method. However, when used in the context of automatic mesh generation, the method requires to be supplemented with input of points. A concise introduction to the topic of automatic mesh generation may be found in the introduction of thesis [98].

detailed Smoothed Particle Hydrodynamics (SPH) case of the wave flow is given in Makris *et al.* [57]; whilst the former (TKE values in pool film boiling studied herein) has been obtained merely using a parametric study, that was lately justified with a computational model, the latter (field TKE distributions) were confirmed with a detailed numerical simulations.

Further theoretical treatises are needed in order to obtain a more comprehensive approach in further modeling of TKE. A study by Takamatsu *et al.* [99] deals with stability analysis of the vapor film thickness in the case of subcooled film boiling around a horizontal wire. The authors, however, note the research by Tanaku wherein the study of subcooled boiling has been tackled using Taylor instability theory. Hence, further theoretical treatises on this subject are needed in order to make some judgments on turbulence modeling in the case of subcooled film boiling around a cylinder.

3.4.7 Solution procedure

Firstly, ten iterations with very small time step were used for initialization. A stabilized bi-conjugate gradient method was switched in order to establish a stable computation; this has been addressed in the documentation as a stability measure in the case of convergence problems. It is noteworthy that, after the initialization has been carried out, the interpolation method is changed from the default least squares cell based to Green-Gauss node based, according to recommendation in the official documentation regarding the computations that involve triangular and/or tetrahedral meshes. The dipping of a solid specimen has been solved predominantly using 1e-4 s. The temperature is limited to a lower-level value of 333.15 K, thus mimicking the Newton-Raphson numerical nonlinear equation system solution method, wherein a solution interval need to be assumed [100]. This is due to some unphysical temperatures below the minimum temperature that were observed in the simulation.

3.5 The heat transfer coefficient

The procedure for determination of overall heat transfer coefficient in the case of subcooled film boiling of a cylinder specimen is shown in Momoki *et al.* [1]. As in the case of film boiling in a liquid at saturation temperature, the calculation of heat transfer is divided into four sectors again, namely: the downward facing horizontal surface; vertical surface with smooth

and wavy interface between the phases; and a horizontal top surface. Thus, the overall heat transfer coefficient is again calculated using Eq. (72). However, it now refers to subcooled condition, since the inputs h_A, h_B and h_C now incorporate the correlations for subcooled liquid pool boiling, and are constituted from saturated part multiplied by the subcooled constant; the full description of the model equations in given in [1][11]. As is the case of superheated vapor, that we had to, as in the case of Nusselt film condensation model, take the thermal properties of the unsaturated phase are for some average temperature[12], $\vartheta_m = (\vartheta_w + \vartheta')/2$, in the case of superheated vapor; $\vartheta_m = (\vartheta' + \vartheta_b)/2$, on the liquid side of the vapor-liquid interface. Both using the data available in [63].

Table 13. Thermal properties of water and vapor at atmospheric pressure.

Phase	ρ , kg/m^3	c_p, kJ/(kg K)	λ, W/(m K)	μ, Pa s	Pr, -
Water, 60 °C	983.2	4.183	0.654	4.664E-04	2.981
Water, 80 °C	971.8	4.196	0.670	3.543E-04	2.219
Vapor, 477.5 °C	0,289	2,120	0.0642	2,766E-05	0.914

Since the liquid medium is now subcooled, we expect more intensive heat transfer. The expressions for estimation of the heat transfer coefficient now also encompass the phenomena associated with the existence of a liquid layer in which the temperature varies from saturation to the bulk fluid temperature, from a theoretical observation.

3.6 Conclusion of Chapter 3

In this chapter, the numerical simulation setup required for calculation of temperature field in a solid specimen during film boiling phase of immersion quenching process has been carried out. The context of this immersion process may be inherited from naval hydrodynamics

11 The correlations for subcooled film boiling of a finite length vertical cylinder may also be found in other publications from this group, namely Yamada *et al.* [101] and Yamada *et al*. [102], and a PhD thesis by Yamada [69].

12 As discussed in Galović [4] this temperature should be, ideally, considered as the one that would be achieved if the phases are perfectly mixed in an adiabatic system. Thus, this temperature would read:

$$\vartheta_b = \frac{\int_A \rho c_p w(A) \vartheta(A) dA}{\int_A \rho c_p w(A) dA}, \tag{77}$$

which , in turn, would require the knowledge of the cross-sectional velocity and temperature profiles in a cross-section. Since this is difficult to achieve, the temperature is calculated as an arithmetic mean value.

application within the framework of water entry problems, in the sense that a cylinder water entry has been studied first. Additionally, this case, among others, involves also heat and mass transfer in contrary to the classical water entry problem, in conjunction with CHT.

The test case has been designed similarly to the one in the validation part of the thesis, which an exception that now the solid specimen is initially placed in the vapor medium, instead of liquid as in the former case, and is immersed into the liquid medium using a moving mesh technique that involves remeshing. Hence, the computational mesh is consisted of two separate zones, namely, the moving one, composed of primarily quadrilateral cells (stretched), and a stationary one, discretized with triangular cells that is subjected to remeshing technique during the motion of the moving zone.

The selected material is Inconel 600 nickel-based alloy, with a thermocouple placed in the center of the object, for which the temperature data obtained using experiment is available. Furthermore, the material experiences significant change in thermal conductivity and the specific heat capacity with the temperature, that needs to be considered in the calculation due to its impact on the temperature evolution in the solid medium. Furthermore, the initial and boundary conditions closely follow, to a great extent, the principles outlined in the validation part of the thesis, excluding thereby the estimation of the initial vapor blanket's edge temperature, that is now handled automatically since the cell arrangement in the immediate neighborhood of the solid specimen is now changed. The computational results obtained with the described setup are presented in the following chapter.

4 RESULTS

4.1 Temperature distribution

The temperatures were sampled in a vicinity of a specimen's center, a volume-weighted average value in two cells in the immediate neighborhood of the specimen center was used due to mesh motion, i. e., the axial coordinate of a specimen's cell center is being changed thorough the simulation, in particular during the immersion process, say, the initial ~ 2 s.

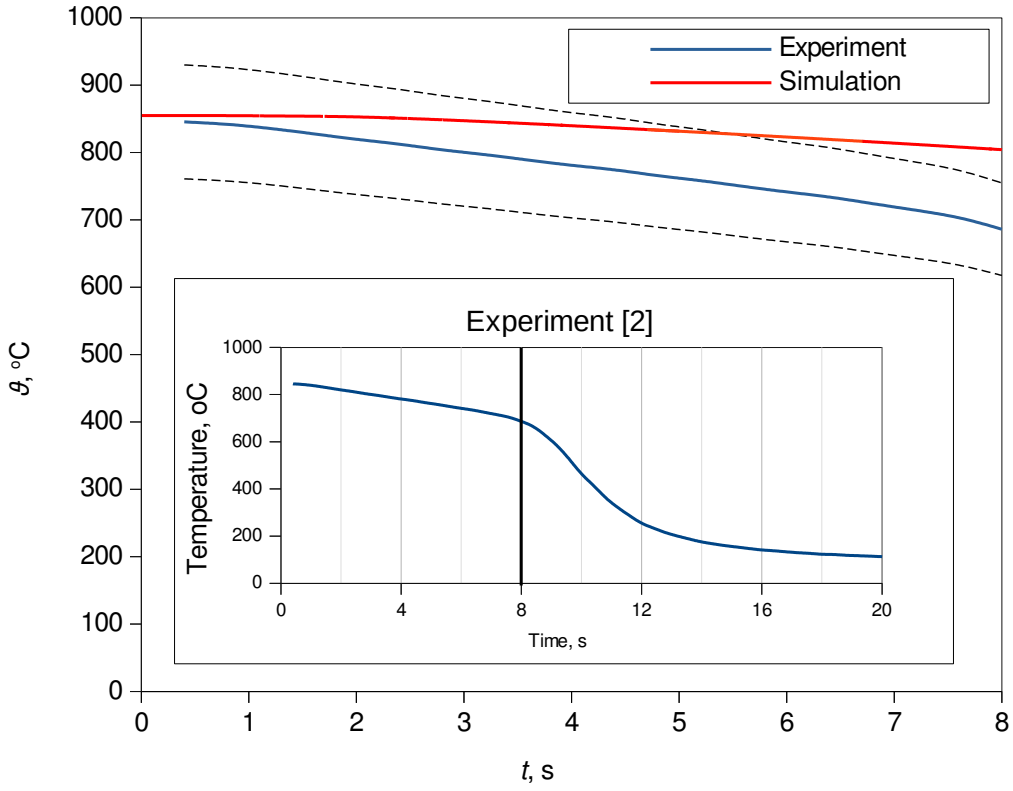


Fig. 33. Comparison of the computational result in the vicinity of the specimen center with the data available from the experiment in Landek et al. ; extracted using .The dashed lines represent 10 % discrepancy from the experimental data.

The obtained temperature distribution exhibits the slope shown in Fig. 33, and a fairly good agreement with the experimental data, say, ca. 10 % is found. Furthermore, it is obvious that this error band covers the majority of the data before an inflection point of the experimental curve is reached; this can be deduced from the prescribed 10 % error band and the auxiliary

plot of the experimental data in Fig. 33. It should be noted that the experimental data has been tracked after the temperature in the specimen's center has reached 849.9 °C [92].

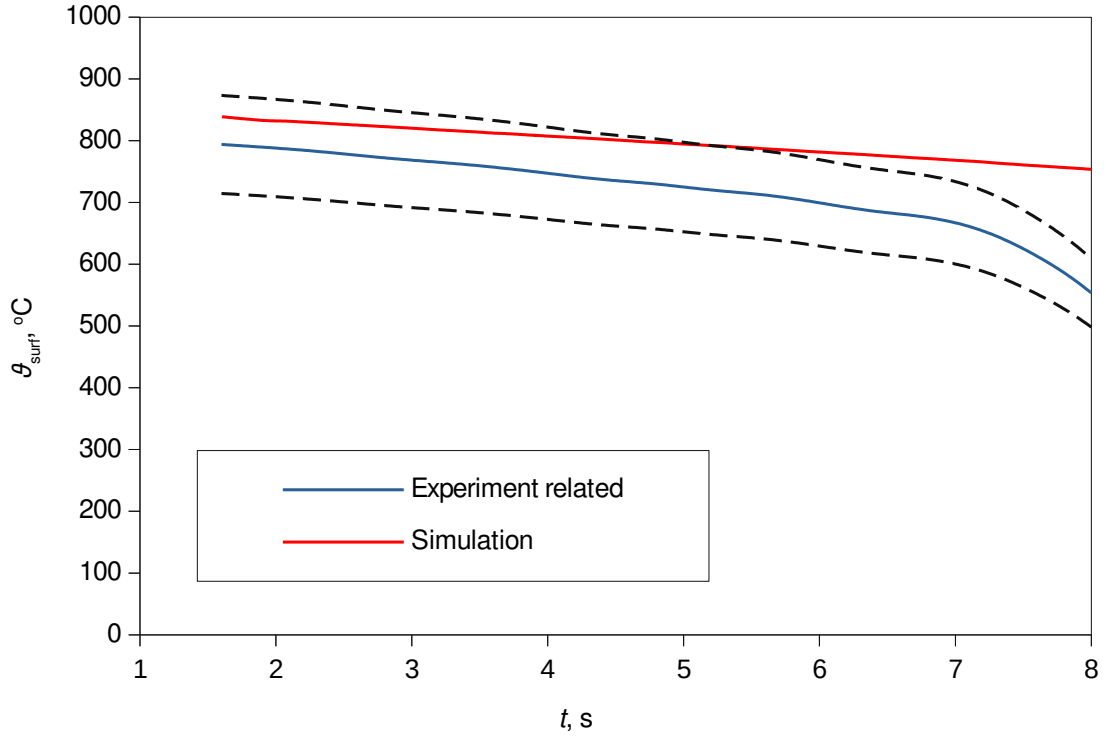


Fig. 34. Comparison of the surface temperature obtained using the data from experiment in Landek et al. and the simulation data. The dashed lines denote 10 % discrepancy from the published data.

It is noteworthy that the experimentally based plot in Fig. 34 is calculated from the inverse heat transfer analysis; hence it is supposed that it has its own computational errors that should be taken into consideration.

The temperature distribution in a solid specimen, Figs. 35 and 36, qualitatively comply with the ones reported in Demirel [86], wherein a solid temperature distributions are obtained using FEM model with experimentally based input data.

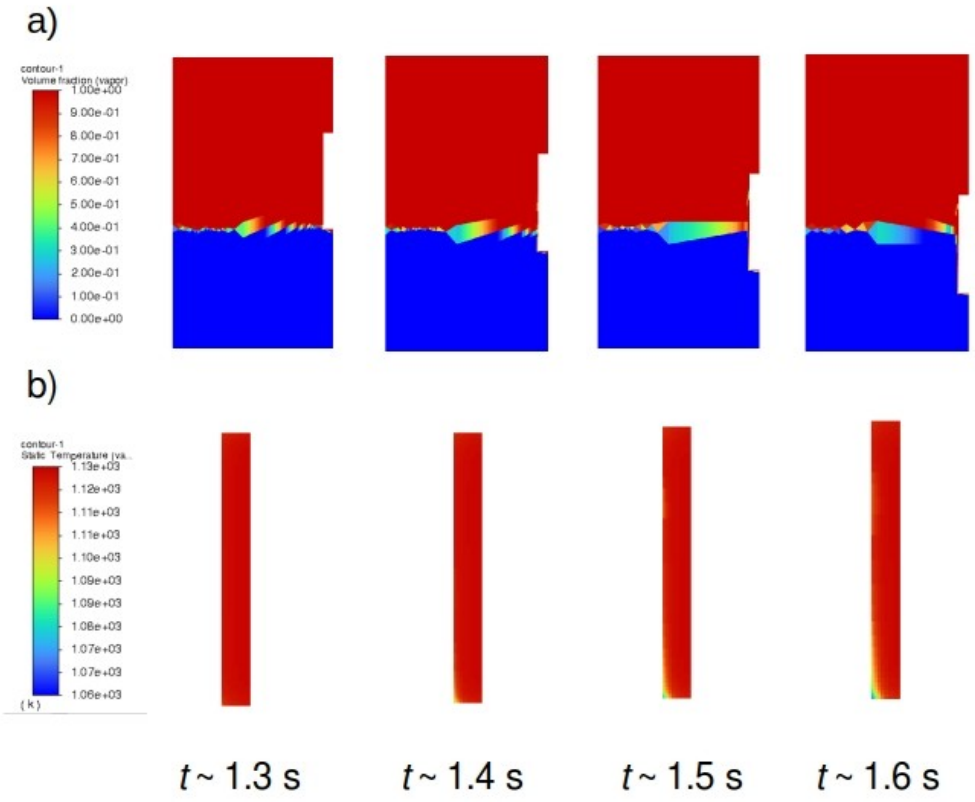


Fig. 35. The volume fraction field evolution in time (a) together with the spatial temperature distribution in solid (b), both being addressed during the immersion process.

This confirms the postulated hypothesis that using Eulerian two-fluid method is able to accurately predict the temperature distribution in a solid material during film boiling mode of immersion quenching process.

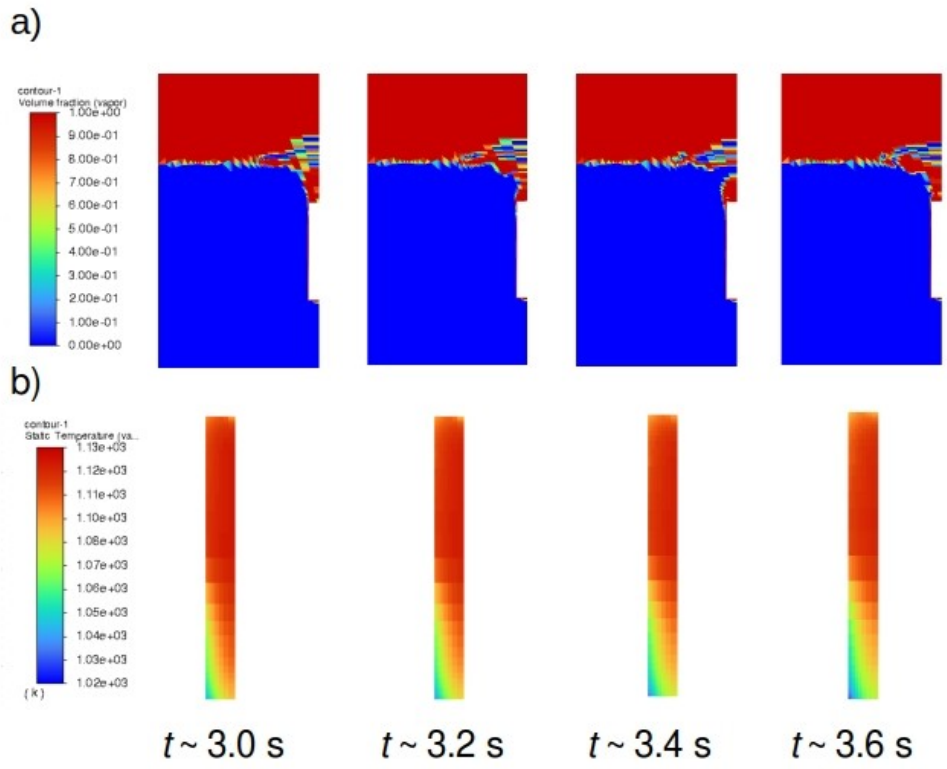


Fig. 36. The vapor volume fraction evolution (a) and temperature field distribution in a solid object (b) during quenching process, whilst the body remains stationary in a liquid medium.

4.2 Heat transfer characteristics

The heat transfer coefficient values presented within this section were obtained on a per surface base, using area weighted average values extracted via the software GUI. The average heat transfer coefficient, when compared to the correlation data obtained using the expressions available in [1], exhibit satisfactory agreement, as shown in Fig. 38.

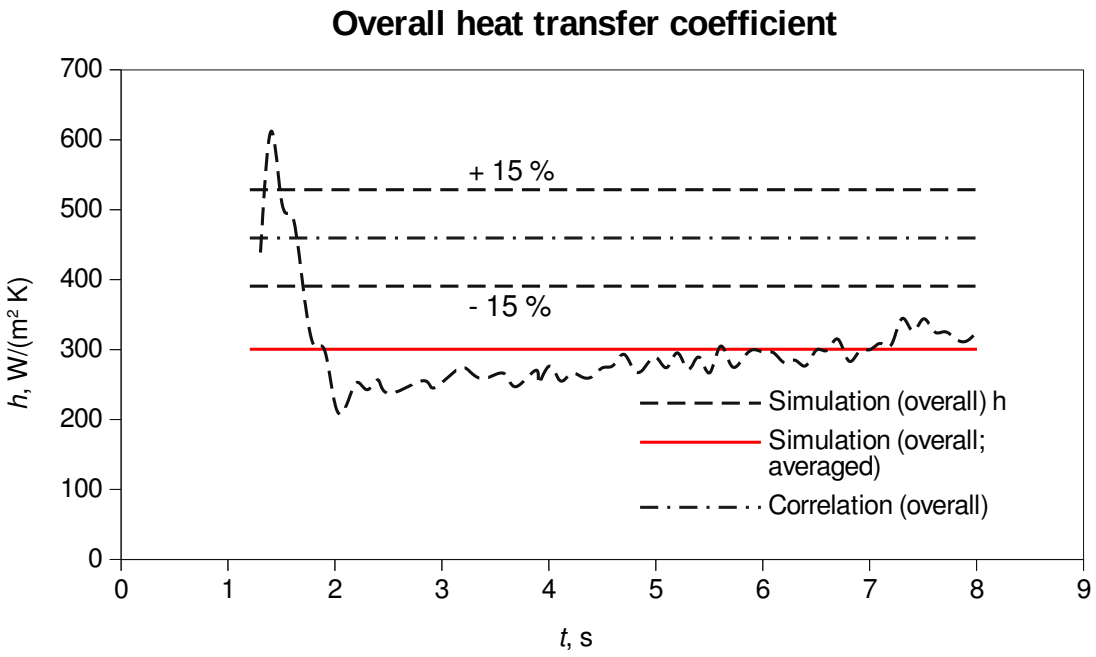


Fig. 37. Comparison of calculated heat transfer coefficients by taking into consideration all heat transfer surfaces with the correlation given in Momoki et al. . The dashed lines denote ± 15 % discrepancy from the correlation result.

We may note that further fine tuning of turbulent kinetic energy may lead to a more accurate result, but, since the intention of the present research is to have a model that is fully, or at least to a great extent, derived from the basic principles and the correspond modeling techniques, such as the LES, this should not be regarded as an appropriate; yet we use the turbulent kinetic energy values applied in paper [73], that deals with an LES study of a boundary layer flow. The value of 0.25 m^2/s^2, that has been addressed in the reference as the highest one, was found as too strong in the validation study conducted herein (Ch. 2; subsection 2.3). Hence, we adopted the medium one, $TKE = 0.1$ m^2/s^2, for the present study. Further improvements should stem from careful theoretical reasoning on instability theory associated with subcooled film boiling flow, such as, for example, in [99].

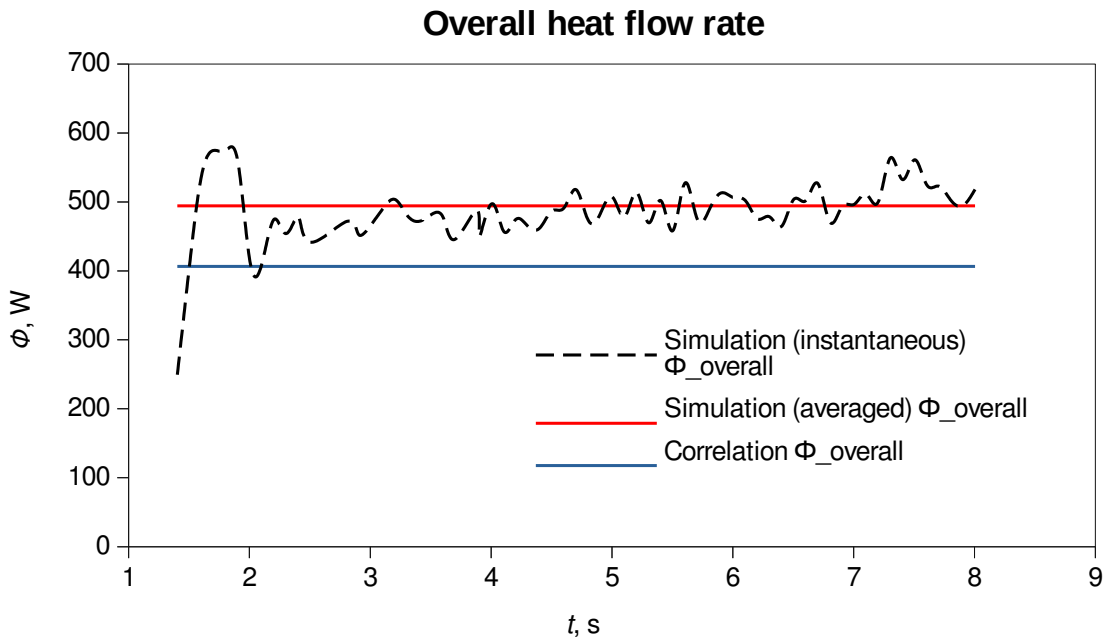


Fig. 38. The overall heat flow rate transferred from the solid specimen during the immersion process, after impact on a free surface level of a liquid quenchant; a comparison with the data obtained using correlations

The heat flow rate has been reported for the whole part, whilst the heat flux partitioning has been selected in heat transfer analysis that follows. It is notable that the calculated heat flow rate by means of numerical simulation agrees with the correlation result with the sufficient level of accuracy, as can be deduced from Fig. 38.

4.2.1 Surface A (horizontal bottom surface)

The heat transfer coefficient calculated using the empirical expressions for subcooled pool film boiling on a horizontal surface of a vertical cylinder specimen, oriented (surface, not cylinder) downward, exhibit the distribution shown in Fig. 39.

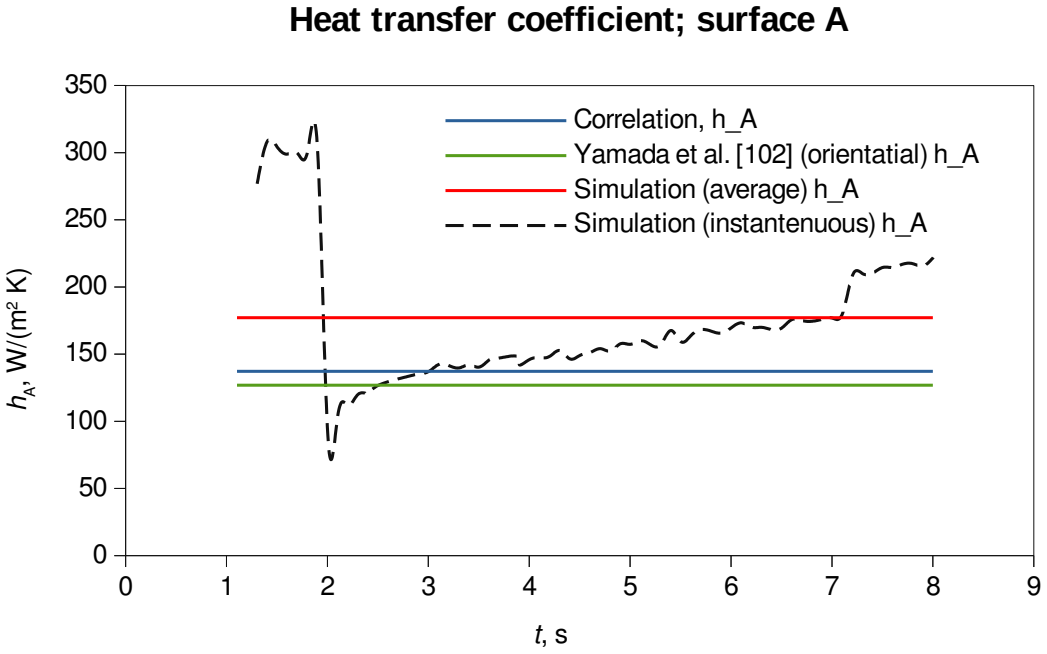


Fig. 39. Comparison of calculated heat transfer coefficientes on the bottom horizontal surface by use of numerical simulation with the ones obtained with correlation available in Momoki et al. and the investigation of 30 x 30 mm cylinder made of silver in .

This is, in the same time, the first one (among the various heat transfer coefficients; namely on surfaces A, B and C) that experiences significant increase in its value as the solid body approaches the free surface of the water, i. e., the liquid medium; an order of magnitude jump of its value is noted at $t \sim 1.3$ s; from 41.16 W/(m^2 K) at $t \sim 1.2$ s up to 276.8 W/(m^2 K) at $t \sim 1.3$ s.

The orientational values are taken from Yamada *et al.* [102] and are obtained using 500 K wall superheat on silver cylinder with $D = L = 30$ mm, with 20 K subcooling, showing thereby the close correspondence between the simulation results and the data obtained using empirical correlations.

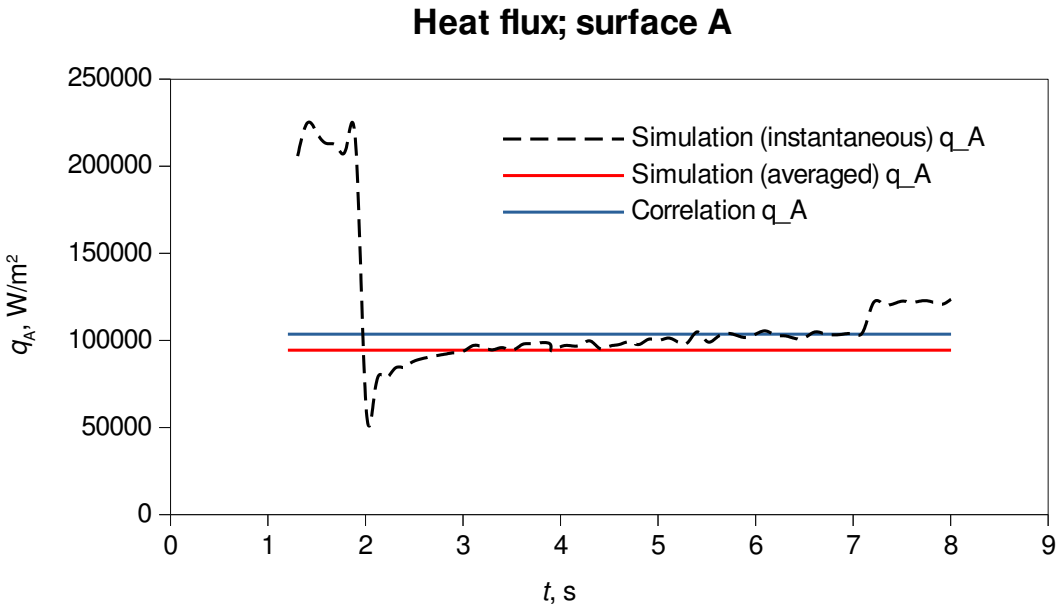


Fig. 40. The distribution of the heat flux values at surface A against time.

The heat flux at the horizontal bottom surface, surface A, exhibits the behavior depicted in Fig. 40. This is, however, the heat transfer surface that firstly experiences the significant increase in heat flux after the material approaches free surface level of the liquid medium. The correlation used in prediction of the heat flux at this surface fits well with the data obtained by use of numerical simulation proposed herein, as could be drawn from the heat flux distributions.

4.2.2 Surface B (vertical lateral surface)

The dominant heat transfer surface in the model proposed in Momoki *et al.* [1], and Yamada *et al.* [102] has been divided into two parts; the smooth interface region (denoted as B1 in the model proposed by the authors), and the wavy interface region (denoted as B2 in those references).

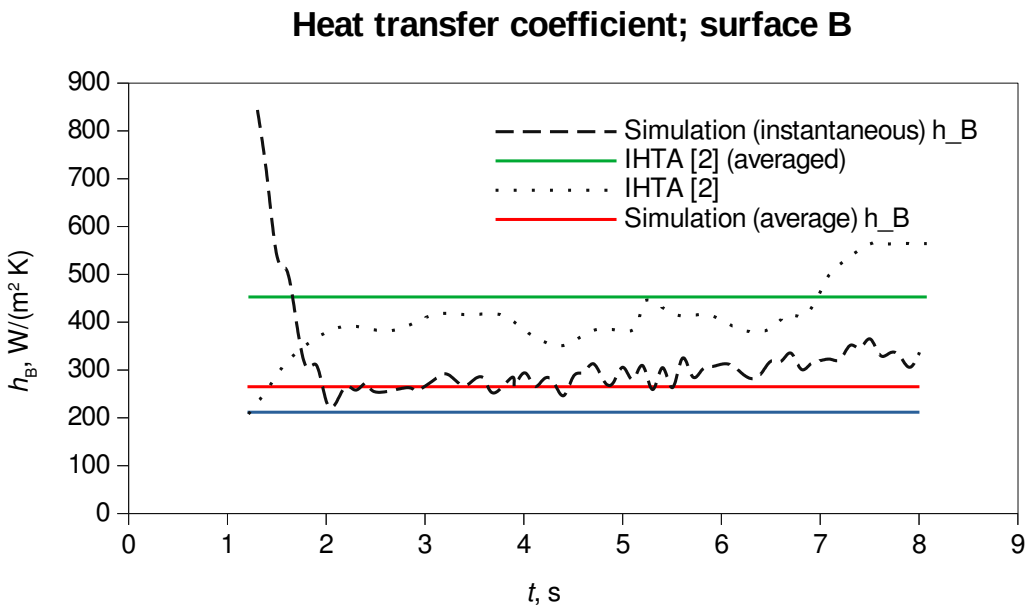


Fig. 41. Comparison of the calculated heat transfer coefficients on the vertical lateral surface with the results obtained using experimental data, presented in Landek et al. , and the ones obtained via the empirical correlation given in Momoki et al. .

Hence, the heat transfer coefficient that embeds both regions is calculated according to definition of the heat transfer coefficient (Newton's cooling law) as:

$$\bar{h}_{\mathrm{B}} = \frac{\bar{q}_{\mathrm{B}}}{\Delta T_{\mathrm{w}}},$$

since both modes employ the same temperature difference, i. e., the wall superheat. Therefore, it is difficult to make direct comparisons with the results in Yamada *et al*. [102]. The resulting plot is, together with simulation (instantaneous and averaged) result plotted in Fig. 41. The average heat transfer coefficient on the cylindrical surface of the Inconel 600 probe (surface B in this simulation), compared to the data available in Landek *et al*. [2], obtained using IHTA agrees reasonably well. This is also shown in Fig. 41.

The heat transfer coefficient at this surface, and, therefore, the corresponding heat flow rates and heat fluxes, that are of interest within the context of present research are those of the immersed part of the solid object. In other words, if half of the body is immersed into the liquid quenchant, then the heat transfer only of immersed part would be considered, not a whole object's heat transfer surface. Hence, a single-phase convection heat transfer from the

non-immersed part is neglected in the context of the present research, at least to a great extent, since it is sometime difficult to sharply determine what is completely immersed part due to motion of the free surface. The consideration of only immersed part has been graphically shown in Demirel [86], whereby $h \neq 0$ is taken inside the liquid quenchant, and $h = 0$ during a single-phase convection to the ambient air.

It is, however, unphysical to consider the average heat transfer coefficients at the vertical lateral surface by taking into consideration the values from the non-immersed part.

This neglection would lead to extremely high heat fluxes and corresponding heat transfer coefficients at the very beginning of the immersion process; thus yielding better agreement with the experimentally obtained data (IHTA) and the ones obtained by use of empirical correlation.

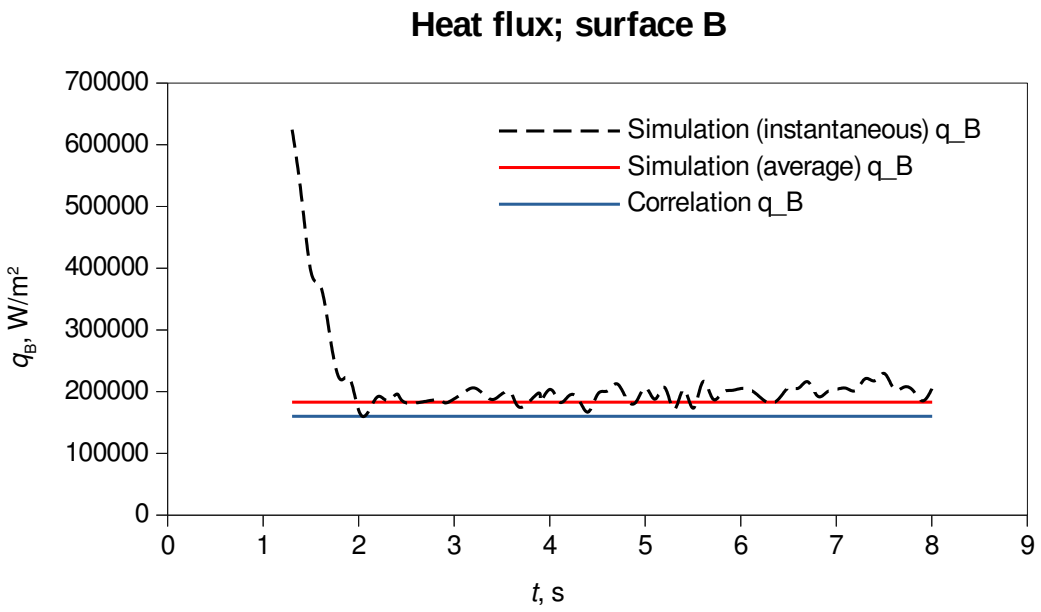


Fig. 42. The heat flux distribution versus time for vertical lateral surface; a comparison between the numerical simulation (instantaneous and the data averaged with respect to time) and the result obtaiend by use of correlation available in Momoki et al. [1].

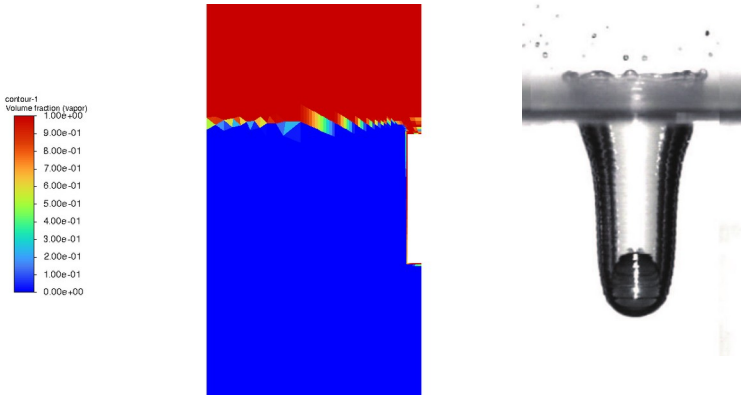
4.2.3 Surface C (top horizontal surface)

It should be noted that the heat transfer coefficient at this surface shows the highest peak values among the studies heat transfer surfaces. However, it has the lowest average value of the

heat transfer coefficient. Fig. 43. shows good agreement between the correlation result and the one obtained with the present model. The similar patterns are recognizable also in the distribution of the heat flux at this surface, Fig. 44.

A measure of similarity has been found between the simulation result and the photographic inspection carried out in [80], denoted in Table 14.

Table 14. A comparison between the flow field obtained using numerical simulation and experimental finding after the solid is immersed into liquid medium.

	Simulation	Experiment [80]
		
Flow field		
$w_{immersion}$, m/s	0.13	1.2
t (from impact), s	~0.5 s	0.043 s
$T_{s,\ init}$	855 °C	500 °C
T_{bulk}	60 °C	95 °C

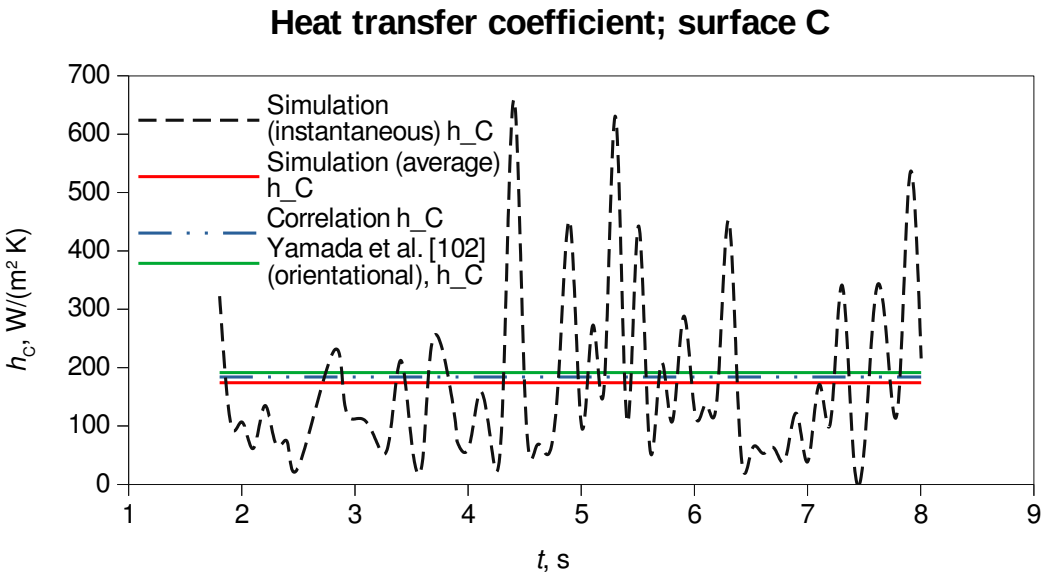


Fig. 43. The heat transfer coefficient distribution on the top horizontal surface, surface C, with respect to time together with the correlation data obtained using the model presented in Momoki et al. [1] *and the data availabale in Yamada et al.* [102].

The top horizontal surface is the last one that participates in the heat transfer with phase-change process, since it becomes relevant after the complete immersion of the solid body into the liquid quenchant. Within the frame of direct interface tracking simulation, it is fully recognizable the crater formation after the top surface of a specimen is located slightly below the free surface level of the liquid medium, as shown in Table 14.

This leads to significantly lower heat transfer coefficient due to inexistence of direct contact with the quenchant, yet the single-phase convection takes place to a significant extent.

The correlation used in estimation of the heat transfer coefficient at the top horizontal surface is based on Berenson's (1961) correlation, and is modified in order to tackle the subcooled film boiling in Momoki *et al.* [1]; also being available in Yamada *et al.* [102] and could be found in Yamada *et al.* [101] as well. The orientation value, obtained from [102], further reveals the close correspondence between the obtained result using the numerical simulation proposed herein with the result obtained in a similar study, but utilizing a slightly different approach.

The fluctuating behavior of the vapor film has been also reported in numerous studies concerning the phase change heat transfer at the horizontal surfaces. Among them, most

notably, the study by Sato and Ničeno [21] presented the graphical comparison with the work of Gaertner [22]. Similar patterns are also observable within the context of the present study.

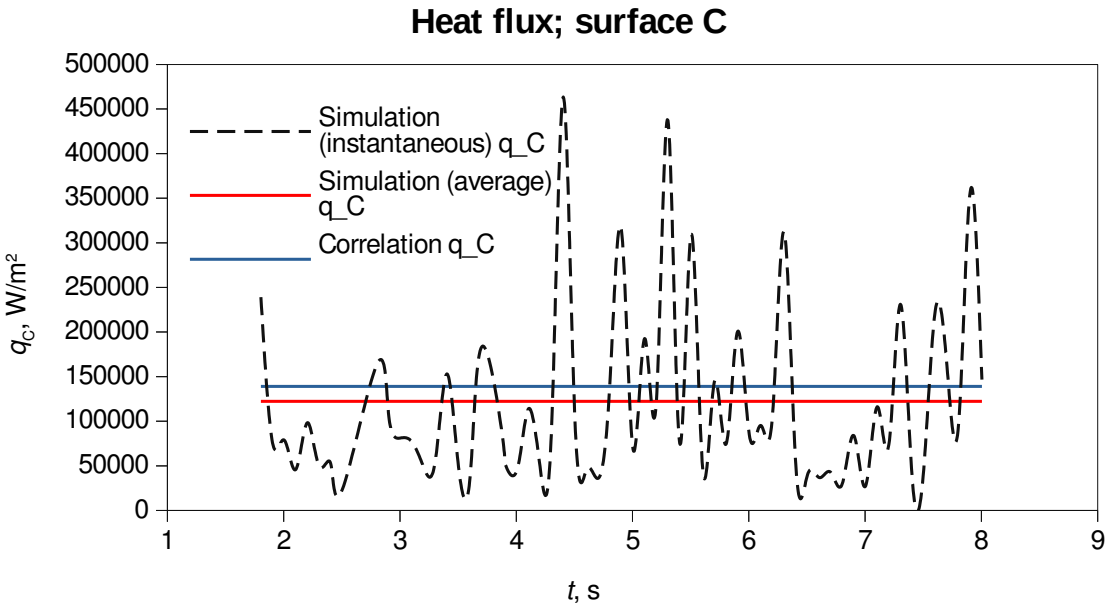


Fig. 44. The instantaneous, averaged (both simulation) and correlation obtained heat flux values at the top horizontal surface.

4.3 Conclusion of Chapter 4

In this chapter the computational results of the performed numerical simulation of immersion quenching process have been carried out. The expected outcomes, i. e., the temperature distribution with respect to time in the specimen center and on its surface were obtained and compared to experimental (central temperatures) and experiment related, calculated, values (surface temperatures). A satisfactory agreement has been achieved, yielding thereby the data that fits to a great extent to the prescribed error band of ± 10 %. Furthermore, the method provides the detailed inspection in the flow fields as well as in the solid temperature distribution, that confirms the stated hypothesis that using the Eulerian two-fluid model one may obtain the accurate field distribution of the temperature evolution in a solid material, based on known initial temperatures of the solid specimen and quenchant medium. In addition, the tracked heat transfer coefficient data, overall for the complete solid object, has shown good agreement with the IHTA and correlation result that match each other; noting thereby that

further refinement of TKE value would provide more accurate result, but, since we want, to a great extent, the model that is based on the basic principles and the derivatives thereof, fine tuning was found as an inappropriate approach in the context of the present study. The reported heat fluxes and the overall heat flow rate agrees relatively well with the correlation data. The graphical inspection has revealed the proper evolution of crater, after the body is immersed into the quenchant. The reported data follows the, say, orientation, data from other investigators.

5 CONCLUSIONS AND FUTURE WORK PERSPECTIVES

5.1 Introduction

In this thesis, a method for estimation of mass transfer across the interface in a phase change simulation has been proposed. The method uses the heat transfer coefficient input as a fictitious function for approximation of the distance between the interface cell's center and an interface, and also to involve the elements of the Fourier law, i. e., being a function of thermal conductivity of the unsaturated phase and a local size of the computational cell; thus constituting the expression for the heat flux, since the temperature difference is already present in the available, thermal phase change, model, wherein the method is implemented and validated. Furthermore, the interface sharpness has been ensured by application of geometrical reconstruction scheme and the computation of the interfacial area density as a gradient of a volume fraction field. Thus, a behavior of a single-fluid VOF method has been successfully reconstructed using two-fluid VOF formulation with, apart from the already mentioned proposed approach, two, say, asymptotic limits, in momentum and energy, and thus in mass conservation, equations; that is, by imposing a large values in terms of interfacial drag term by selection of anisotropic drag model, and to "lock" the temperature at the interface at the saturation point by the application of so-called "zero-resistance" closure on the liquid side of the interface in the applied two-resistance heat transfer model at the interface.

5.2 Conclusions

5.2.1 Verification part

The method is verified using the analytical solution of Stefan problem, and the conclusions related to the developed of the method and thus the verification section are as follows.

1 Stefan problem was accurately solved using the two-fluid VOF model. To this end, the local-parameter based, heat and mass closure was derived, under the assumption of the constant liquid temperature at the saturation.
2 The sharp distribution of the volume fraction of liquid/vapor was achieved by using the geometrical reconstruction scheme implemented in the VOF model.
3 The velocity jump was captured at the interface owing to the sharp distribution of the interfacial area density calculated as the volume fraction gradient.
4 The method is capable to solve Stefan problem on the hybrid mesh predominantly composed of triangular cells with a commensurate level of accuracy. The accurate solutions are also obtained for the stretched quadrilateral mesh.
5 The evaluated relative computational error in calculation of interface position and temperature field, for all the studied cases, agreed with the analytical solution in 5 % and 10 % error band, respectively.

Although the proposed method was validated only for Stefan problem, the application of the method to engineering problems is straightforward because the method only uses a local value: the cell volume.

5.2.2 Validation part

The method is validated using experimental data presented in Momoki *et al*. [1] and are extracted using the Web software [65]. The silver specimen has been subjected to a liquid medium, water, at saturation temperature; hence, the vapor film thickness is mostly pronounced. To accomplish this by use of numerical simulation, additional treatment of turbulent kinetic energy has been carried out in order to extract the, at least to a commensurate level of accuracy, the heat flux from the specimen, and, therefore, to accurately estimate the temperature field in a solid specimen; a transient CHT approach has been used in the simulation of the film boiling, and the accuracy of the model has been evaluated from the viewpoint of temporal distribution of the solid temperature in the vicinity of a particular point in a solid body.

The TKE value has been obtained by using a parametric study, i. e., it was varied until a sufficiently correct estimate of a solid temperature was obtained. The TKE value of 0.25 m^2/s^2 has been found as a reasonably accurate, i. e., a ± 2 % accurate temperature distribution in the

immediate neighborhood of the specimen center was obtained in ~ 10 % of the total duration of stable film boiling.

Hence, a transient CHT film boiling simulation in axis-symmetric coordinate system has been carried out within the validation part of the work, and the following conclusions may be drawn:

1. The shared velocity field values at the interface have represented accurately the interface behavior also in the case of more complex interface evolution.
2. The application of the dispersed turbulence model is necessary in order to correctly estimate the temperature distribution in a solid; that is, the BIT may be assumed in the present context of the pool film boiling.
3. The application of Kelvin-Helmholtz instability theory in estimation of TKE magnitudes has been found as very straightforward when used in conjunction with the boundary layer theory in estimation of the necessary velocity input.
4. The obtained heat transfer coefficient values exhibit a cyclic character, the same as the evolution of vapor-liquid interface, as shown by the other authors.
5. The obtained heat transfer coefficients only locally enter the prescribed error bandwidth of ± 15 %, whilst the average value in slightly above 30 %.
6. The temperature distribution in a solid material has agreed with the measured values in, say, ~ 10 % of total duration of film boiling phase.
7. The selected turbulence model has exhibited a realistic value of turbulent viscosity inside the vapor film, which may be addressed to usage of C_μ factor that, among other variables, depend on strain rate.

Thus, ample room for method application is made by incorporation of the findings presented so far.

5.2.3 Application case

The formerly presented outputs are also relevant for the application case, wherein the following conclusions may be drawn:

1. A reasonable agreement between the numerical simulation and the experimental data has been observed for the temperatures in the vicinity of the solid specimen's center; i. e., the cooling characteristics may be reasonably accurate estimated in the film boiling mode of immersion quenching process, yielding the result that enters inside a ± 10 % solution accuracy when compared with the experimental data. further improvements on TKE value are claimed as the ones that may result in even more accurate result.
2. The obtained heat transfer coefficients follow the patterns of the averaged data obtained using IHTA and the correlation ones. Although further refinement of the TKE value would yield, most probably, the more accurate result, it is claimed that it should stem from careful theoretical reasoning instead of fine tuning any simulation parameter.
3. The vapor explosion has been successfully reconstructed by use of the present numerical method, as observed from the heat flow rates (heat fluxes) and, therefore, the heat transfer coefficients, especially at the bottom horizontal surface of the cylinder that is first one which experiences the rapid jump in these heat transfer characteristics.
4. The formation of a crater after the solid body is being completely immersed into liquid medium and its impact heat transfer have been also captured in the present simulation case; graphical inspection reveals its increased presence due to phase change process that is present in the flow.
5. Further exploration on the partitioned heat transfer may reveal some hidden aspects of the results obtained herein; generally speaking, the heat flow rates agree reasonably well with the data obtained using correlation.
6. The application of hybrid meshes has been found as valuable due to mesh motion and the associated topological change due to remeshing; although a temperature limiter was needed to be included in the case of turbulent flow to limit the lower temperature that is allowed in the domain.
7. The interpolation of variables has been established using Green-Gauss node-based method, due to triangular cells that are present in the domain, in conjunction with the BiCGSTAB method for solving linear system of equations, that is necessary in order to improve the solution stability.

Finally, it is shown that the accepted method is suitable for film boiling simulation during the immersion quenching process in a sense that the temperature evolution in a solid object, subjected to the immersion quenching process can be accurately estimated, together with the complete heat transfer characteristic, such as: the heat transfer coefficients and heat flow rates.

This confirms the stated hypothesis that the temperature evolution in a solid could be successfully tracked during film boiling mode of immersion quenching process by application of Eulerian two-fluid method.

5.3 Future work

The proposed computational model is simple to implement and is based primarily on the basic principles implemented within the framework of two-fluid VOF method in the commercial CFD code ANSYS Fluent. Therefore, due to its simplicity and continuum mechanics background, one may distinguish further future steps:

1. Further research should be aimed at revealing the hidden aspects of the model in resolving fundamental boiling flows, such as vapor bubble rise and nucleate pool boiling.
2. Turbulence modeling in the case of film boiling should be studied further; it is known that there is a class of problems that may be accurately computed only using DNS or LES. Hence, more research in this regard is needed to exploit some conclusions on proper turbulence modeling in the case of film boiling supplemented with conjugate heat transfer.
3. Further considerations of turbulent flow may include so-called "zero-equation" turbulence modeling, or a mixing length hypothesis (MLH) model, which is applicable in the case of parallel flows, as noted in van Dijk [103], such as the fully developed pipe flow or a flow in a diverging channel, where stream-wise velocity gradient equals zero, that is, $\partial \bar{u}/\partial x = 0$ and characteristic length scales are of order $L_2 >> L_1$, respectively.
4. Although not considered in this study, the thermal radiation heat transfer may have some influence due to existence of vapor phase. Since the vapor is a participating in radiation heat transfer, involvement of selective radiation of gases may have some content in future investigations.

Of course, the other phase change simulations, such as solidification and melting inside the package ANSYS Fluent, that are stated in the documentation that do not work with two-fluid formulation are now possible to be carried out, based on the principles shown in the verification part.

5.4 Conclusion of Chapter 5

This chapter has closed the research carried out within the context of numerical simulation of film boiling during metal materials quenching in a vaporizing medium. It was shown that the stated hypothesis has been successfully confirmed, although the two-fluid formalism is not usual choice for stratified two-phase flow, with a sharp large interface. To alleviate the drawbacks of inexistence of sharp interface in the default two-fluid modeling approach, the enhanced two-fluid model formulation that incorporates VOF method has been chosen to this end, with selection of proper closures to close the mathematical modeling. As a result, a novel mass transfer model has been proposed and a wide variety of further industrial applications could be made by its use within the context of heat transfer with phase change processes. Supplemented with proper TKE value, the model is fully capable, at least to a certain extent, of accurately modeling the CHT problems on the large-scale domains, using relatively high time increments.

REFERENCES

[1] S. Momoki, T. Yamada, T. Shigechi, K. Kanemaru, T. Yamaguchi, Film Boiling Around a Vertical Cylinder With Top and Bottom Horizontal Surfaces, in: HT2007, ASME/JSME 2007 Thermal Engineering Heat Transfer Summer Conference, Volume 2, 2007: pp. 611–619. https://doi.org/10.1115/HT2007-32733.

[2] D. Landek, J. Župan, T. Filetin, A Prediction of Quenching Parameters Using Inverse Analysis, Matls. Perf. Charact. 3 (2014) 229–241. https://doi.org/10.1520/MPC20130109.

[3] Krumes, Dragomir, Toplinska obradba, Slavonski Brod: Strojarski fakultet, Slavonski Brod, 2000.

[4] Galović, Antun, Termodinamika II, Fakultet strojarstva i brodogradnje, Sveučilište u Zagrebu, Zagreb, 2014.

[5] B. Liščić, H.M. Tensi, W. Luty, eds., Theory and Technology of Quenching, Springer Berlin Heidelberg, Berlin, Heidelberg, 1992. https://doi.org/10.1007/978-3-662-01596-4.

[6] H.M. Tensi, Wetting Kinematics, in: B. Liščić, H.M. Tensi, W. Luty (Eds.), Theory and Technology of Quenching: A Handbook, Springer, Berlin, Heidelberg, 1992: pp. 93–116. https://doi.org/10.1007/978-3-662-01596-4_5.

[7] I. Felde, W. Shi, Hybrid approach for solution of inverse heat conduction problems, in: 2014 IEEE International Conference on Systems, Man, and Cybernetics (SMC), IEEE, 2014: pp. 3896–3899.

[8] Z. Pan, J.A. Weibel, S.V. Garimella, A saturated-interface-volume phase change model for simulating flow boiling, International Journal of Heat and Mass Transfer. 93 (2016) 945–956. https://doi.org/10.1016/j.ijheatmasstransfer.2015.10.044.

[9] D.G. Kim, C.H. Jeon, I.S. Park, Comparison of numerical phase-change models through Stefan vaporizing problem, International Communications in Heat and Mass Transfer. 87 (2017) 228–236. https://doi.org/10.1016/j.icheatmasstransfer.2017.07.013.

[10] N. El Kosseifi, T. Coupez, E. Causse-Massoni, Numerical simulation of boiling for industrial quenching processes, Simulation numérique de l'ébullition pour les procédés de trempe industrielle, Ecole Nationale Supérieure des Mines de Paris, 2012. https://pastel.archives-ouvertes.fr/pastel-00734601.

[11] D.-L. Sun, J.-L. Xu, L. Wang, Development of a vapor–liquid phase change model for volume-of-fluid method in FLUENT, International Communications in Heat and Mass Transfer. 39 (2012) 1101–1106. https://doi.org/10.1016/j.icheatmasstransfer.2012.07.020.

[12] Y. Sato, B. Ničeno, A sharp-interface phase change model for a mass-conservative interface tracking method, Journal of Computational Physics. 249 (2013) 127–161. https://doi.org/10.1016/j.jcp.2013.04.035.

[13] I. Perez-Raya, S.G. Kandlikar, Discretization and implementation of a sharp interface model for interfacial heat and mass transfer during bubble growth, International Journal of Heat and Mass Transfer. 116 (2018) 30–49. https://doi.org/10.1016/j.ijheatmasstransfer.2017.08.106.

[14] B.A. Nichita, ed., An Improved CFD Tool to Simulate Adiabatic and Diabatic Two-Phase Flows, EPFL, Lausanne, 2010. https://doi.org/10.5075/epfl-thesis-4776.

[15] M. <1982> Magnini, CFD modeling of two-phase boiling flows in the slug flow regime with an interface capturing technique, Doctoral Thesis, Alma Mater Studiorum - Università di Bologna, 2012. https://doi.org/10.6092/unibo/amsdottorato/4437.

[16] R. Arévalo, D. Antúnez, L. Rebollo, A. Abánades, Estimation of radiation coupling factors in film boiling around spheres by mean of Computational Fluid Dynamics (CFD) tools, International Journal of Heat and Mass Transfer. 78 (2014) 84–89. https://doi.org/10.1016/j.ijheatmasstransfer.2014.06.063.

[17] I. Perez-Raya, S.G. Kandlikar, Chapter Three - Evaporation on a Planar Interface – Numerical Simulation and Theoretical Analysis of Heat and Mass Transport Processes, in: E.M. Sparrow, J.P. Abraham, J.M. Gorman, T.F. Irvine, J.P. Hartnett (Eds.), Advances in Heat Transfer, Elsevier, 2016: pp. 125–190. https://doi.org/10.1016/bs.aiht.2016.08.005.

[18] C.R. Kharangate, I. Mudawar, Review of computational studies on boiling and condensation, International Journal of Heat and Mass Transfer. 108 (2017) 1164–1196. https://doi.org/10.1016/j.ijheatmasstransfer.2016.12.065.

[19] M. Magnini, B. Pulvirenti, J.R. Thome, Numerical investigation of hydrodynamics and heat transfer of elongated bubbles during flow boiling in a microchannel, International Journal of Heat and Mass Transfer. 59 (2013) 451–471. https://doi.org/10.1016/j.ijheatmasstransfer.2012.12.010.

[20] O. Kartuzova, M. Kassemi, Modeling interfacial turbulent heat transfer during ventless pressurization of a large scale cryogenic storage tank in microgravity, in: 47th AIAA/ASME/SAE/ASEE Joint Propulsion Conference & Exhibit, 2011: p. 6037.

[21] Y. Sato, B. Niceno, Pool boiling simulation using an interface tracking method: From nucleate boiling to film boiling regime through critical heat flux, International Journal of Heat and Mass Transfer. 125 (2018) 876–890. https://doi.org/10.1016/j.ijheatmasstransfer.2018.04.131.

[22] R.F. Gaertner, Photographic Study of Nucleate Pool Boiling on a Horizontal Surface, Journal of Heat Transfer. 87 (1965) 17–27. https://doi.org/10.1115/1.3689038.

[23] N. Saini, I.A. Bolotnov, Two-Phase Turbulence Statistics from High Fidelity Dispersed Droplet Flow Simulations in a Pressurized Water Reactor (PWR) Sub-Channel with Mixing Vanes, Fluids. 6 (2021). https://doi.org/10.3390/fluids6020072.

[24] F. Krause, S. Schüttenberg, U. Fritsching, Modelling and simulation of flow boiling heat transfer, International Journal of Numerical Methods for Heat & Fluid Flow. 20 (2010) 312–331. https://doi.org/10.1108/09615531011024066.

[25] V. Srinivasan, K.-M. Moon, D. Greif, D.M. Wang, M. Kim, Numerical simulation of immersion quench cooling process using an Eulerian multi-fluid approach, Applied Thermal Engineering. 30 (2010) 499–509. https://doi.org/10.1016/j.applthermaleng.2009.10.012.

[26] V. Srinivasan, K.-M. Moon, D. Greif, D.M. Wang, M. Kim, Numerical simulation of immersion quenching process of an engine cylinder head, Applied Mathematical Modelling. 34 (2010) 2111–2128. https://doi.org/10.1016/j.apm.2009.10.023.

[27] J.U. Brackbill, D.B. Kothe, C. Zemach, A continuum method for modeling surface tension, Journal of Computational Physics. 100 (1992) 335–354. https://doi.org/10.1016/0021-9991(92)90240-Y.

[28] R. Kopun, L. Škerget, M. Hriberšek, D. Zhang, W. Edelbauer, Numerical Investigations of Quenching Cooling Processes for Different Cast Aluminum Parts, Strojniški Vestnik - Journal of Mechanical Engineering; Vol 60, No 9 (2014): Strojniški Vestnik - Journal of Mechanical Engineering. (2018). https://doi.org/10.5545/sv-jme.2014.1705.

[29] P. Stark, U. Fritsching, Simulation of the impinging liquid jet cooling process of a flat plate, International Journal of Numerical Methods for Heat & Fluid Flow. 25 (2015) 153–170. https://doi.org/10.1108/HFF-04-2013-0151.

[30] S. Maharshi, COMPUTATIONAL MODELLING OF LIQUID JET IMPINGEMENT ONTO HEATED SURFACE, Ph.D. Thesis, Technische Universität, 2017. https://tuprints.ulb.tu-darmstadt.de/6217/ (accessed July 13, 2022).

[31] C. Bahbah, Méthodes numériques avancées pour la simulation du procédé de trempe industrielle, phdthesis, Université Paris sciences et lettres, 2020. https://pastel.archives-ouvertes.fr/tel-03157524 (accessed July 13, 2022).

[32] G. Černe, S. Petelin, I. Tiselj, Coupling of the Interface Tracking and the Two-Fluid Models for the Simulation of Incompressible Two-Phase Flow, Journal of Computational Physics. 171 (2001) 776–804. https://doi.org/10.1006/jcph.2001.6810.

[33] S. Mer, O. Praud, H. Neau, N. Merigoux, J. Magnaudet, V. Roig, The emptying of a bottle as a test case for assessing interfacial momentum exchange models for Euler–Euler simulations of multi-scale gas-liquid flows, International Journal of Multiphase Flow. 106 (2018) 109–124. https://doi.org/10.1016/j.ijmultiphaseflow.2018.05.002.

[34] P. Coste, A Large Interface Model for two-phase CFD, Nuclear Engineering and Design. 255 (2013) 38–50. https://doi.org/10.1016/j.nucengdes.2012.10.008.

[35] R. Denèfle, J.-P. Caltagirone, S. Vincent, Local two-phase modeling of the water-steam flows occurring in steam generators, Modélisation locale diphasique eau-vapeur des écoulements dans les générateurs de vapeur, Université Sciences et Technologies - Bordeaux I, 2013. https://tel.archives-ouvertes.fr/tel-00919975.

[36] D.A. Drew, S.L. Passman, Introduction, in: D.A. Drew, S.L. Passman (Eds.), Theory of Multicomponent Fluids, Springer New York, New York, NY, 1999: pp. 1–9. https://doi.org/10.1007/0-387-22637-0_1.

[37] D.A. Drew, S.L. Passman, Classical Theory of Solutions, in: Theory of Multicomponent Fluids, Springer, 1999: pp. 59–61.

[38] Ansys® Fluent, ANSYS Fluent Theory Guide, Release 19.2, ANSYS, Inc., n.d.

[39] T. Höhne, C. Vallée, Experiments and Numerical Simulations of Horizontal Two-Phase Flow Regimes Using an Interfacial Area Density Model, The Journal of Computational Multiphase Flows. 2 (2010) 131–143. https://doi.org/10.1260/1757-482X.2.3.131.

[40] C.R. Kharangate, H. Lee, I. Mudawar, Computational modeling of turbulent evaporating falling films, International Journal of Heat and Mass Transfer. 81 (2015) 52–62. https://doi.org/10.1016/j.ijheatmasstransfer.2014.09.068.

[41] L. Štrubelj, I. Tiselj, B. Mavko, Simulations of free surface flows with implementation of surface tension and interface sharpening in the two-fluid model, International Journal of Heat and Fluid Flow. 30 (2009) 741–750. https://doi.org/10.1016/j.ijheatfluidflow.2009.02.009.

[42] Ansys® Fluent, VOF Model, (2017). https://support.ansys.com/.

[43] S. Fleau, S. Vincent, S. Mimouni, Multifield approach and interface locating method for two-phase flows in nuclear power plant, Modélisation des écoulements eau-vapeur « tous régimes d'écoulements » par une approche multi-champ, Université Paris-Est, 2017. https://tel.archives-ouvertes.fr/tel-01621735.

[44] G. Chen, T. Nie, X. Yan, An explicit expression of the empirical factor in a widely used phase change model, International Journal of Heat and Mass Transfer. 150 (2020) 119279. https://doi.org/10.1016/j.ijheatmasstransfer.2019.119279.

[45] S. Pertant, G. Balarac, Numerical simulation of two phase flows with contact line and phase change on unstructured meshes, Simulation numérique d'écoulements diphasiques avec ligne triple et changement de phase sur maillages non structurés, Université Grenoble Alpes [2020-....], 2022. https://tel.archives-ouvertes.fr/tel-03638270.

[46] V.P. Carey, Liquid Vapor Phase Change Phenomena: An Introduction to the Thermophysics of Vaporization and Condensation Processes in Heat Transfer Equipment, Second Edition, Taylor & Francis, 2007. https://books.google.hr/books?id=COokAAAACAAJ.

[47] C. Geuzaine, J.-F. Remacle, Gmsh: A 3-D finite element mesh generator with built-in pre- and post-processing facilities, International Journal for Numerical Methods in Engineering. 79 (2009) 1309–1331. https://doi.org/10.1002/nme.2579.

[48] J.O. Hinze, Turbulence. McGraw-Hill Publishing Co, New York. (1975).

[49] N.C. Markatos, The mathematical modelling of turbulent flows, Applied Mathematical Modelling. 10 (1986) 190–220. https://doi.org/10.1016/0307-904X(86)90045-4.

[50] F. Hoppe, M. Breuer, A deterministic breakup model for Euler–Lagrange simulations of turbulent microbubble-laden flows, International Journal of Multiphase Flow. 123 (2020) 103119. https://doi.org/10.1016/j.ijmultiphaseflow.2019.103119.

[51] G. Philip, Measurement of turbulence in an annular jet, University of Missouri--Rolla, 1972.

[52] M. Kimber, J. Brigham, A. Jana, Experimentally Validated Numerical Models of Non-Isothermal Turbulent Mixing in High Temperature Reactors, 2018. https://doi.org/10.2172/1461189.

[53] J. Padet, Fluides en Ecoulement - Méthodes et Modèles. 2° Edition, 2011.

[54] B. Ničeno, M.T. Dhotre, N.G. Deen, One-equation sub-grid scale (SGS) modelling for Euler–Euler large eddy simulation (EELES) of dispersed bubbly flow, Chemical Engineering Science. 63 (2008) 3923–3931. https://doi.org/10.1016/j.ces.2008.04.050.

[55] Kashima H., Mori N., Mizutani N., Visualization on Air Bubble Characteristics of the Surf Zone Breaking Waves, PROCEEDINGS OF COASTAL ENGINEERING, JSCE. 54 (2007) 56–60. https://doi.org/10.2208/proce1989.54.56.

[56] N. Mori, T. Suzuki, S. Kakuno, Experimental study of air bubbles and turbulence characteristics in the surf zone, J. Geophys. Res. 112 (2007) C05014. https://doi.org/10.1029/2006JC003647.

[57] C.V. Makris, C.D. Memos, Y.N. Krestenitis, Numerical modeling of surf zone dynamics under weakly plunging breakers with SPH method, Ocean Modelling. 98 (2016) 12–35. https://doi.org/10.1016/j.ocemod.2015.12.001.

[58] E. Cascioli, S. Buckingham, S. Keijers, K.V. Tichelen, S. Kenjeres, Numerical and experimental analysis of a planar jet with heated co-flow at medium and low Prandtl-number values, Nuclear Engineering and Design. 361 (2020) 110570. https://doi.org/10.1016/j.nucengdes.2020.110570.

[59] A. Sakurai, M. Shiotsu, K. Hata, A General Correlation for Pool Film Boiling Heat Transfer From a Horizontal Cylinder to Subcooled Liquid: Part 1—A Theoretical Pool Film Boiling Heat Transfer Model Including Radiation Contributions and Its Analytical Solution, Journal of Heat Transfer. 112 (1990) 430–440. https://doi.org/10.1115/1.2910396.

[60] J. Baber, Experimental Investigation on Water Film Characteristics and Droplets Formation around Cascade Blade, The University of Tokyo, 2017. https://repository.dl.itc.u-tokyo.ac.jp/records/50298 (accessed July 14, 2022).

[61] A. Hillier, T.V. Doorsselaere, K. Karampelas, Estimating the Energy Dissipation from Kelvin–Helmholtz Instability Induced Turbulence in Oscillating Coronal Loops, ApJL. 897 (2020) L13. https://doi.org/10.3847/2041-8213/ab9ca3.

[62] T. Yamada, T. Shigechi, S. Momoki, K. Kanemaru, An Analysis of Film Boiling around a Vertical Finite-Length Cylinder, 長崎大学工学部研究報告. 31 (2001) 1–11.

[63] Halasz, Boris, Galović, Antun, Boras, Ivanka, Toplinske tablice, FSB, Zagreb, 2013.

[64] Krasniqi, Marigona, Истражување на можности за подобрување на енергетската ефикасност и намалување на емисиите на енергетски парогенератор на јаглен; Investigation of opportunities for energy efficiency improvement and emissions reduction of utility coal-fired steam generator, Thesis, Машински факултет, УКИМ, Скопје, 2021. https://repository.ukim.mk:443/handle/20.500.12188/16538 (accessed October 4, 2022).

[65] A. Rohatgi, Webplotdigitizer: Version 4.5, (2021). https://automeris.io/WebPlotDigitizer.

[66] A. Galović, ODABRANA POGLAVLJA IZ KONDUKCIJE, (2003).

[67] Y.-Y. Tsui, S.-W. Lin, Y.-N. Lai, F.-C. Wu, Phase change calculations for film boiling flows, International Journal of Heat and Mass Transfer. 70 (2014) 745–757. https://doi.org/10.1016/j.ijheatmasstransfer.2013.11.061.

[68] D. Juric, G. Tryggvason, Computations of boiling flows, International Journal of Multiphase Flow. 24 (1998) 387–410. https://doi.org/10.1016/S0301-9322(97)00050-5.

[69] Yamada, Takashi, 水平の底面と上面を有する垂直円柱まわりの膜沸騰熱伝達に関する研究; Study on Film Boiling Heat Transfer around a Vertical Cylinder with Top and Bottom Horizontal Surfaces, (2007). https://nagasaki-u.repo.nii.ac.jp/?action=repository_uri&item_id=22671&file_id=70&file_no=1.

[70] F. Gauss, D. Lucas, E. Krepper, Grid studies for the simulation of resolved structures in an Eulerian two-fluid framework, Nuclear Engineering and Design. 305 (2016) 371–377. https://doi.org/10.1016/j.nucengdes.2016.06.009.

[71] W.D. Pointer, Y. Liu, EULERIAN TWO-FLUID RANS-BASED CFD SIMULATIONS OF A HELICAL COIL STEAM GENERATOR BOILING TUBE, (n.d.) 19.

[72] M.D. Zimmer, I.A. Bolotnov, Exploring Two-Phase Flow Regime Transition Mechanisms Using High-Resolution Virtual Experiments, Nuclear Science and Engineering. 194 (2020) 708–720. https://doi.org/10.1080/00295639.2020.1722543.

[73] I. Vinkovic, C. Aguirre, S. Simoëns, M. Gorokhovski, Large-eddy simulation of droplet dispersion for inhomogeneous turbulent wall flow, International Journal of Multiphase Flow. 32 (2006) 344–364. https://doi.org/10.1016/j.ijmultiphaseflow.2005.10.005.

[74] C. Heschl, K. Inthavong, W. Sanz, J. Tu, Nonlinear eddy viscosity modeling and experimental study of jet spreading rates, Indoor Air. 24 (2014) 93–102. https://doi.org/10.1111/ina.12050.

[75] K. Herman, Teorija elastičnosti i plastičnosti, Element, 2008.

[76] Heschl, Christian, Ein Beitrag zur numerischen Berechnung turbulenter Raumluftströmungen, Technischen Universität Graz, 2010. https://diglib.tugraz.at/download.php?id=576a7a588e89c&location=browse.

[77] N.R.S. Toso, Contribution to the modelling and simulation of aircraft structures impacting on water, Beitrag zur Modellierung und Simulation von Luftfahrtstrukturen beim Wasseraufprall. (2009). https://doi.org/10.18419/opus-3823.

[78] K.M.T. Kleefsman, G. Fekken, A.E.P. Veldman, B. Iwanowski, B. Buchner, A Volume-of-Fluid based simulation method for wave impact problems, Journal of Computational Physics. 206 (2005) 363–393. https://doi.org/10.1016/j.jcp.2004.12.007.

[79] J. Bašić, N. Degiuli, A. Werner, Simulation of water entry and exit of a circular cylinder using the ISPH method, Transactions of FAMENA. 38 (2014) 45–62.

[80] J.-C. Li, Y.-J. Wei, C. Wang, W.-X. Xia, Cavity formation during water entry of heated spheres, Chinese Phys. B. 27 (2018) 094703. https://doi.org/10.1088/1674-1056/27/9/094703.

[81] A. Jetly, I.U. Vakarelski, Z. Yang, S.T. Thoroddsen, Giant drag reduction on Leidenfrost spheres evaluated from extended free-fall trajectories, Experimental Thermal and Fluid Science. 102 (2019) 181–188. https://doi.org/10.1016/j.expthermflusci.2018.11.010.

[82] J. Gylys, R. Skvorčinskienė, L. Paukštaitis, Peculiarities of the Leidenfrost effect application for drag force reduction, Mechanics. 20 (2014) 266–273. https://doi.org/10.5755/j01.mech.20.3.6775.

[83] K. Mohanarangam, S.C.P. Cheung, J.Y. Tu, L. Chen, Numerical simulation of micro-bubble drag reduction using population balance model, Ocean Engineering. 36 (2009) 863–872. https://doi.org/10.1016/j.oceaneng.2009.05.001.

[84] S. Sindagi, R. Vijayakumar, B.K. Saxena, Parametric CFD investigation of ALS technique on reduction in drag of bulk carrier, Ships and Offshore Structures. 15 (2020) 417–430. https://doi.org/10.1080/17445302.2019.1661617.

[85] I. Felde, Új módszer acélok edzéséhez használatos hűtőközegek hűtőképességének minősítésére, Miskolci Egyetem. Műszaki Anyagtudományi Kar. Kerpely Antal Anyagtudományok és technológiák Doktori Iskola, 2007. http://midra.uni-miskolc.hu/jadox/portal/displayImage.psml?offset=1&docID=5600&secID=1051&libraryId=-1&limit=10&pageSet=newLine&resultType=0&schemaId=null&action=browse&site=search&type=advanced&orderBy=0 (accessed July 12, 2022).

[86] C. Demirel, Experimentelle Untersuchung und Simulation des Abschreckprozesses von bauteilähnlichen Geometrien aus G-AlSi7Mg, (2009). https://depositonce.tu-berlin.de/items/a928e92c-4afe-4351-9012-e3b9ad23666b/ urn:nbn:de:kobv:83-opus-23363 (accessed October 3, 2022).

[87] E. Troell, H. Kristoffersen, J. Bodin, S. Segerberg, I. Felde, Unique software bridges the gap between cooling curves and the result of hardening∗, 62 (2007) 110–115. https://doi.org/10.3139/105.100414.

[88] D. Landek, Models and algorithms for computer-aided planning of induction hardening process, PhD Thesis, 2005.

[89] F.M. Tenzer, Heat transfer during transient spray cooling: An experimental and analytical study, Ph.D. Thesis, Technische Universität, 2020. https://doi.org/10.25534/tuprints-00011344.

[90] S. Jagga, S. Vanapalli, Cool-down time of a polypropylene vial quenched in liquid nitrogen, International Communications in Heat and Mass Transfer. 118 (2020) 104821. https://doi.org/10.1016/j.icheatmasstransfer.2020.104821.

[91] M. Afify, D. Gentile, M. Llory, Courbes d'ébullition en convection forcée. Deuxième partie : Effets paramétriques et corrélations, La Houille Blanche. 72 (1986) 463–474. https://doi.org/10.1051/lhb/1986048.

[92] Landek, Darko, Rezultati mjerenja - nastavak, (2022).

[93] N. Hannoschöck, Wärmeleitung und -transport: Grundlagen der Wärme- und Stoffübertragung, Springer Berlin Heidelberg, Berlin, Heidelberg, 2018. https://doi.org/10.1007/978-3-662-57572-7.

[94] W.F. Noh, CEL: A Time-Dependent, Two-Space-Dimensional, Coupled Eulerian-Lagrange Code, Other Information: Orig. Receipt Date: 31-DEC-65. (1963). https://doi.org/10.2172/4621975.

[95] D. Aubram, An arbitrary Lagrangian-Eulerian method for penetration into sand at finite deformation, 2014. https://depositonce.tu-berlin.de/items/urn:nbn:de:kobv:83-opus4-47557 (accessed September 27, 2022).

[96] C. Dobrzynski, Adaptation de Maillage anisotrope 3D et application à l'aéro-thermique des
bâtiments, Theses, Université Pierre et Marie Curie - Paris VI, 2005. https://tel.archives-ouvertes.fr/tel-00120327.

[97] J.-F. Remacle, F. Henrotte, T. Carrier-Baudouin, E. Béchet, E. Marchandise, C. Geuzaine, T. Mouton, A frontal Delaunay quad mesh generator using the L ∞ norm, International Journal for Numerical Methods in Engineering. 94 (2013) 494–512. https://doi.org/10.1002/nme.4458.

[98] X. Roca Navarro, Paving the path towards automatic hexahedral mesh generation, Ph.D. Thesis, Universitat Politècnica de Catalunya, 2009. http://www.tdx.cat/handle/10803/5858 (accessed September 30, 2022).

[99] H. Takamatsu, H. Yamashiro, H. Honda, Theoretical analysis of the stability of vapor film in subcooled film boiling on a horizontal wire, Heat Transfer - Japanese Research. 26 (1997) 219–235. https://doi.org/10.1002/(SICI)1520-6556(1997)26:4<219::AID-HTJ2>3.0.CO;2-Z.

[100] M. Čančarević, PRIBLIŽNO RJEŠAVANJE NELINEARNIH SUSTAVA (NEWTON - RAPHSONOVA METODA), Poučak : časopis za metodiku i nastavu matematike. 11 (2010) 64–72.

[101] Yamada, Takashi, Shigechi, Toru, Momoki, Satoru, Kanemaru, Kuniyasu, Yamaguchi, Tomohiko, 有限長の垂直円柱まわりのサブクール膜沸騰熱伝達(熱工学,内燃機関,動力など); Subcooled Film Boiling Heat Transfer Around a Vertical Finite-Length Cylinder(Thermal Engineering), 日本機械学会論文集. B 編; Transactions of the Japan Society of Mechanical Engineers. B. 73 (2007) 1715–1722.

[102] Yamada, Takashi, Shigechi, Toru, Momoki, Satoru, Kanemaru, Kuniyasu, Yamaguchi, Tomohiko, 有限垂直円柱まわりのサブクール膜沸騰熱伝達に関する研究 : 第 1 報 : 伝熱整理式の検討; Study on Subcooled Film Boiling Heat Transfer around a Vertical Finite-Length Cylinder : 1st Report : Examination of Correlation Equations for Heat Transfer, 長崎大学工学部研究報告; Reports of the Faculty of Engineering, Nagasaki University. 35 (2005) 1–10.

[103] van Dijk Gerard, A study on mathematical models for turbulent flows, Technische Universiteit Eindhoven, Eindhoven, 1987.

APPENDIX A: THE DERIVATION OF CORRELATION FOR CALCULATION OF LOCAL NUSSELT NUMBER

The expression for local, cell-size dependent, Nusselt number stems from the balance between thermal phase change and energy jump mass transfer models. It is thereby assumed that liquid is at saturation temperature, $T_l = T'$. Other, model related, assumptions are also incorporated.

Thus, in thermal phase change model it is also assumed that vapor and liquid phase's scaling factors are equal to unity, that is, $C_v = C_l = 1.0$ and that interfacial area is computed as magnitude of volume fraction field, Eq. (35). Hence, Eq. (41), reduces to:

$$\dot{m}_{lv} = \frac{-h_v |\nabla \alpha_v| \left(T' - T_v\right)}{r_0} \tag{A 1}$$

where r_0 denotes specific heat of vaporization.

As stated in the introduction, one of the goals of the proposed model is to ensure the occurrence of dominant mass transfer rate in the interface zone. Therefore, in order to define energy jump model, consider the phase change process in a three-cell stencil, as shown in Fig. 44. Let the interface is thereby located between positions *i* and *i + 1* at *x*-coordinate of right sided Cartesian coordinate system. Furthermore, it is assumed that the superheated vapor phase occupies the zone on the left side of the interface, while the remainder of the domain is filled with liquid at saturation temperature.

The temperature gradient at the right side of the central cell's center is calculated as [30]:

$$\frac{dT}{dx} = \frac{T' - T_i}{d_3} \tag{A 2}$$

where d_3 denotes the distance between the interface and the center of adjacent vapor cell, see Fig. 45.

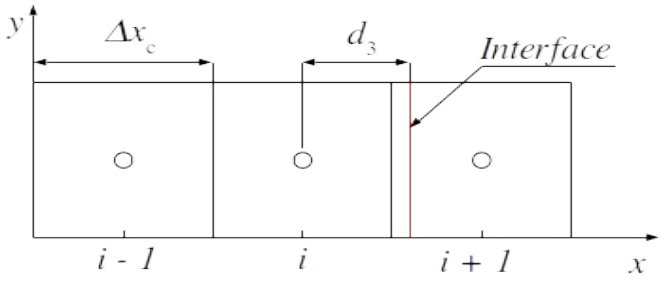


Fig. 45. The mass transfer process in a three-cell stencil.

The mass transfer rate calculated using energy jump model is defined as [30]:

$$\dot{m}_{\mathrm{lv}} = \frac{\lambda_{\mathrm{l}} \left(\nabla T_{\mathrm{l}} \right) \cdot \vec{n} - \lambda_{\mathrm{v}} \left(\nabla T_{\mathrm{v}} \right) \cdot \vec{n}}{r_0} \cdot \frac{A_{\mathrm{i}}}{V_{\mathrm{c}}} \tag{A 3}$$

where indexes l and v denote, respectively, liquid and vapor phase, ∇T is the temperature gradient, $\vec{n}$ is the interface normal directed from vapor to liquid phase, A_{i} is the interface area and V_{c} is the cell volume.

Since the liquid is at saturation temperature, $\nabla T_{\mathrm{l}} = 0$, and Eq. (A 3) is reduced to:

$$\dot{m}_{\mathrm{lv}} = \frac{-\lambda_{\mathrm{v}} \left(\nabla T_{\mathrm{v}} \right) \cdot \vec{n}}{r_0} \cdot \frac{A_{\mathrm{i}}}{V_{\mathrm{c}}} \tag{A 4}$$

The consideration of the problem as one-dimensional allows for the following simplification:

$$\left| \nabla \alpha_{\mathrm{v}} \right| \approx \frac{A_{\mathrm{i}}}{V_{\mathrm{c}}}$$

Hence, the energy jump model reads:

$$\dot{m}_{\mathrm{lv}} = \frac{-\lambda_{\mathrm{v}} \nabla T_{\mathrm{v}} \left| \nabla \alpha_{\mathrm{v}} \right|}{r_0} \tag{A 5}$$

Approximation of vapor phase's temperature gradient using Eq. (A 2) gives:

$$\dot{m}_{\mathrm{lv}} = \frac{-1}{r_0} \lambda_{\mathrm{v}} \frac{T' - T_{\mathrm{i}}}{d_3} \left| \nabla \alpha_{\mathrm{v}} \right| \tag{A 6}$$

The equalization of the right-hand sides of Eqs. (A 1) and (A 6) gives:

$$h_{\mathrm{v}} \left(T' - T_{\mathrm{v}} \right) = \lambda_{\mathrm{v}} \frac{T' - T_{\mathrm{i}}}{d_3} \tag{A 7}$$

The heat transfer is present only in vapor phase and, therefore, the heat transfer coefficient is defined as:

$$h_{\mathrm{v}} = \frac{\lambda_{\mathrm{v}} N u_{\mathrm{v}}}{d_{\mathrm{v}}} \tag{A 8}$$

Further approximations refer to *i*-th cell temperature and distance *h*, and are given by:

$$T_{\mathrm{i}} \approx T_{\mathrm{v}}$$

$$d_3 \approx \frac{\Delta x}{2}$$

The involvement of these approximations together with Eq. (A 8) in Eq. (A 7) yields the local, cell-size dependent, Nusselt number

$$N u_{\mathrm{v}} = \frac{2 \cdot d_{\mathrm{v}}}{\Delta x} \tag{A 9}$$

By rearranging Eq. (A 9) we obtain:

$$N u_{\mathrm{v}} = \frac{d_{\mathrm{p}}}{\frac{\Delta x}{2}}$$

which involved in Eq. (A 8) gives:

$$h_{\mathrm{v}} = \frac{\lambda_{\mathrm{v}}}{\frac{\Delta x}{2}}$$

where the diameter of dispersed phase vanished. By involving it in the mass transfer equation, Eq. (A 1), and after subsequent rearranging we have:

$$\dot{m}_{\mathrm{lv}} r_0 = -\lambda_{\mathrm{v}} \frac{T_{\mathrm{v}} - T'}{\frac{\Delta x}{2}} |\nabla \alpha_{\mathrm{v}}| \qquad \text{(A 10)}$$

Thus, the heat transfer coefficient is a fictitious quantity since it is used to express the approximate distance from the cell center of the control volume that contains the interface to the interface itself and to involve the thermal conductivity of the vapor phase in the mass transfer model. Furthermore, its inclusion in the mass transfer model yields an approximation of the temperature gradient at the interface, that appears from energy balance at the interface, i.e., in the heat flux in the normal direction to the interface.

APPENDIX B. THE ESTIMATION OF VAPOR LAYER THICKNESS IN A STABLE FILM BOILING WITH A SMOOTH VAPOR-LIQUID INTERFACE

In what follows a boundary layer theory analysis, according to Yamada *et al.* [62] has been performed in order to study the vapor film thickness. The average vapor film thickness reads:

$$\bar{\delta}_{\mathrm{m}} = \frac{\bar{\tilde{\delta}}_{\mathrm{m}} L}{\left(Gr_{\mathrm{B}}/Sp\right)^{\frac{1}{4}}}, \tag{B 1}$$

where, on the other hand, $\bar{\tilde{\delta}}_{\mathrm{m}}$ is the average dimensionless film thickness, L is the specimen length (height in the case of vertical, upward oriented, cylinder, m), Gr_{B} is the Grashoff number for this natural convection case and Sp is the degree of wall superheat. The average dimensionless vapor layer thickness, $\bar{\tilde{\delta}}_{\mathrm{m}}$, is calculated as:

$$\bar{\tilde{\delta}}_{\mathrm{m}} = \frac{1}{L}\int_0^L \tilde{\delta}_{\mathrm{B}}\,\mathrm{d}\,x_{\mathrm{B}}, \tag{B 2}$$

where $\tilde{\delta}_{\mathrm{B}}$ is the dimensionless vapor layer thickness profile, given by the expression derived in Yamada *et al.* [62].

After integration the profile equation reads:

$$\tilde{\delta}_{\mathrm{B}} = \frac{8}{5}\left\{\left[1+\left(\frac{\tilde{\delta}_{\mathrm{B},0}}{2}\right)^4\right]^{\frac{5}{4}} - \left(\frac{\tilde{\delta}_{\mathrm{B},0}}{2}\right)^5\right\} L, \tag{B 3}$$

where $\tilde{\delta}_{\mathrm{B},0}$ is the dimensionless initial layer thickness due to the inflow from the vapor layer beneath the bottom surface of the cylinder and is dependent on the flow conditions, i. e., the momentum equation boundary conditions at the vapor-liquid interface at the horizontal bottom and vertical surface of the cylinder specimen. Hence, for the non-slip (see Fig. 46) conditions at

both the interfaces, Yamada *et al.* [62] arrive at the following expression for computation of the initial film layer:

$$\widetilde{\delta}_{\mathrm{B},0} = 1.45781 \left(D/L \right)^{\frac{1}{5}} \left(Sp/Gr_{\mathrm{B}} \right)^{\frac{1}{60}}, \tag{B 4}$$

with the quantities as explained earlier in the text.

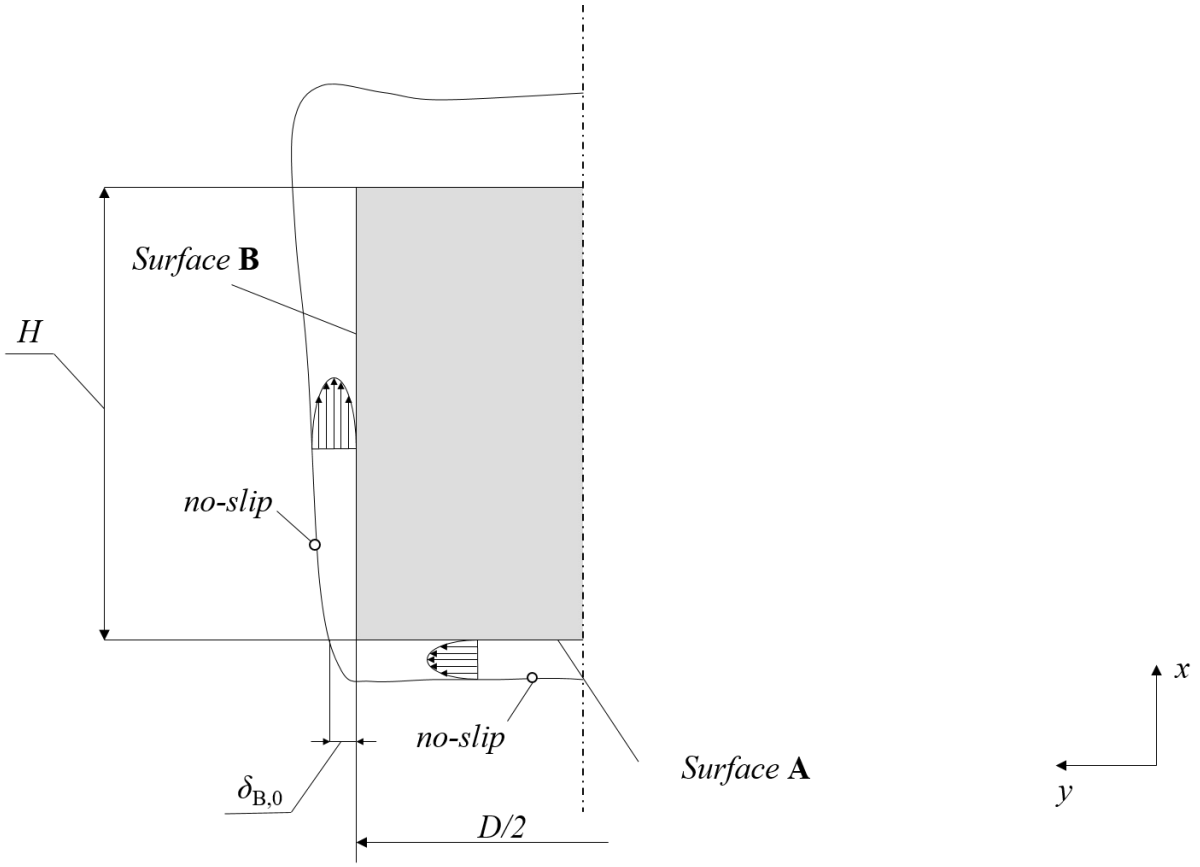


Fig. 46 A conceptual sketch of the boundary conditions applied in the theoretical according to Yamada et al. [62]*, and used in obtaining the average velocity for determination of TKE here.*

The original model also accounts four different combinations of slip and non-slip conditions at the vapor-liquid interface during film boiling around a vertical cylinder, thus being suitable for even flow boiling applications.

BIOGRAPHY AND A LIST OF SELECTED PUBLICATIONS

Biography

Alen Cukrov was born on May 16th, 1989, in Šibenik. After finishing elementary school in Vodice, he enters the high school of economics, namely Ekonomska škola Šibenik, in Šibenik, in 2004, and finishes it in 2008, being exempted from taking the matura exam due to excellent grades at the end of each high school year. In the same year, he enrolls in the undergraduate program at the University of Zagreb's Faculty of Mechanical Engineering and Naval Architecture (FAMENA), which he completes in February 2012 with the highest honor, *Summa Cum Laude*. He has immediately started master's studies at the same institution. In the academic year 2013/2014, he visited TU Darmstadt's Center of Smart Interfaces via the Erasmus mobility for placements program and stayed there for five months. He completed his master's course in 2015. After completing his studies, he joined Creative Fields d.o.o., where he worked one year as an intern. In December 2016, he started to work as an assistant at the FAMENA. In October 2017, he spent one month doing research at the Paul Scherrer Institute in Switzerland as a Guest Scientist, and in the academic year 2019/2020, he visited the Paul Scherrer Institute again, but this time as a FCS scholarship holder at the ETH Zürich.

Selected publications

1. Vlček, D., Sato, Y., Niceno, B. & Cukrov, A. (2022) Boiling flow simulations for DEBORA experiment using Eulerian CFD approach. U: (editor) (ur.)Proceedings of the 7th thermal and fluids engineering conference (TFEC).
2. Cukrov, A., Sato, Y., Boras, I. & Ničeno, B. (2021) A solution to Stefan problem using Eulerian two-fluid VOF model. *Brodogradnja*, 72 (4), 141-164 doi:10.21278/brod72408.
3. Cukrov, A., Sato, Y., Boras, I. & Ničeno, B. (2018) Numerical Simulation of Annular Flow Boiling in a Vertical Pipe Using Two-Fluid Model. U: Marović, P., Krstulović-Opara, L. & Galić, M. (ur.)Proceedings of the 9th International Congress of Croatian Society of Mechanics.

ŽIVOTOPIS I POPIS ODABRANIH PUBLIKACIJA

Životopis

Alen Cukrov rođen je 16. svibnja 1989. godine u Šibeniku. Nakon završene osnovne škole u Vodicama, upisuje srednju ekonomsku školu u Šibeniku, koju završava 2008. godine; bez polaganja mature uslijed odličnog uspjeha na kraju svake školske godine. Iste godine, u srpnju, upisuje preddiplomski studij na Fakultetu strojarstva i brodogradnje Sveučilišta u Zagrebu (FSB), koji završava u veljači 2012. godine s najvišom pohvalom, *Summa Cum Laude*. Odmah započinje diplomski studij na istom fakultetu. Akademske godine 2013./2014. posjećuje institut Center of Smart Interfaces pri Tehničkom sveučilištu u Darmstadtu u okviru programa Erasmus stručne prakse, te boravi tamo pet mjeseci. Diplomski studij završava 2015. godine. Nakon završetka studija pridružuje se tvrtki Creative Fields d.o.o., gdje radi jednu godinu kao pripravnik na stručnom osposobljavanju. U prosincu 2016. godine, započinje s radom na FSB-u kao asistent. U isto vrijeme pohađa doktorski studij na istom fakultetu. U listopadu 2017. godine provodi mjesec dana radeći istraživanje na Paul Scherrer Institutu u Švicarskoj kao gostujući znanstvenik, a tokom akademske godine 2019./2020. ponovno posjećuje Paul Scherrer Institut, ali ovaj puta kao stipendist Vlade Švicarske Konfederacije na sveučilištu ETH Zürich.

Odabrane publikacije

1. Vlček, Daniel; Sato, Yohei; Niceno, Bojan; Cukrov, Alen Boiling flow simulations for DEBORA experiment using Eulerian CFD approach. // Proceedings of the 7th thermal and fluids engineering conference (TFEC) / (editor) (ur.). Las Vegas, NV, USA: Begellhouse, 2022. str. 1539-1548.
2. Cukrov, Alen; Sato, Yohei; Boras, Ivanka; Ničeno, Bojan A solution to Stefan problem using Eulerian two-fluid VOF model. // Brodogradnja, 72 (2021), 4; 141-164 doi:10.21278/brod72408 (međunarodna recenzija, članak, znanstveni)
3. Cukrov, Alen; Sato, Yohei; Boras, Ivanka; Ničeno, Bojan Numerical Simulation of Annular Flow Boiling in a Vertical Pipe Using Two-Fluid Model. // Proceedings of the 9th International Congress of CSM / Marović, Pavao ; Krstulović-Opara, Lovre ; Galić, Mirela (ur.). Split: Hrvatsko društvo za mehaniku, 2018. str. 1-9.